UNIVERSIDADE ESTADUAL DE CAMPINAS

INSTITUTO DE QUÍMICA

TATHIANA MIDORI KOKUMAI

PLATINUM CATALYSTS FOR HYDROGEN PRODUCTION REACTIONS

CATALISADORES DE PLATINA PARA REAÇÕES DE PRODUÇÃO DE HIDROGÊNIO

CAMPINAS
2018

TATHIANA MIDORI KOKUMAI

PLATINUM CATALYSTS FOR HYDROGEN PRODUCTION REACTIONS

CATALISADORES DE PLATINA PARA REAÇÕES DE PRODUÇÃO DE HIDROGÊNIO

Tese de Doutorado apresentada ao Instituto de Química da Universidade Estadual de Campinas como parte dos requisitos exigidos para a obtenção do título de Doutora em Ciências

Doctor´s Thesis presented to the Institute of Chemistry of the University of Campinas as part of the requirements to obtain the title of Doctor in Sciences.

Supervisor: Profa. Dra. Daniela Zanchet

ESTE EXEMPLAR CORRESPONDE À VERSÃO FINAL DA TESE DEFENDIDA PELA ALUNA TATHIANA MIDORI KOKUMAI, E ORIENTADA PELA PROFA. DRA. DANIELA ZANCHET

CAMPINAS
2018

Agência(s) de fomento e nº(s) de processo(s): CAPES
ORCID: https://orcid.org/0000-0002-3478-2771

Ficha catalográfica
Universidade Estadual de Campinas
Biblioteca do Instituto de Química
Camila Barleta Fullin - CRB 8462

K829p

Kokumai, Tathiana Midori, 1983-
Platinum catalysts for hydrogen production reactions / Tathiana Midori Kokumai. – Campinas, SP : [s.n.], 2018.

Orientador: Daniela Zanchet.
Tese (doutorado) – Universidade Estadual de Campinas, Instituto de Química.

1. Catálise heterogênea. 2. Platina. 3. Óxidos metálicos. 4. Nanomateriais. 5. Hidrogênio - Produção. I. Zanchet, Daniela, 1972-. II. Universidade Estadual de Campinas. Instituto de Química. III. Título.

Informações para Biblioteca Digital

Título em outro idioma: Catalisadores de platina para reações de produção de hidrogênio
Palavras-chave em inglês:
Heterogeneous catalysis
Platinum
Metallic oxides
Nanomaterials
Hydrogen - Production
Área de concentração: Química Inorgânica
Titulação: Doutora em Ciências
Banca examinadora:
Daniela Zanchet [Orientador]
Dalmo Mandelli
Leandro Martins
Heloise de Oliveira Pastore
Miguel Angel San Miguel Barrera
Data de defesa: 27-04-2018
Programa de Pós-Graduação: Química

BANCA EXAMINADORA

Profa. Dra. Daniela Zanchet (Orientadora)

Prof. Dr. Dalmo Mandelli (CCNH-UFABC/ Santo André)

Prof. Dr. Leandro Martins (IQ-UNESP/Araraquara)

Profa. Dra. Heloise de Oliveira Pastore (IQ-UNICAMP)

Prof. Dr. Miguel Angel San Miguel Barrera (IQ-UNICAMP)

A Ata da defesa com as respectivas assinaturas dos membros encontra-se no processo de vida acadêmica do(a) aluno(a).

Este exemplar corresponde à redação final da Tese de Doutorado defendida pelo(a) aluno(a) **TATHIANA MIDORI KOKUMAI,** aprovada pela Comissão Julgadora em 27 de abril de 2018.

“People think dreams aren't real just because they aren't made of matter, of particles. Dreams are real. But they are made of viewpoints, of images, of memories and puns and lost hopes.” John Dee on *Sandman* (Neil Gaiman)

Agradecimentos

A realização deste trabalho não teria sido possível sem o apoio de diversas pessoas. Começando pela grande família, meus pais Hélio, Kyoko e Dalton, minhas irmãs Thaís, Nathalie, Bianca e Kiara, em especial das crianças Aya, Naomi, Yuna e Kazuya, Sayuri e Hikari, sem vocês nada teria acontecido.

Como uma das maiores motivações deste trabalho, agradeço à Prof. Daniela Zanchet, pela oportunidade e apoio durante estes anos e que continuamente me mostra que podemos ir além.

Aos queridos amigos do Grupo de Catálise e Nanomateriais Diego Carvalho, Priscila Destro, Danielle Gonçalves, Isaias Aragão, Felipe Moreira, Luelc Costa, Tanna Fiuza, Karen Resende, Daniel Cantane, Arthur Malheiro e Monique Ottmann, que tornaram o caminho ao longo destes muitos anos menos tortuoso. Obrigada pelas discussões, comidas, bares, cinemas, caminhadas e medidas de madrugada. Principalmente, agradeço à Debora, Felipe, Priscila e Diego pela construção das linhas catalíticas. Agradeço especialmente ao Diego pelo companheirismo, pelas viagens, pelo aprendizado cultural e por me fazer uma pessoa mais paciente. E à Danielle, pela companhia nos últimos períodos de trabalho.

Aos meus amigos de mais longa data Rosana, Maria, Alana, Sheila, Edson, e Jacqueline, por sempre estarem ao meu lado mesmo na distância. Em especial, agradeço à Rosana pelo companheirismo, desabafos, reflexões existenciais, incentivo e apoio ao longo deste trabalho.

Agradeço ao Massimo Colombo e Liberato Manna pelo apoio, supervisão e aprendizagem, e aos funcionários do Instituto Italiano de Tecnologia. Aos amigos que fiz na Itália, agradeço especialmente à Cansunur Demirci, Mengjiao Wang, Sergey Poghosian e Laura Cannarozzi, que fizeram deste período uma das melhores fases da minha vida.

Meus agradecimentos aos funcionários do IQ e da UNICAMP e ao Prof. José Maria Bueno pela disponibilização da infraestrutura do LabCat da UFSCar. Agradeço também ao Laboratório Nacional de Nanomateriais (LNNano) e ao Laboratório Nacional de Luz Síncrotron (LNLS).

Meus agradecimentos às agências de fomento CAPES, CNPq (406879/2013-3), FAPESP (2011/50727-9, 2015/50375-6) e a FAEPEX/UNICAMP pelo auxílio concedido.

Resumo

O objetivo do presente trabalho foi o estudo de catalisadores nanoestruturados aplicados à reação de reforma a vapor do glicerol (*glycerol steam reforming*, GSR). A reação de deslocamento gás-água (*water-gas shift*, WGS) também foi investigada por ser etapa fundamental no aumento da produção de hidrogênio por esta rota. Os sistemas são catalisadores suportados à base de platina e foram divididos em dois grupos, um contendo óxido de vanádio e o outro, óxido de cério. Os resultados do primeiro grupo evidenciaram o efeito benéfico da adição de vanádio na reação de WGS através da maior conversão de CO. Por outro lado, verificou-se que o aumento do teor de vanádio não impacta na atividade catalítica devido à formação de espécies poliméricas VO_x na superfície do suporte que não estão em contato com a Pt. Ainda, a presença do vanádio não favoreceu o aumento da fração de hidrogênio na reação de GSR, pois promoveu a formação de subprodutos, o que resultou no consumo do H_2 produzido.

O segundo grupo contém catalisadores à base de Pt/CeO_2 suportados em sílica produzidos a partir de nanopartículas (NPs) de CeO_2 de diferentes tamanhos médios (5 e 9 nm) ou impregnação do precursor de Ce, visando avaliar tanto o efeito da presença da céria quanto o de tamanho/dispersão na atividade catalítica. Os resultados indicaram o aumento expressivo do desempenho nas reações de WGS e GSR na presença da céria, no entanto a comparação entre os catalisadores com os diferentes tamanhos de CeO_2 não mostrou alterações de mesma magnitude. A céria se mostrou essencial na reação de GSR por facilitar o desbloqueio dos sítios mais ativos da Pt, liberando-os para interagir com o glicerol através da remoção do CO fortemente ligado como CO_2. Utilizando a metodologia de excitação modulada acoplada à espectroscopia no infravermelho por reflectância difusa com transformada de Fourier (modulation-excitation diffuse reflectance infrared Fourier transformed spectroscopy, ME-DRIFTS) em condições reacionais, foi possível identificar a formação de espécies carboxilatos e formiatos como as espécies ativas formadas na superfície dos catalisadores de céria durante a reação de WGS, o que pode contribuir para o melhor entendimento do comportamento destes sistemas nas duas reações de interesse.

Desta forma, a sistemática investigação destes sistemas nanoestruturados resultou na identificação de propriedades que determinam seus desempenhos, que devem ser levadas em consideração no desenvolvimento racional de catalisadores mais ativos, estáveis e seletivos.

Abstract

The present work had as the main goal the study of nanostructured catalysts applied to glycerol steam reforming (GSR) reaction. The water-gas shift (WGS) reaction was also investigated since it is a fundamental step to increase hydrogen production by this approach. The systems are Pt-based supported catalysts and they were divided in two groups, one containing vanadium oxide and the other, cerium dioxide. The results from the first group evidenced a beneficial effect of vanadium addition in WGS reaction, by increasing the CO conversion rates. On the other hand, it was noted that the increment in vanadium loading is not relevant due to the formation of polymeric VO_x species on the support surface which are not in close contact with Pt. Moreover, the presence of vanadium did not enhance hydrogen production during GSR reaction since it promoted the formation of lateral products which resulted in the consumption of the produced H_2.

The second group has silica supported Pt/CeO_2 based catalysts which were produced from CeO_2 nanoparticles (NPs) with different mean sizes (5 and 9 nm) or by impregnation of Ce precursor, aiming to evaluate both the effect of ceria presence and its size/dispersion on catalytic activity. The results indicated an expressive increase in WGS and GSR performances due to the presence of ceria, however the comparison between the samples with different CeO_2 sizes did not show variations with the same magnitude. Ceria demonstrated to be essential on GSR reaction by facilitating the cleaning of the most active Pt sites, releasing them to interact with glycerol through the removal of the strongly bound CO as CO_2. By means of the modulation-excitation methodology coupled to diffuse reflectance infrared Fourier transformed spectroscopy (ME-DRIFTS) under reaction conditions, it was possible to identify the formation of carboxylate and formate species as the active intermediate species formed on ceria catalysts surface during WGS reaction, which may contribute to a deeper understanding of the behavior of these systems on both target reactions.

Therefore, the systematic investigation of these nanostructured systems led to the recognition of key properties dictating their performance, which should be taken into account for the rational design of more active, stable and selective catalysts.

List of Schemes

List of Figures

List of Tables

List of Abbreviations

CeO_2 NPs – colloidal ceria nanoparticles
DFT - density functional theory
DRIFTS - diffuse reflectance infrared Fourier transform spectroscopy
EXAFS - extended X-ray absorption fine structure
FID – Flame ionization detector
GC – gas chromatograph(y)
Gly_rate_max –maximum value of glycerol conversion rate to gas products
Gly_rate_32 - value of glycerol conversion rate to gas products at 32 min under reaction
GSR – glycerol steam reforming
HC – highly under-coordinated
HRTEM - high resolution transmission electron microscopy
ICP-OES - Inductively coupled plasma - Optic emission spectroscopy
IIT – Italian Institute of Technology
LNLS - Brazilian Synchrotron Light Laboratory
MS – mass spectrometer
MCT - mercury cadmium telluride
MES – modulation excitation spectroscopy
PEMFC - proton-exchange membrane fuel cell
PROX-CO - preferential CO oxidation
PSD – phase sensitive detection
Pt NPs - colloidal platinum nanoparticles
RT – room temperature
STEM - scanning transmission electron microscopy
SSITKA – steady-state isotopic transient kinetic analysis
TCD - thermal conductive detector
TEM - transmission electron microscopy
TGA - thermo gravimetric analyses
TOF - turn over frequency
UC – under-coordinated
UV-Vis - electronic spectroscopy on the ultraviolet and visible range
WC – well-coordinated
WGS – water-gas shift
WHSV - weight hourly space velocity
XAS – X-ray absorption spectroscopy
XAFS – X-ray absorption fine structure spectroscopy

XANES - X-ray absorption near edge structure

XRD - X-ray diffraction

XRF – X-ray fluorescence spectroscopy

SUMMARY

Chapter 1

1.1 CONTEXTUALIZATION

With the increasing energy consumption worldwide, the development and improvement of clean energy technologies are crucial to shift the economy away from relying on fossil fuels and to assure that power demand is fulfilled globally without elevating costs and waste production[1]. Although some renewable sources are already available (photovoltaics, wind, hydropower), their share in the global energy production is yet small (less than 20% in 2015) and the power produced from fossil fuels is undeniable cheaper. As the technology advances to improve renewable sources capacity and price, it also enables the discovery of new deposits and methods to extract fuels once not economically viable (shale and bituminous sands)[2]. To drive the transition from a fossil fuel based economy to a feasible far-reaching renewable energy distribution, dramatic breakthroughs such as adopting strict policies for fossil fuels utilization and ambitious investments in research and development of renewable sources technologies are essential.

The use of waste organic compounds as source to generate fuels and power is an interesting strategy to avoid the dependence on fossil fuels, besides reducing waste accumulation and storage (landfilling) issues. Biomass is considered a powerful feedstock for energy and value-added chemicals, since it is basically organic matter which can be derived from wood, agricultural crops, animal manure and human sewage, among other sources. One may even argue that biomass processing, when efficient, can be considered CO_2 neutral since plants can reutilize this gas through photosynthesis [3]. Biomass transformations have been in the spotlight and there are several reported strategies to its conversion to transportation fuels, power/heat and chemicals[1]. However, there are drawbacks in its utilization since raw biomass is usually heterogeneous, has high moisture content and low calorific value, the latter can be enhanced by removing its oxygen as CO, CO_2 and H_2O. An important transportation fuel that can be derived from biomass transesterification is biodiesel, which has been replacing oil-derived diesel successfully in automotive engines [4]; however, this process generates byproducts, with glycerol (1,2,3-propanetriol, $C_3H_8O_3$) corresponding to about 10 %wt. of the production [5]. Glycerol is also produced in other biofuels synthesis routes, such as the ethanol from fermentation processes [6].

Although glycerol is a raw material for the synthesis of several commodities and high-value chemicals [7], its high availability caused by the increased biodiesel production has overcome its industrial demand and its low price is now a drawback in biodiesel economy. Added to its inability to be used as fuel in oil and diesel engines, glycerol abundance has motivated its transformation into syngas ($CO + H_2$) to be used in high-value chemicals and

fuel synthesis, as well as a source of hydrogen to produce electricity through fuel cell technologies [7–11]. Hydrogen is mainly produced from fossil fuels processing, with methane as the main (and less expensive) source, thus producing greenhouse gases. Besides its necessity in the petroleum refining, production of ammonia, methanol and other chemicals, hydrogen is a promising high energy carrier and can be also used in transportation, although the technologies for such applications still needs to be improved [12–14]. Such potential created the urge to develop competitive and cleaner ways to produce hydrogen, from abundant renewable and sustainable sources, as biomass derived compounds.

The majority of processes concerning the conversion of biomass to hydrogen involves catalytic transformations and they occur by several routes and intermediate compounds. The catalytic conversion of glycerol to hydrogen-rich streams can be carried out through pyrolysis or reforming reactions, such as steam, aqueous phase and photo-reforming reactions [6,15]. Among them, glycerol steam reforming (GSR) reaction ((Equation 1.1) is advantageous because it can boost hydrogen production from the decomposition reaction (Equation 1.2) without requiring high pressures.

$$\mathbf{C_3H_8O_3 + 3H_2O \rightleftharpoons 7H_2 + 3CO_2 \quad \Delta H = 128\ kJ\ mol^{-1}} \qquad \text{(Equation 1.1)}$$

The global catalytic reaction involves at least two sequential reactions, first glycerol is converted to H_2 and CO (Equation 1.2), followed by the water-gas shift reaction (WGS), in which the produced CO reacts with steam to form CO_2 and additional H_2 (Equation 1.3). As a consequence, hydrogen production can be enhanced by favoring the WGS reaction step [6].

$$\mathbf{C_3H_8O_3 \rightarrow 3CO + 4H_2 \quad \Delta H = 251\ kJ\ mol^{-1}} \qquad \text{(Equation 1.2)}$$

$$\mathbf{CO + H_2O \rightleftharpoons CO_2 + H_2 \quad \Delta H = -41\ kJ\ mol^{-1}} \qquad \text{(Equation 1.3)}$$

For application in fuel cells, such as the PEMFC (Proton Exchange Membrane Fuel Cell), it is in fact necessary to decrease the residual CO concentration from the H_2 stream to few ppms, to avoid deactivation of Pt-based catalysts present in the cell [14]. Therefore, the reformate gas stream is typical flown through a WGS reactor, decreasing the CO levels down to about 0.5-1.0 % of CO. The CO concentration can be further decreased to 50 ppm (or lower) by the preferential CO oxidation reaction (PROX-CO), (Equation 1.4), in which the parallel H_2 oxidation ((Equation 1.5) has to be minimized.

$$\mathbf{CO + \frac{1}{2}O_2 \rightleftharpoons CO_2 \quad \Delta H = -283\ kJ\ mol^{-1}} \qquad \text{(Equation 1.4)}$$

$$\boldsymbol{H_2 + \frac{1}{2}O_2 \rightleftharpoons H_2O \quad \Delta H = -243\ kJ\ mol^{-1}}$$ (Equation 1.5)

The success of the glycerol transformation to hydrogen through this route depends, as a consequence, on each step of the process.

The concentration of glycerol on the crude byproduct from biodiesel production varies around 60-80 %wt. and its purification for further synthetic purposes is expensive [10,16]. Its use for hydrogen production through catalytic reforming reaction is attractive, since it has been reported to occur within a range of glycerol concentrations[17], and some other organic compounds in the mixture could also be reformed, depending on reaction conditions [18,19]. However, it must be taken into consideration the nature of the catalysts and its interaction with such impurities to avoid its deactivation [7,20,21], which may decrease its commercial appeal. Nevertheless, the successful application of byproduct glycerol for energy purposes by hydrogen generation drastically relies on the understanding of the catalytic reforming processes, the role of catalytic systems and the key parameters to improve H_2 selectivity.

GSR reaction has been reported in several experimental conditions, mostly using Ni and Pt catalysts supported in oxides such as Al_2O_3, SiO_2, ZrO_2, TiO_2, CeO_2[22–27]. For the low temperature WGS and PROX-CO reactions, the most promising catalysts are composed by Pt, Au, Pd, Ru, Rh and Cu [28–33] supported on reducible oxides such as CeO_2, TiO_2 and ZrO_2/CeO_2 [34–36]. For WGS, PROX-CO and GSR reactions, both metal phase and support have a determinant role on the reaction mechanism, as well as the interface between them [33,37–39].

As the supported metallic phase, the efficiency of Pt is well known for both WGS and GSR reactions, and for the latter it showed less methane as by-product when compared to Ni over the same supports[6].

Regarding the metal oxide acting as support (or as promoter, when it is over another oxide as support) in catalysts for WGS and GSR reactions, reducible oxides are usually chosen by their properties that can enhance activity, such as oxygen mobility, strong interaction with metal phase, promotion of spillover of species between them and thermal stability of the catalysts [36].

Thus, a successful GSR reaction catalyst to promote the maximization of CO-free H_2 production must favor both glycerol decomposition and WGS reactions and avoid the formation of byproducts and deactivation. The catalyst composition and structure must be thoughtfully arranged to achieve the desired properties, therefore Pt supported in reducible oxides is a promising candidate since it could favor WGS step within GSR reaction, increasing H_2 formation and reducing CO concentration in the outlet stream.

1.2 GOALS AND THESIS PRESENTATION

The purpose of this project was the development of well-defined nanostructured catalysts to allow the investigation of specific properties dictating catalytic performance towards reactions for hydrogen production. A thoughtful catalyst design is required in order to favor beneficial characteristics while suppressing detrimental ones. Factors as the synthesis method (addition of the metallic phase), nature of support, size control of metallic phase and/or metal oxide particles and the creation of interfacial sites for bifunctional catalysts have a key role in enhancing the desired catalytic activity and stability. Exploring these well-defined systems may assist in the investigation of the importance of a given isolated parameter, providing insights for a better comprehension of such systems.

The bifunctional systems investigated herein were composed of Pt as the metallic phase, supported on a high surface area support (Al_2O_3 or SiO_2) promoted with a reducible metal oxide (VO_x or CeO_2). These set of catalysts were characterized and explored for WGS and GSR reactions, aiming to identify structure-reactivity relations, such as NP size, coordination environment of the metal, the loading and nature of the promoter and the synthesis methods. Moreover, it was intended to gather insights about the nature of the active sites and the main reaction pathways involved in the catalytic reaction.

The identification of such structure-activity relations are crucial to shed light on the rational design of more stable, selective and active catalytic systems.

Overview

In Chapter 1 the contextualization of hydrogen production from biomass for energy purposes assisted by bifunctional heterogeneous catalysts was presented as the motivation behind the study of Pt catalysts applied to WGS and GSR reactions.

In Chapter 2, a more detailed discussion about the WGS and GSR reactions is provided, as well as a better description on the importance of the specific features investigated along the work, such as the coordination environment of the atoms within a nanoparticle and the promoting role of CeO_2.

Chapter 3 comprises an adapted version (more detailed) of the findings regarding VO_x-Pt/Al_2O_3 catalysts, which were already published, as described therein.

In Chapter 4 is discussed the work related to the Pt/CeO_2/SiO_2 system, including the preparation and characterization of the samples, as well as their catalytic evaluation. It also contains the presentation and discussion of the *in situ* investigations during WGS reaction performed by modulation-excitation spectroscopy.

Finally, Chapter 5 presents a global conclusion of the work developed during the thesis, as well as perspectives to future works. The APPENDIX section contains a brief

description of published co-authored additional works which involved X-ray absorption spectroscopy. The technique was applied to the investigation of distinct catalytic systems, including *in situ* studies. The APPENDIX also holds the publication licenses for the works used herein.

Chapter 2

2.1 WGS REACTION

WGS reaction became popular in the Haber process for ammonia synthesis, where most of the H_2 was obtained by reforming of coal and coke. WGS reaction was then useful to promote the conversion of CO to CO_2, which was removed more easily from the outlet stream than CO, and also generated additional H_2. It is yet an important industrial step for reducing CO concentration on the hydrogen-rich outlet stream from catalytic reforming reactions, whether to use the H_2 for chemical synthesis or as source for fuel cells. Especially for the latter application, where there is the need for adapting H_2 production for portable devices, effort has been put to improve catalysts performance, durability, convenience and safety at low reaction temperatures [40].

WGS reaction (Equation 1.3) is moderately exothermic and conversions are limited by equilibrium. Conversion levels have also demonstrated a dependence on water concentration, with higher H_2O:CO (or H_2O:CO+CO_2) molar ratios increasing the temperature range in which the catalyst can be effective [40] and also elevating conversion levels at a given temperature [41]. In the industrial application of hydrogen production by steam reforming reaction (of methane, for example), the reformate gas (coming out of the reforming reactor) is not only composed of CO and H_2 (rich), but also have CO_2, and the presence of WGS reaction products lower the equilibrium CO conversions [40,42].

For the low temperature regime, in the context of portable applications, several systems have been investigated and key properties have been identified as determinant to render highly active and stable catalysts. Among supported catalysts, it has been discussed the importance of the nature of the metal phase, loading and dispersion over the catalyst surface. For the support, metal oxides once have been thought as mere substrates which would indirectly enhance catalyst performance by providing thermal stability to the metallic phase and favoring its high dispersion. Recently, it has been clearly evidenced that some supports have an active role in the WGS reaction mechanism, mostly demonstrated by the high activity of catalysts containing reducible oxides [35,40].

For a deeper understanding of the key parameters determining catalyst activity, it is important to discuss the actual panorama concerning WGS reaction mechanism. It is

greatly discussed in literature that the pathways to convert CO and H_2O to CO_2 and H_2 depend strongly on reaction conditions (temperature, concentration of feed components), as well as catalyst composition [43,44]. From an experimental point of view, it is generally described in literature that over bifunctional catalysts composed of a noble metal (Pt) supported in a non-reducible oxide (such as SiO_2, Al_2O_3), WGS reaction would proceed by the "associative" mechanism, in which CO would adsorb on Pt while H_2O would be activated on the support, preferably close to the metal, forming H and OH species. These species would react with adsorbed CO and then produce intermediates such as carboxylates (COO^-), formates ($HCOO^-$) and carbonates (CO_3^{2-}), which would decompose to form CO_2 and H_2. The correct assignment of the sites in which the formation of these intermediates would occur and how it would happen (migration of OH species to the metal or of CO to the support, or yet to the interface) remains a challenge [43–46]. Regarding the systems composed of a metal (Pt) supported over reducible oxides such as CeO_2, TiO_2, Co_3O_4, the "redox" mechanism is generally accepted. This route would involve the participation of oxygen from the support lattice [47–49] to oxidize the adsorbed CO, which would lead to the formation of an oxygen vacancy (reduction of the support). The vacancy in turn would be refilled with the adsorption and dissociation of a water molecule preferentially on these sites, therefore forming H_2 and regenerating the support [45]. Both reaction pathways over metal-reducible oxides catalysts are depicted in Scheme 2.1. It is important to note that both mechanisms may occur over these type of catalysts and the extent of their participation is also a matter of investigation [43,44,49], as well as the identification of the true active site (its oxidation state or even its site location, whether it is an specific lone metal site, a metal in interaction with support, or a metal within a perimeter around it) [29,49–55].

Scheme 2.1: WGS reaction mechanism over metal-reducible oxide catalysts (adapted from [56]). In the classic associative type illustrated, the carbon intermediate is depicted as a carboxyl entity.

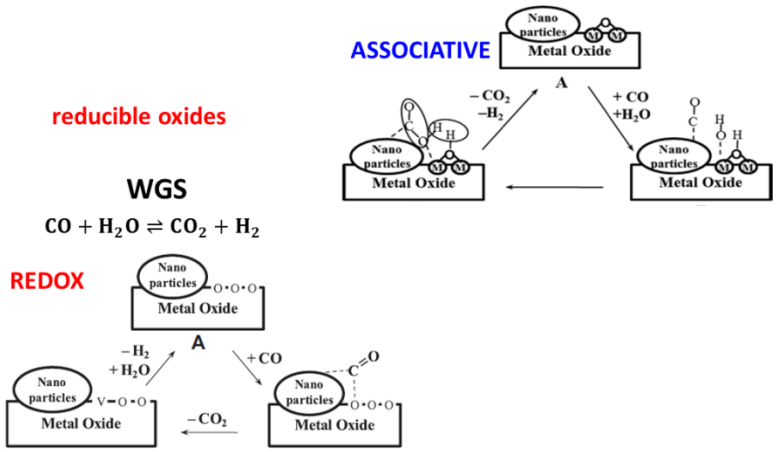

Recently, over metal-reducible oxides catalysts, it has been reported that the associative mechanism could occur by a redox generation step, in which the –OH groups consumed to form the intermediates (formate, carboxylate) would generate an oxygen vacancy to be restored by water dissociation. What distinguish this “associative mechanism with redox regeneration, or with OH group regeneration” from the true “redox” mechanism, is that the associative type occurs through intermediates such as formates and carboxylates, whereas the “redox” one does not. Concerning the “associative mechanism with redox regeneration” Kalamaras *et al.* [49] proposed the “associative formate with OH group regeneration” mechanism to occur on Pt/CeO_2 catalysts at 300 °C, thus by the formate intermediate. On the other hand, theoretical studies have also improved the understanding of WGS reaction mechanisms, such as the one performed by Aranifard *et al.* [50]. The authors studied the “associative carboxyl pathway with redox generation” by means of DFT and microkinetic modeling (227 °C), assigning carboxyl as the active intermediate. These two proposed mechanisms are illustrated in Scheme 2.2.

Scheme 2.2: Proposed “associative mechanism with redox regeneration” through a) carboxylate and b) formate intermediate species over Pt/CeO_2 catalysts for WGS reaction. Both are depicted with co-adsorbed CO on Pt (Adapted from [49,50,57]).

a)

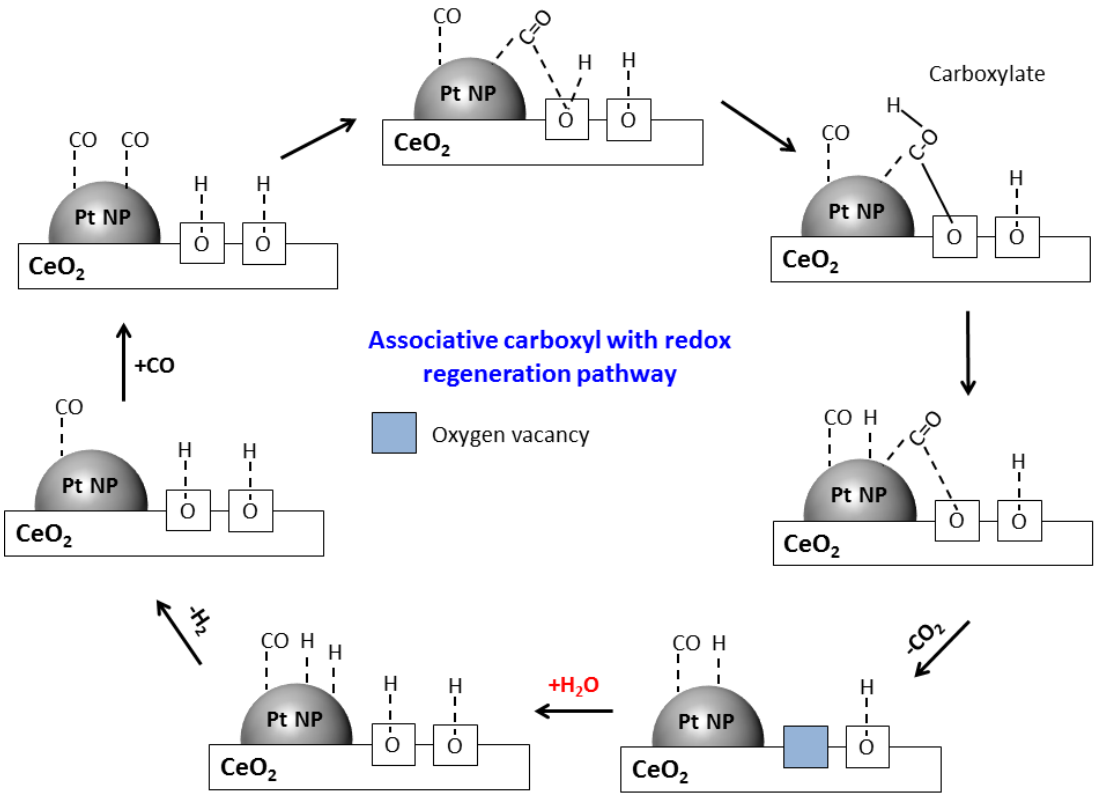

b)

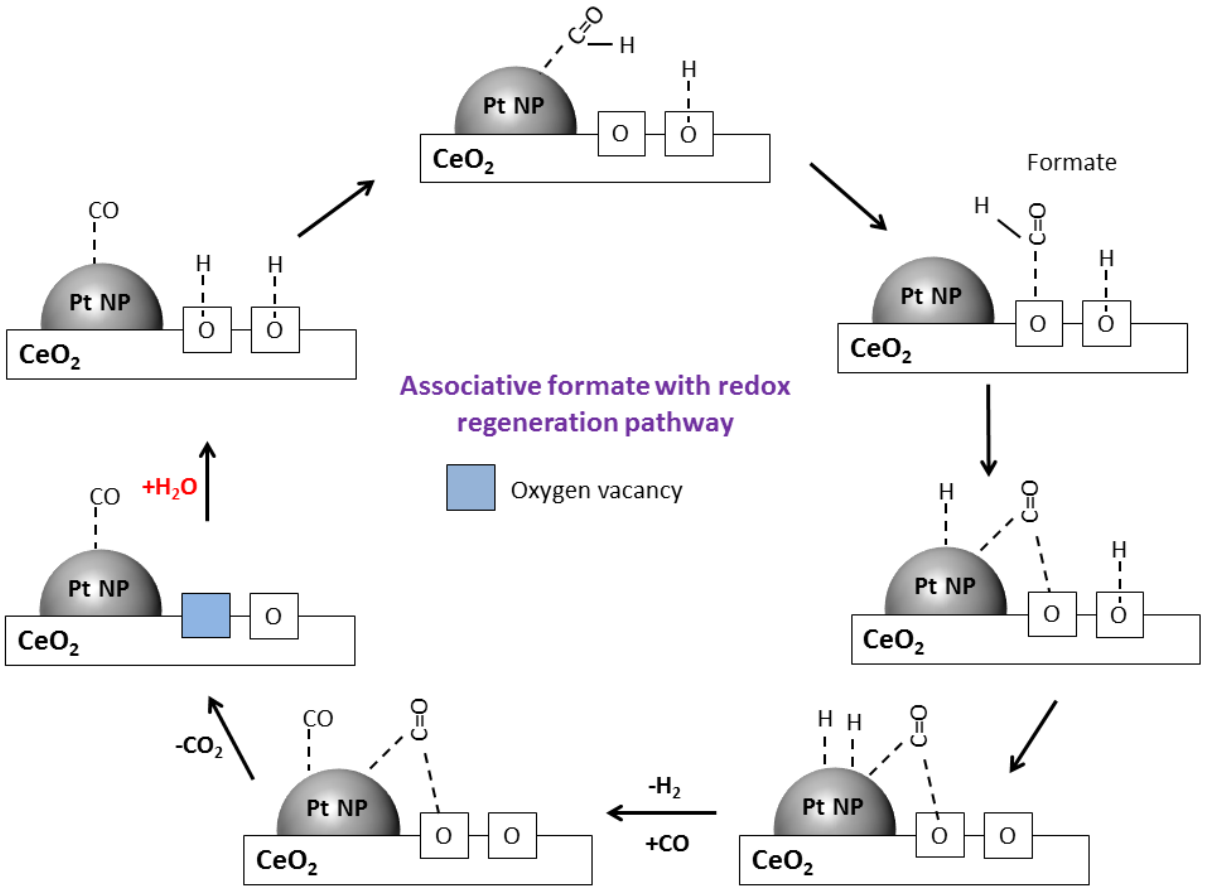

Supported platinum catalysts have been extensively investigated for low-temperature WGS due to their high activity and several experimental and theoretical works discussed about the key factors possibly involved on the reaction pathways. Concerning the Pt phase, the activity has been related to characteristics such as the particle size and coordination of the exposed Pt atoms (also related to their electronic properties), loading (which may actually dictate the size of crystalline domain) [28,50,51,55,58] and the effect the metal can exert on the support (metal-support interaction enabling charge and/or oxygen transfer) [57,59,60].

Regarding the support, WGS mechanism would be intrinsically dependent on the nature of the metal oxide, the surface properties (availability and reactivity of hydroxyl groups), oxygen vacancies amount and ease of formation, interaction with metallic phase (spillover of surface species to the metal and charge/oxygen transfer), which are often associated in literature to the surface area and crystalline domain size of support. Reducible oxides have demonstrated a direct participation in the increased activity observed for Pt catalysts for WGS reaction, since Pt (bulk) itself does not react with water at the usual reaction conditions [52,61]. The presence of the non-stoichiometric oxide would assist the water activation step, which would occur in the oxygen vacancies or in their vicinity, and/or provide

surface OH groups, dictating the preferred reaction pathway (redox or associative) [31,45,61–65]. The support may also influence in the electronic properties of the metallic phase, modulating the bond strength of reactants and products, which was also reported to occur with Pt when in close contact with highly oxophilic metals [55,60,63,66].

In general, WGS activity is related to enabling optimized CO adsorption strength and the activation of water, as well as favoring the oxygen transfer from water to CO, whether through the oxide lattice or from a surface hydroxyl. In both cases, the interaction between metal and oxide is essential to favor the encounter of reactants and formation of intermediates and the interfacial metal-oxide sites are currently believed as the true active sites for WGS reaction [50], and the catalytic performance would be strongly dependent on the availability of such sites.

For the design of Pt catalysts for WGS reaction, one promising reducible oxide is vanadium oxide, which presents a variety of oxidation states, high oxygen mobility and has been applied to catalyze oxidation reactions. These oxides were reported as effective promoters in several studies especially focused on the transformation of hydrocarbons to olefins, by dehydrogenation, or to CO_x and H_2 through oxidation reactions [67–69]. For instance, when $VO_x/Pt/Al_2O_3$ catalysts were applied to propane total oxidation, it showed a higher catalytic activity compared to Pt/Al_2O_3 [70]. Moreover, when a WGS stage was integrated to ethanol oxidation, the V addition to the WGS Pt/CeO_2 catalyst enhanced the activity [71]. The effect of vanadium as promoter has demonstrated to be dependent on the nature of the support, as suggested by Vining *et al.* [72] for methanol oxidation reaction to produce formaldehyde. The comparison of catalysts composed of VO_x grafted on SiO_2 and over CeO_2/SiO_2 showed a remarkable increase in methanol conversion for the $VO_x/CeO_2/SiO_2$ catalyst. Furthermore, the promoting effect of vanadium seems to rely on the VO_x species formed over the support surface; Kilos *et al.* [73] showed that when tridimensional structures were created, they affected the accessibility of ethanol to the active sites of VO_x/Al_2O_3 catalysts, thus decreasing the turnover rates for ethanol oxidative dehydrogenation to acetaldehyde. On the other hand, the presence of vanadium in CeO_2 catalysts has increased the stability towards Cl poisoning when applied to the combustion of chlorobenzene [74].

Thereby, the deposition of dispersed vanadium species over metal oxides can play an interesting role in WGS reaction, an increase in catalytic activity was observed when vanadium was added to ZrO_2 and CeO_2 supported Pt catalysts, assigned to the increased reducibility of the support [75,76]. Such strategy could also be promising for glycerol decomposition on GSR reaction, since VO_x species are active for selective dehydrogenation of alcohols and could assist H_2 generation by enhancing WGS step.

Another active support is cerium oxide, widely explored in catalytic systems [77,78] due to its influence on dispersion, reduction/oxidation and thermal stability of the supported

metal phase, usually attributed to the strong metal-ceria interaction. Additionally, it is well established that CeO_2 is not a mere support for the metallic phase [59,79], its characteristics such as the oxygen storage capacity, the availability of oxygen vacancies on the surface and in the bulk, the wide array of feasible mixed oxides [80] contribute to its exploitation as an active support on catalytic reactions. Recently, due to the promising catalytic activity exhibited by ceria, parameters as the loading, particle size, exposed crystal planes and charge transfer to the metal phase have been investigated [41,62,81–88]; however, to tackle the key properties driving high catalytic activity is still a challenge. Additionally, the metal-ceria interaction has been on the spotlight and several works have demonstrated that such interface is determinant (if not the active site) on WGS reaction mechanism [39,43,49].

Despite all the efforts, several aspects of ceria role on the reaction pathways still remain unclear. An example is the variation of the electronic and structural properties of CeO_2 nanoparticles (NPs) with different size, in the range of a few tens of nanometers. It has been reported the difference between CeO_2 NPs with 3 and 120 nm in catalytic activity [81], however the size effect of CeO_2 NPs within 20 nm with narrow size distribution has not been experimentally reported until now. Additionally, CeO_2 NPs with different size may present distinct properties that would have an impact on WGS reaction. It was reported by Huang and Beck [62] that the reactivity of ceria surface OH groups, determinant in such reaction despite the major mechanism, is dependent on the size of CeO_2 clusters. The theoretical data showed that very small clusters could be active even without the presence of a supported metal phase. It has also been demonstrated that Pt-CeO_2 interaction can be modulated according to CeO_2 size, which in turn can change the reactivity of active sites. Vayssilov *et al.* [87] when comparing two CeO_2 clusters (one with 21 Ce atoms and the other with 40) interacting with Pt NPs, discovered that the energy to form an oxygen vacancy on ceria is reduced for the smaller CeO_2 cluster. Thus, the size of CeO_2 NPs is an important factor to be investigated, being intimately related to the catalytic performance by modulating the strength and geometry of reactants adsorption, ease of product desorption, oxygen transport through the structure and reactivity of surface -OH groups, interaction with metallic NPs and their thermal stability. In this sense, the investigation of catalysts composed of dispersed CeO_2 NPs with different mean sizes (within 20 nm regime) and its effect on reactions as WGS and GSR can contribute to better understand the determinant properties of ceria for rational development of catalysts with optimized performance. Since Pt/CeO_2 catalysts have demonstrated high activity on WGS reaction [41,45,61,89,90] and also offer challenging aspects to be investigated, this is a promising system to be explored for H_2 generation.

Once WGS catalytic systems were briefly described, a more specific discussion about the metallic phase is depicted. Currently, the majority of works studying Pt catalysts for

WGS reaction essentially attempt to correlate reaction rates to properties as the Pt loading, particle size, metal dispersion and oxidation state. However, if one wants to identify true active sites, for example, such parameters must be carefully thought since they are interconnected. For instance, as in the case of increasing Pt loading, depending on the support, there would be the formation of larger Pt crystalline domains provided the interaction with the support is not stronger than Pt-Pt interaction, thus the metal dispersion over the surface will decrease with larger particles. Despite the increase in metal content, there will not be a corresponding creation of additional exposed metallic sites, since their amount is lower for larger nanoparticles.

A more fundamental outcome of the variations in metal loading and particle size (and thus in metal dispersion) is the availability of exposed metal sites, the ones accessible to interact with the oxide and reactant molecules. At a given metal content, with smaller metallic domains the fraction of exposed atoms on the surface of the particle is higher, meaning more metal atoms can act as active sites, as shown in Scheme 2.3. The shape of the particle also affects the number of exposed atoms on the surface. Within a particle, the exposed atoms have different coordination, at edges and corners each atom is coordinated with less equal atoms than at terrace sites, and the proportion of such low-coordination sites decreases with the increase in particle size (Scheme 2.4). Herein, it will be adopted the denomination of highly under-coordinated sites (HC, coordination lower than 6 atoms), under-coordinated (UC, coordination of 6-7) and well-coordinated (WC, coordination of 8-9 atoms) [91].

Scheme 2.3: Geometric models of the fraction of well-coordinated (WC) and undercoordinated (UC) sites as a function of particle diameter for cuboctahedron, icosohedron and cube nanoparticle shapes (reprinted with permission from Kale *et al.* [91]).

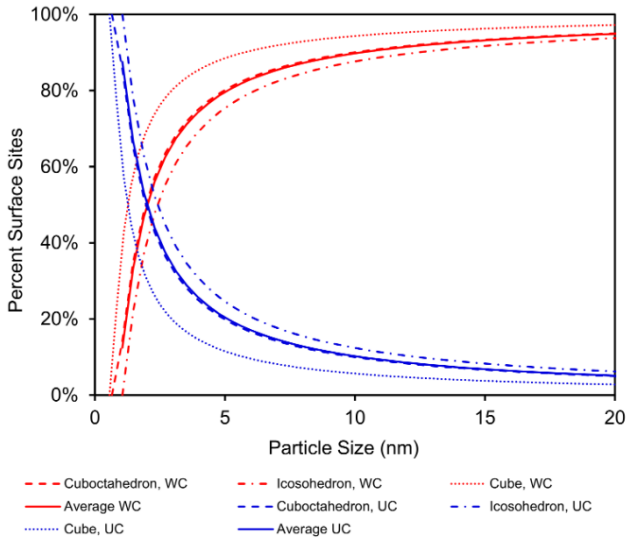

Scheme 2.4: Illustration of distinct Pt sites within a NP for model cuboctahedral (Pt_{55}) as well as polyhedra NPs of different sizes: Pt_{116}, Pt_{201}, Pt_{432}, Pt_{901} and Pt_{1214} (Reprinted with permission from Lentz *et al.* [92])

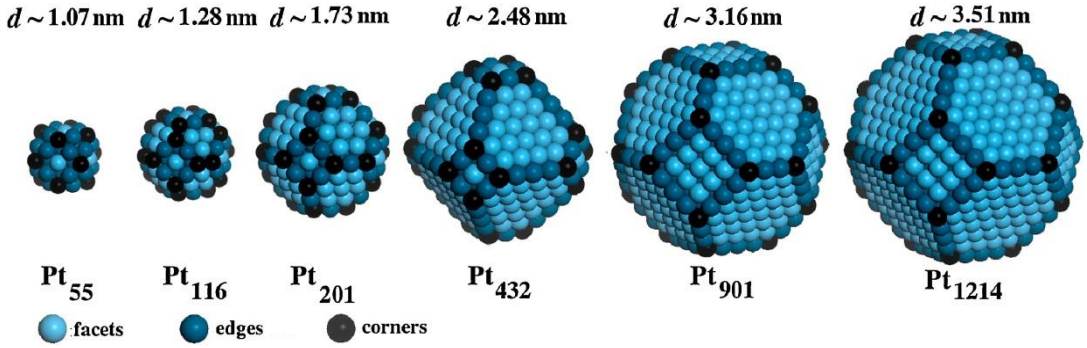

The experimental distinction between metallic sites within a particle is a challenging task and the difficulty drastically elevates in the analysis of real samples with common heterogeneity in particle size and shape. Nonetheless, the participation of these low-coordination metal sites (HC and UC) have been suggested for WGS reaction by few works, being more active towards water activation and in close contact with the active support, and their cooperation seems to rely on reaction conditions [50,90,93]. For example, Petallidou *et al.* [90] investigated a 0.5 %wt. $Pt/Ce_{0.5}La_{0.5}O_{2-\delta}$ catalyst during WGS reaction by isotopic transient Diffuse Reflectance Infrared Fourier Transform Spectroscopy (DRIFTS) and suggested that HC and UC Pt sites are involved in the formation of active reaction intermediates, whereas WC Pt sites do not participate in the formation of carbon intermediates. The same trend was also proposed by Aranifard *et al*. [50] in the study of Pt/CeO_2 catalyst mentioned earlier. The authors suggested that HC Pt sites would strongly bind CO and these co-adsorbed CO would increase the CO reactivity over the others HC Pt atoms in close contact with ceria (Scheme 2.5). These interfacial centers would participate in the reaction mechanism, whereas the co-adsorbed CO on the adjacent Pt sites would merely assist in the reactivity of interfacial centers.

In the same trend, Stamatakis *et al* [93]*.* investigated Pt surfaces using DFT and kinetic Monte Carlo simulation and demonstrated that all terraces and step Pt sites would contribute to the reaction mechanism, however, at high H_2O:CO ratios, the activity of Pt step sites would be higher than terrace sites.

Recently, it has been demonstrated that despite achieving the fine tuning of metal and support properties to increase WGS reaction rates, such improvement is only possible if the odds of creating new interfacial sites are also higher [41,82]. In works involving catalysts with varied loading of metal or metal oxide as promoter, to address the change in reaction rates to a specific catalyst property is a challenging puzzle, and the global result

may be only a product of the increase in probability of creating additional interfacial sites with higher loadings.

Scheme 2.5: Illustration of Pt/CeO_2 interfacial sites with adsorbed CO on HC sites (reprinted with permission from Aranifard *et al*. [50]). Cream, red, and navy balls represent Ce, O, and Pt atoms, respectively, while white and gray balls represent H and C atoms. In the notation, the interfacial oxygens (O_{int}) are those top layer oxygen atoms that are nearest neighbors to the Pt cluster, while surface oxygens (O_s) are all other top layer oxygen atoms. The highlighted areas correspond to the initial active site (*Pt–O_{int}), where the empty Pt site corresponds to a Pt–Pt bridge site.

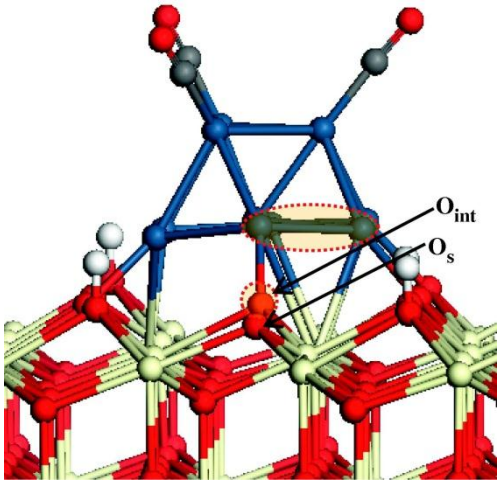

Another important issue about the activity of Pt catalysts for WGS reaction is their deactivation with time on stream, a drawback for industrial applications. The main cause of such phenomena is CO-poisoning of the metallic phase or coke formation. The latter is often less common in the presence of reducible oxides. CO poisoning would be provoked in catalysts in which Pt binds CO strongly, hindering its desorption as CO_2, often observed in cases where the oxygen transfer from support is not possible or have low rate [57,60,66]. CO poisoning is also reported to occur more often in low-coordination Pt sites, especially without direct interaction with the metal oxide support [50,93]. For both coke and CO poisoning, the presence of reducible oxides interacting closely with Pt greatly diminishes deactivation. However, depending on the support, another cause for catalyst deactivation during WGS reaction is related to the stability of the carbon intermediates formed over the surface (especially carbonates), thus blocking the active sites. Such species have been reported to be very stable over some Pt supported catalysts, especially containing oxides with basic-nature surface, as CeO_2 [28,65,89,94,95]. Despite such drawback on ceria catalysts, their high activity towards WGS reaction still motivates its application and studies are being conducted to minimize such effects, such as tuning the support properties by alkali-doping [40].

A valuable tool which can contribute to the comprehension of the catalytic pathways during WGS reaction, as well as probing catalyst surface properties is DRIFTS carried *in situ* (under reaction conditions), which allows the observation of surface reaction intermediates derived from the interaction of CO and H_2O molecules with Pt and ceria. Coupling DRIFTS with Modulation Excitation Spectroscopy (MES) and the Phase Sensitive Detection (PSD) it is possible to distinguish the active reaction intermediates species from the spectators and enhance significantly the signal to noise ratio of the spectra [96–98].

2.2 GSR REACTION

As GSR reaction is another main topic of this work, a literature overview focused on the studied systems will be described.

Glycerol steam reforming is an endothermic reaction and it is usually reported at temperatures ranging from 400 to 800 °C; the production of H_2 is increased at higher temperatures and water to glycerol molar ratios [17]. The high concentration of water (water to glycerol molar ratios from 4 to 15) shifts the equilibrium towards reactants consumption and also assists the removal of coke from the catalyst surface by coke gasification[15,99]. The maximization of H_2 generation and the suppression of byproducts formation strongly rely on the catalyst properties and reaction conditions, and the ability to promote selective bond scission (C-C, C-H and O-H instead of C-O) is also important to avoid catalyst deactivation. Thus, to favor glycerol decomposition and WGS reaction, metal-supported catalysts are usually employed to favor C-C bond scission (metal) and WGS step (by the oxide support for water activation).

The most explored metals in such bifunctional systems are Pt and Ni, whereas Ru, Rh, Co, Ir and the bimetallics Pt-Ni, Co-Ni, Ni-Sn, Pt-Re, Pt-Ru, Pt-Os were also reported in literature[19,22,24–27,100–110]. Glycerol decomposition on Pt and Ni is believed to occur by a series of dehydrogenation and decarbonylation steps, as shown in Scheme 2.6.

Scheme 2.6: Reaction pathways for glycerol decomposition over metal surfaces (Adapted from [6]).

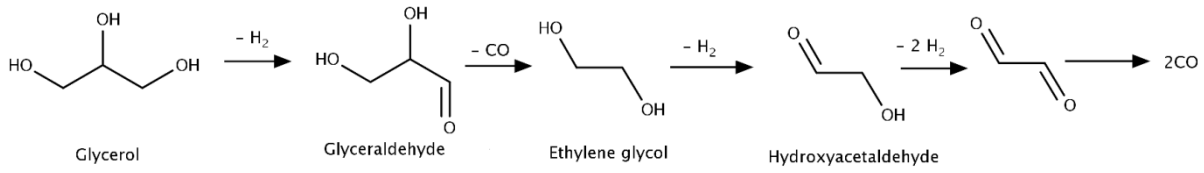

The resulting CO would then be oxidized to CO_2 by steam, forming additional H_2 through WGS reaction (Equation 1.3). The presence of CO and H_2 on stream could also favor the formation of methane, by methanation or Fischer-Tropsch reactions:

$$\boldsymbol{CO + 3H_2 \rightarrow CH_4 + H_2O \quad \Delta H = -206\ kJ\ mol^{-1}} \qquad \text{(Equation 2.1)}$$

$$\boldsymbol{2CO + 2H_2 \rightarrow CH_4 + CO_2 \quad \Delta H = -247\ kJ\ mol^{-1}} \qquad \text{(Equation 2.2)}$$

While both Ni and Pt can act in C-C cleavage, Ni is less expensive and would activate water more effectively than Pt due to the formation of $Ni(OH)_2$ and NiOOH species. However, Ni has also a higher activity towards C-O bond scission, usually leading to high amounts of methane and coke[6,23,102,111]. Thus, the use of Pt catalysts on appropriate supports often leads to less coke and byproducts, and the water activation drawback can be overcome by adding a metal oxide support to interact with Pt.

The nature of support on catalyst performance has been reported as determinant to improve thermal stability (reduce sintering of the metal phase), to favor WGS step through water activation and to reduce the formation of byproducts and coke deposition (avoiding catalyst deactivation). The interaction with an active support as CeO_2 could also modify the electronic properties of Pt and as a consequence its reactivity towards glycerol and the carbon intermediates formed on the surface, compared to the bare metal. Once glycerol is decomposed, the oxide may promote a weaker binding of the product CO on interface Pt sites, increasing its reactivity and also facilitate its removal as CO_2 by WGS step, therefore improving Pt resistance to CO poisoning. Such behavior, as the weaker Pt-CO bond and promotion of WGS reaction during aqueous phase reforming of glycerol was reported by Liu *et al.*[112], when an oxophilic element (Mo) was added to Pt catalysts.

Besides the high metallic dispersion provided by supports presenting strong metal-support interaction, the intrinsic property of metal oxide as support or even promoter is the surface nature, regarding its acid-base properties and degree of hydroxylation [113]. It has been extensively reported in literature the effect of different supports on glycerol conversion, H_2 selectivity and catalyst stability towards deactivation (whether by metal sintering or coke formation) [22,24,26,27,100–103,107], however, not many studies analyzed in depth the intrinsic properties of the metal oxide that led to distinct reaction pathways in this reaction.

The interaction of glycerol with metal oxides with distinct properties was reported by Copeland *et al.*[113] by DRIFTS experiments. It was shown that the polyol molecule interacted more strongly with oxides whose surfaces presented strong Lewis acid sites (CeO_2, Al_2O_3, ZrO_2, TiO_2) by forming a multidentated alkoxyde by terminal hydroxyls, even in the presence of water. With an oxide with more basic nature, MgO, glycerol would only

weakly interact with the surface through hydrogen-bonding. Accordingly, the importance of Lewis acid sites has been demonstrated by the analysis of byproducts formed by lateral reactions during GSR reaction.

For instance, alumina (in different structures, alpha, gamma) is widely used as support in reforming catalysts due to high surface area, mechanical, thermal and chemical stability. Yet, its acidic nature often leads to carbon deposition from lateral byproducts formed under GSR conditions. For this reaction, in an attempt to reduce coke formation in a NiSn bimetallic catalyst, Bobadilla *et al.*[103] tuned the support acidity by adding 10 and 30% wt of MgO to γ-Al_2O_3. The authors observed that the addition of MgO reduced the amount of acid Lewis sites and suppressed the formation of liquid byproducts. With 10 %wt of MgO, the formation of coke was the smallest, and conversion of glycerol to gas products and H_2 production were the highest, possibly due to the formation of well dispersed Ni from Ni-$MgAl_2O4$ formation. Without MgO, $NiAl_2O_4$ was formed, hindering active Ni sites and producing coke, whereas 30% wt of MgO led to sintering of Ni particles and catalyst deactivation.

Rossetti *et al.* [24] tested Ni catalysts prepared by impregnation on ZrO_2, TiO_2 and SiO_2 for GSR reaction. Again, the formation of Ni over supports with very distinct properties led to a difficult evaluation of the acid-base nature of the surface. The variations on catalytic performance on GSR reaction (all catalysts showed carbon deposition and deactivation) were mostly attributed to the strength of metal-support interaction, which led to different formation of Ni domains.

Pompeo *et al*. [100] prepared Pt catalysts over SiO_2, ZrO_2, Al_2O_3 and CeO_2/ZrO_2 for GSR reaction, with Pt domains ranging from 2 to 4 nm. The acid-base properties of the surfaces were determined and SiO_2 showed a neutral characteristic, while the others were acidic in nature. Catalyst deactivation and formation of byproducts derived from lateral reactions (dehydration, hydrogenolysis and condensation) were identified for all samples except Pt/SiO_2.

Also for GSR reaction, Kim *et al.*[102] impregnated Ni over SiC, Al_2O_3 and CeO_2 supports and demonstrated the stable and high (90%) glycerol conversion to gas products (H_2 and CO, no WGS activity), as well as no byproducts over Ni/SiC catalyst. For Pt/Al_2O_3 and Pt/CeO_2 samples it was observed the occurrence of lateral reactions (glycerol dehydration and condensation over acidic and basic sites, respectively). These samples, although presenting higher WGS activity, suffered from deactivation due to coke formation.

Sad *et al.* [101] studied Pt catalysts over SiO_2, Al_2O_3, TiO_2 and MgO for GSR reaction. The samples were prepared from Pt impregnation, and the metallic dispersion was similar for all samples (from 35 to 45%) except Pt/MgO (11%). Surface acidity measurements showed higher acidic nature for Pt/Al_2O_3 and Pt/TiO_2, which in turn exhibited low conversion

of glycerol to gas products (10 and 20%, respectively) and high formation of byproducts. Although TiO_2 is known for its redox properties which can promote WGS reaction, Pt/TiO_2 catalyst did not show high H_2 selectivity due to the occurrence of parallel reactions and catalyst deactivation. The complex chain of reactions that can take place during GSR reaction, depending on the catalyst nature, can be exemplified as illustrated in Scheme 2.7.

Scheme 2.7:Glycerol reaction chain (reprinted with permission from [101]).

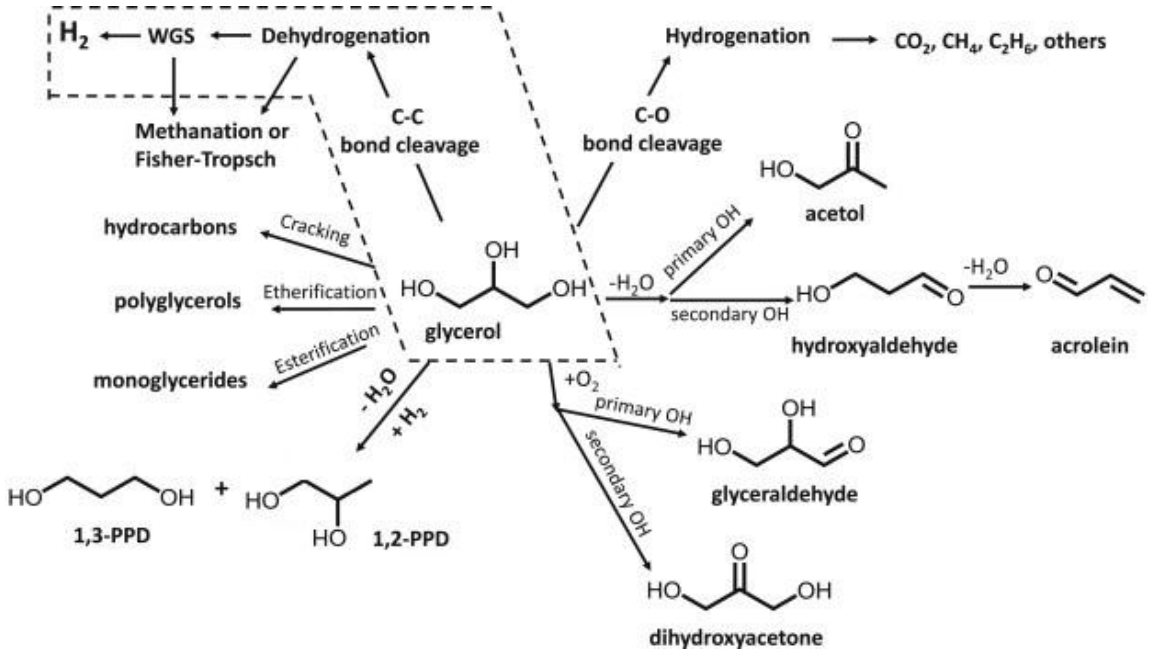

One of the parallel reactions that often occur over acid supports during GSR reaction is glycerol dehydration. Foo *et al.* [114] investigated this step experimentally and theoretically over niobium oxide surface, which possesses both Lewis and Brønsted acid sites. By blocking selectively one of them (Brønsted ones) with Na^+ ions the authors could elucidate the role of each type of site. It was found that glycerol would chemisorb on the oxide through a primary hydroxyl with a Lewis acid site, then subsequently both Lewis and Brønsted sites could promote dehydration on the coordinated hydroxyl group, leading to the formation of hydroxyacetone. The dehydration of glycerol over the secondary hydroxyl would occur preferentially on Brønsted sites, forming 1,3-propenediol, which is further dehydrated to acrolein. The authors also demonstrated that when more than one monolayer of glycerol was present over the surface, aromatic compounds could be formed, possibly by condensation reactions. The illustration of the dehydration process of glycerol can be found in Scheme 2.8.

Scheme 2.8: Glycerol dehydration reaction over Lewis and Brønsted acid sites (LAS and BAS, respectively, reprinted with permission from [114]).

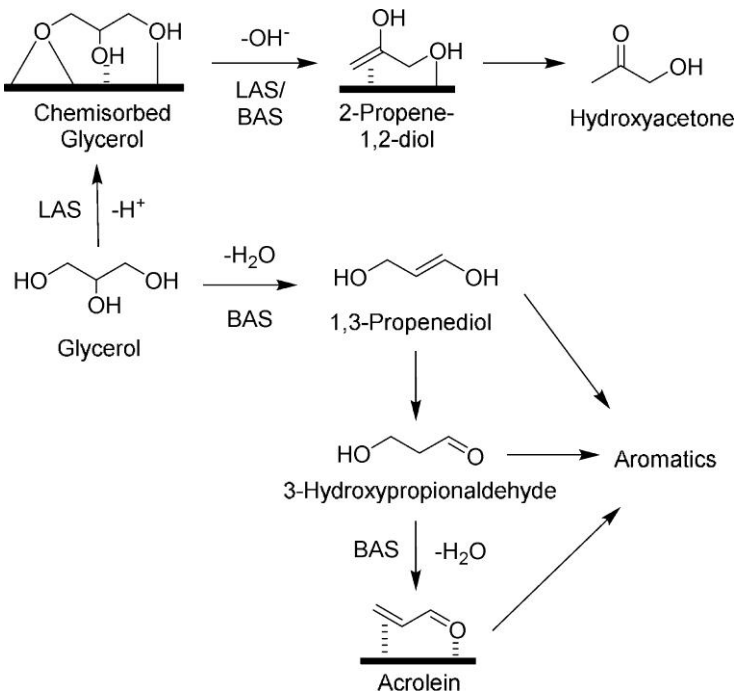

Therefore, a great effort has been destined to understand the role of support on GSR reaction, and to tackle this effect independently, focusing on the intrinsic nature of the metal oxide is yet challenging. The aforementioned works provided insights of how to increase glycerol conversion to gas products and reduce the formation of byproducts (using supports with neutral surface characteristics as SiO_2, SiC), however H_2 selectivity was not maximized since the these supports do not promote WGS reaction. When supports known to promote WGS reaction were employed, lateral reactions occurred and catalyst deactivation was observed. About the latter, it was often associated with both formation of carbon deposits from byproducts decomposition, as well as the sintering of the active metallic phase. The metal-support interaction was mostly responsible for the stability of the metal phase. The literature thus showed that there must be a compromise between H_2 maximization by promoting WGS reaction and avoiding catalyst deactivation.

Besides the design of catalysts, the performance observed during GSR reaction is extremely dependent on the conditions the tests are performed. For instance, the H_2 yield is increased through glycerol decomposition at higher temperatures (above 500 °C), however WGS reaction is disfavored. Glycerol concentration on the solution feed (water to glycerol ratio) and feed flow rate are also crucial, as well as the catalyst to glycerol weight ratios. In literature, catalytic tests are run with glycerol concentration varying from crude glycerol from biodiesel byproduct (60 to 80% wt) to 10% wt in water, with feed flow rates ranging from

0.08 to 1 mL min^{-1}, while catalyst mass varies from to 0.035 to 1g [26,100–102,115]. Thus, the comparison of catalytic performance even for systems with relatable components is difficult.

2.2.1 Distinct Pt sites on GSR

As discussed earlier, several works showed the dispersion of metallic phase as an important parameter to promote catalyst stability, but evaluation of an independent factor is not straightforward with varying support nature, metal loading and catalyst preparation method.

As illustrated in Scheme 2.6, glycerol decomposition reaction on monofunctional Pt catalysts were described as occurring through dehydrogenation and decarbonylation steps, first C-H bonds would be cleaved before C-C scission, with few or barely none C-O bond breaking, resulting in H_2 and CO when WGS reaction is not promoted.

Rezende *et al.*[116] suggested that the lower carbon deposition observed on a sample was due to the smaller Pt NP size (with 3 nm, observed by TEM after GSR tests), the catalysts with higher amounts of carbon showed sintered particles. The authors suggested the highly dispersed Pt NPs were essential to the *in situ* decomposition (burn off, cleaning) of carbon deposits on the metal sites.

Zamzuri *et al*.[27] impregnated Ni over various support, with distinct surface areas, and Ni/Al_2O_3 catalyst showed the highest glycerol conversion and H_2 selectivity, compared to La_2O_3, ZrO_2, SiO_2 and MgO. The tests were performed using 300 mg of catalyst, from 600 to 700 °C and water to glycerol ratio of 9, 1 mL min^{-1} solution feed. Under such reaction conditions the acidity of alumina support seems to play a minor role, being suppressed by the high Ni dispersion (4 nm, XRD) over the surface when compared to the other oxides (15-30 nm). Besides being another suggestion of the effect of dispersed metal sites on catalyst activity, this work is an example that catalyst performance and the effect of each property is deeply intertwined with reaction conditions.

The size of Pt NPs has been suggested as an important parameter on catalysts for glycerol transformation reactions. Cifti *et al*.[117] studied the aqueous reforming of glycerol over Pt catalysts with varied sizes and Re loadings. They found out the monometallic catalyst with 2 nm Pt NPs showed higher H_2 production rates and WGS activity; the authors attributed this better performance to the increased fraction of step-edges Pt sites on the catalyst, which in turn would present lower activation barrier for water activation and C-C cleavage. The samples containing Pt NPs smaller than 2 nm would not present higher activity due to the decreased fraction of step-edge sites[118]. The effect of Pt domain size was also proposed by Pompeo *et al*.[100], who suggested that Pt face sites (WC sites) would be the responsible to cleave C-C bonds, since the catalyst with larger Pt crystalline domain exhibited higher glycerol conversions. However, the work did not discuss about the size distribution of such Pt

particles, which probably exhibited a broad size distribution and thus several HC and UC sites. Later, another work was published containing authors in common[119], which claimed that smaller Pt NPs (1-2 nm, obtained by Pt precursor impregnation over the supports) on a modified SiO_2-Carbon support would boosts C-C cleavage and also avoid the formation of coke precursors and their deposition.

Additionally, a DFT study conducted by Tereshchuk *et al*.[120] on glycerol adsorption over a defected Pt_6/Pt(100) surface showed that the polyol would bind preferentially on the low-coordinated Pt atoms (lower energy configuration), compared to terrace Pt sites; however, it points out that the other higher energy isomers can be formed on high temperature conditions (as during the GSR reaction).

Analogously, the decomposition of ethylene glycol (simplest biomass-derived polyol) on terraced and stepped Pt surfaces, namely Pt(111) and Pt(211), respectively was studied by Gu *et al.*[121], and it was demonstrated by DFT that the products would mostly be CO and H_2 for both surfaces and the first steps of decomposition would be the dehydrogenation reactions, with stronger binding energies for intermediates from C-H bond cleavage than from C-O. Dehydrogenations would have lower barriers than the breaking of C-C and C-O bonds, and the transition state energy related to C-C cleavage would be lowered with further ethylene glycol dehydrogenation steps, while for C-O the energy would decrease and then increase. On Pt(211), the reaction intermediates would bind strongly, resulting in lower effective activation barriers on the stepped surface. Therefore, the stepped surface would exhibit a more effective CO poisoning, however, if WGS reaction can take place, this effect could be mitigated and thus the stepped surface would show increased activity. Recently, Mahmoodinia *et al*.[122] suggested the same preference on bond scissions for ethylene glycol, and also demonstrated that the cleavage reactions would occur more favorably on a Pt_{13} clusters than on a Pt surface. Interestingly, the same preference towards dehydrogenation of glycerol before C-C and C-O bond cleavage was identified by Liu and Greeley[123] for Pt(111) surface.

A method to quantify the relative proportion of distinct types of sites on Pt NPs regarding their coordination was reported by *Kale et al.* [91]. The authors estimated the fraction of WC and UC sites from the relative areas of the bands attributed to CO linearly bound to Pt sites on the DRIFTS spectra during CO adsorption experiments. Hence they correlated the fraction of WC and UC sites with geometric models considering different shapes and sizes of Pt NPs. The estimated size and shape of Pt NPs obtained by TEM measurements fairly agreed with the ones obtained by this analysis.

2.2.2 CeO_2 role on GSR

Despite most of the works described so far showed a poor activity of CeO_2 catalysts towards GSR reaction due to byproducts formation, it is still a very promising promoter if the adequate tuning of its properties can be achieved. As Copeland *et al*. [113] demonstrated, CeO_2 itself can interact with the polyol (Ce cations would interact with glycerol terminal OH groups) and although it has not been evidenced that such interaction could promote the scission of C-C, C-H or C-O bonds, it may facilitate such steps to be performed by Pt at the interface.

With the lack of information regarding glycerol-ceria interaction, studies with ethylene glycol again can be useful to understand this interplay. Chen *et al*.[124] studied the adsorption of ethylene glycol ($OHCH_2CH_2OH$) over fully oxidized CeO_2(111) and reduced CeO_x(111). It was shown that the molecule interacts through the two hydroxyl groups forming ethylenedioxy and surface hydroxyls on both ceria surfaces. TPD experiments up to 800 K showed that over CeO_2(111) the C-C bond would break, forming formate intermediates which would later become CO, CO_2, H_2 and H_2O. The cleavage of C-O bonds could also occur, forming acetaldehyde, ethylene and acetylene. Over CeO_x(111), dehydration would be favored with ethylenedioxy mostly converted to acetaldehyde, ethylene and acetylene (also with H_2 and O_2). These dehydration products would occur since C-O bond cleavage would be favored instead of the C-C one due to the competition for oxygen between the reduced surface and the adsorbed molecules. At 400 °C (623 K), all the dehydration products were formed, (even for CeO_2(111), however in small amounts, together with H_2).

Thus, since it was reported by Copeland *et al.*[113] that glycerol would interact with ceria by the terminal OH groups (as ethylene glycol would do), analogously for our ceria catalyst under GSR reaction it is possible that C-C, C-H and C-O bond scission could occur, regardless of the ceria reduction degree.

Concerning CeO_2 loading, high amounts of CeO_2 and even bulk CeO_2 have shown to favor the deactivation of the catalyst due to the formation of byproducts. Iriondo *et al.*[25] have shown that at 500 °C, higher loadings of CeO_2 added on Ni/Al_2O_3 catalyst (8-17% wt) decreased glycerol conversion due to the formation of byproducts. The optimal tested loading was 5 % wt at a given feed flow rate and glycerol solution concentration. The conversion decreased with increasing ceria loading, since at 500 °C the byproducts would not be reformed further, blocking the active sites and hindering C-C cleavage. When the temperature was increased to 600 °C, such intermediates could then be mostly transformed to H_2 and CO_2, especially for the catalyst without ceria.

Doukkali *et al*.[125], however, found out that the addition of 10 % wt of CeO_2 over Pt/Al_2O_3 (2.5% wt Pt) catalyst decreased the formation of byproducts at 400, 450 and 500 °C, because ceria would cover part of the highly acidic alumina surface. Accordingly, in a study

conducted by Montini *et al*.[22], ceria was added to Pt/Al_2O_3 catalyst and the results were the increase of H_2 fraction at lower temperatures, higher stability and WGS enhancement compared to bare Pt/Al_2O_3.

Therefore, Pt/CeO_2 catalysts have demonstrated high activity on WGS reaction [41,45,61,89,90] and thus is a promising system to be explored for H_2 generation through GSR reaction. It has been demonstrated that the oxide on GSR catalyst has a fundamental role on the activity, influencing not only the glycerol conversion to gas products but also the H_2 selectivity and the variety of lateral reactions. The complexity of the glycerol molecule results in a gamma of byproducts, which are dependent on the reaction conditions (temperature, pressure, glycerol concentration, gas flow) and the catalysts composition[17,100].

For Pt-based catalysts for GSR reaction, silica has shown the best H_2 selectivity and smaller methane formation among the tested supported catalysts due to its decreased acidity, but it does not promote WGS reaction [100]. Tailoring support properties by adding CeO_2 to high surface area supports can be a promising strategy to enhance H_2 selectivity and catalyst stability.

Therefore, in the present work groups of Pt-based catalysts were investigated: one containing vanadium oxide and the other, ceria. Within the first group the influence of vanadium oxide at different loadings on the VO_x species formed on the catalyst surface were evaluated on GSR reactions. For the second group the catalytic activity was evaluated in terms of the nature of both Pt metallic phase and ceria.

Chapter 3

VO_x-Pt/Al_2O_3 SYSTEM

3.1 OVERVIEW

This chapter is an adaptation of the work published in the paper "VO_x-Pt/Al_2O_3 catalysts for hydrogen production", Tathiana M. Kokumai, Daniel A. Cantane, Guilherme T. Melo, Luigi B. Paulucci, Daniela Zanchet (Catal. Tod., 289, 2017, 249–257). The copyright clearance can be found in PUBLICATION LICENSES section.

Herein we detail the synthesis, characterization and catalytic performance of bifunctional VO_x-Pt/Al_2O_3 catalysts applied to WGS and GSR reaction and the correlation of catalyst properties with catalytic activity and H_2 selectivity.

3.2 ABSTRACT

Platinum supported catalysts are promising systems to a wide range of catalytic reactions involved in the hydrogen production chain. The performance of these catalysts can be enhanced by designing properly their nature, composition and structure. In this context, the addition of a second metal oxide on a catalyst composed of a well dispersed Pt phase over a high surface area support may be a powerful strategy. In this work we impregnated VO_x species over Pt/Al_2O_3 and evaluated the catalysts performance for water-gas shift (WGS) and glycerol steam reforming (GSR) reactions. The catalysts characterization showed that VO_x species formed over the Pt/Al_2O_3 surface were not deeply affected by the loading in the range of 0.5-2.0 V atoms per nm^2 and were reduced at mild temperatures. *In situ* measurements during catalysts activation and WGS reaction showed that VO_x species presented mixed valence (V^{3+}/V^{4+}) while Pt was in metallic state. The addition of vanadium increased Pt/Al_2O_3 WGS activity; however, the improvement did not linearly correlate with the loading. Under GSR, the results indicated that the WGS step was favored by the presence of vanadium but the selectivity to H_2 decreased, which could be attributed to the parallel reactions enhanced by the acidic nature of the VO_x sites.

Keywords: Platinum catalysts; vanadium oxides; water-gas shift reaction; glycerol steam reforming

3.3 GRAPHICAL ABSTRACT

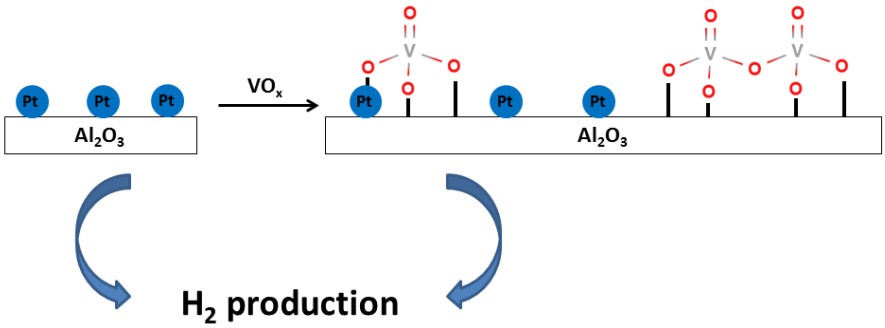

3.4 MATERIALS AND METHODS

3.4.1 CATALYST PREPARATION

The chemicals were used as received, without any pre-treatment. The support γ-Al_2O_3 was synthetized by the sol-gel method previously described [126]. Briefly, aluminium tri-sec buthylate (*Merck*, 97%) was stirred with ethanol and water at 80 °C for 1 h, then a certain amount of 0.1 mol L^{-1} HNO_3 solution was added and the system was kept under reflux for 14 h. The formed gel was dried at 110 °C overnight and calcined under synthetic air flow at 500 °C, 4h.

The Pt/Al_2O_3 catalyst (nominal 1% wt) was synthetized by wet impregnation. One gram of the γ-Al_2O_3 support was added to an ethanolic solution containing 0.025 g of $H_2PtCl_6.H_2O$ (*Umicore*, 40% Pt *basis*) and the dispersion was stirred in a rotary evaporator for 4 h. The ethanol was evaporated in vacuum; the solid was dried at 110 °C overnight and then calcined again under synthetic air flow at 500 °C, 4 h. The catalyst was labeled **PtAl**.

The VO_x-Pt/Al_2O_3 catalysts were prepared by wet impregnation of **PtAl** by adding 41, 82 and 163 mg of NH_4VO_3 (*Aldrich*, >99%) dissolved in 80 ml of deionized water, to result in three catalysts with different loadings of vanadium (1.8, 2.5 and 6.6 V % wt / g_{cat}, respectively). After stirring and solvent evaporation, the solids were dried and calcined as before. The final catalysts were labeled **05VPtAl**, **1VPtA**l and **2VPtAl,** and generally addressed as **xVPtAl**. For comparison, a **1VA**l sample was prepared in similar way without adding the Pt precursor.

3.4.2 CHARACTERIZATION

Powder X-ray diffraction (XRD) was measured in a Shimadzu XRD7000 equipped with Cu target (Kα=1.5406 Å), operating at 40 kV and 30 mA. Vanadium and platinum loadings were obtained by X-ray fluorescence (XRF) in a Shimadzu XRF1800. The surface area of the **PtAl** catalyst was obtained by the Brunauer–Emmet–Teller (BET) method

in a Quantachrome Nova 4200 by N_2 adsorption at – 196 °C, after pre-treatment at 150 °C by 24 h.

Temperature programmed reduction (H_2-TPR) was conducted in a Micromeritics AutoChem 2920 equipped with a U-tube reactor. Thirty mg of catalyst were treated under N_2 flow for 30 min at 200 °C, cooled to room temperature and heated to 1000 °C, at 10 °C min^{-1} under 30 mL min^{-1} of 10% H_2/He. The H_2 consumption was quantified by a thermal conductivity detector (TCD) detector and a calibration curve. The signal obtained for the bare alumina support was subtracted prior the analysis.

In situ X-ray absorption fine structure (XAFS) spectra at V K-edge (5465 eV) and Pt L_3-edge (11564 eV) were obtained at XAFS2 beamline at the Brazilian Synchrotron Light Laboratory (LNLS), Campinas, Brazil. The samples packed in pellets were mounted in a home-made furnace connected to a gas flow system, working in transmission mode. Catalyst activation was conducted under 2.5% H_2/He flow, 100 mL min^{-1} and the WGS reaction was conducted using CO:H_2O vol. ratio of 1:3 and total flow of 100 mL min^{-1}. To help the identification of the intermediate V species, bulk V_2O_5 reduction was conducted and the X ray absorption near edge structure (XANES) data was analyzed by the methodology described by Wong *et al.* [127]. Briefly, the spectra obtained at selected temperatures were compared to V references compounds. After attributing the selected spectra to a known vanadium oxide phase (V_2O_5, V_4O_7, V_2O_4, V_2O_3 and VO), the identification of V species in the **xVPtAl** catalysts was done. XANES and EXAFS data analysis were performed with Athena and Artemis codes within Demeter package following the standard procedures for alignment, normalization and background removal [128]. The value of passive electron reduction factor (S_0^2) was obtained from fitting Pt standard and the value was fixed in the analysis of the samples. The structural parameters: average coordination numbers ($CN_{Pt\text{-}Pt}$ and $CN_{Pt\text{-}O}$ corresponding to Pt-Pt and Pt-O scattering, respectively), interatomic distance (R) and Debye-Waller factor (σ^2) were obtained from the fittings; the reported Fourier transform of the EXAFS spectra and best fits are not phase corrected. The theoretical model for the Pt^0 reference was built based on the bulk Pt fcc structure.

Pt metallic dispersion was estimated the structural data obtained by EXAFS analysis using the following expressions [129]:

$$CN_{Pt-Pt} = \left[1 - \frac{3}{4}\left(\frac{r}{R}\right) + \frac{1}{16}\left(\frac{r}{R}\right)^3\right] N_{bulk} \qquad \text{(Equation 3.1)}$$

where:

$CN_{Pt\text{-}Pt}$ = average coordination number for the first coordination shell found experimentally;

r = interatomic distance for the first coordination shell found experimentally ($R_{Pt\text{-}Pt}$);

R = nanoparticle radius;

N_{bulk} = 12 for fcc Pt

Since the NP diameter (D) is twice its radius (2R), it is possible to calculate Pt dispersion using the experimental value found for D. The dispersion corresponds to the percentage of Pt atoms at the surface in relation to the total number of atoms in the volume of a NP (n). This amount is the ratio between the NP volume and the Pt atom volume (considering that the atom diameter is twice the Pt metallic ratio and equal to 1.38 Å): $n = D^3/d^3$.

The surface area of a spherical NP is $4\pi D^2$. One atom at the surface contributes with πD^2 from this surface area which corresponds to the area projected at the surface. Hence, the number of atoms at the surface (N) is $N = 4D^2/d^2$. Thus, the dispersion (Di) is given as $Di = (N/n) * 100$. It is important to note that the Pt metallic dispersion (Di) estimative is obtained without taking Pt-O contributions that are considered to be on the surface.

Diffuse reflectance spectroscopy in the ultraviolet-visible range (UV-Vis DRS) was performed using an Agilent Cary 5000 UV-Vis- NIR spectrophotometer. The catalyst was finely ground and the absorbance was measured in the 200-800 nm range at ambient conditions. All spectra were obtained with hydrated samples and the reference compound was $BaSO_4$. The Kubelka-Munk function, $F(R_\infty)$, was obtained from the absorbance.

3.4.3 CATALYTIC TESTS

WGS reaction tests were performed in a fixed bed quartz reactor (i.d. 9 mm) operating at atmospheric pressure illustrated in Scheme 3.1. The catalyst (75 mg) was diluted in 125 mg of ground quartz and reduced *in situ* at 500 °C, 10 °C min^{-1} for 1 h in 35 mL min^{-1} of H_2. The catalyst was cooled to 250 °C and the WGS reaction was performed with 1:3 CO:H_2O (v/v) feed ratio and total (wet) flow of 115 mL min^{-1}, 4.3% v/v CO. The CO conversion (%) was followed by gas chromatography in an Agilent CG 7890 equipped with a TCD detector, at temperatures of 250, 300, 350, 400 and 450 °C, with 5 measurements (about 8 min each) at the different temperatures. The CO conversion was obtained by Equation 3.2:

$$\boldsymbol{CO\ conversion}\ (\%) = {\boldsymbol{mol\ CO_2} * \boldsymbol{100}}/{\boldsymbol{mol\ CO} + \boldsymbol{mol\ CO_2}} \qquad \text{Equation 3.2}$$

The specific reaction rate (r) was estimated by Equation 3.3:

$$\boldsymbol{r = F_{CO} * CO\ conversion}\ (\%) * \boldsymbol{MM/100 * m_{cat} * tm * D} \qquad \text{Equation 3.3}$$

Where F_{CO} = CO molar flow (mol s^{-1}); MM = Pt molecular mass (g mol^{-1}); mcat = catalyst mass (g); tm = metal loading (%) and D = metal dispersion (%, estimated by EXAFS data).

Scheme 3.1: Illustration of the catalytic unit for GSR reaction run. In parenthesis are the adaptations for WGS reaction.

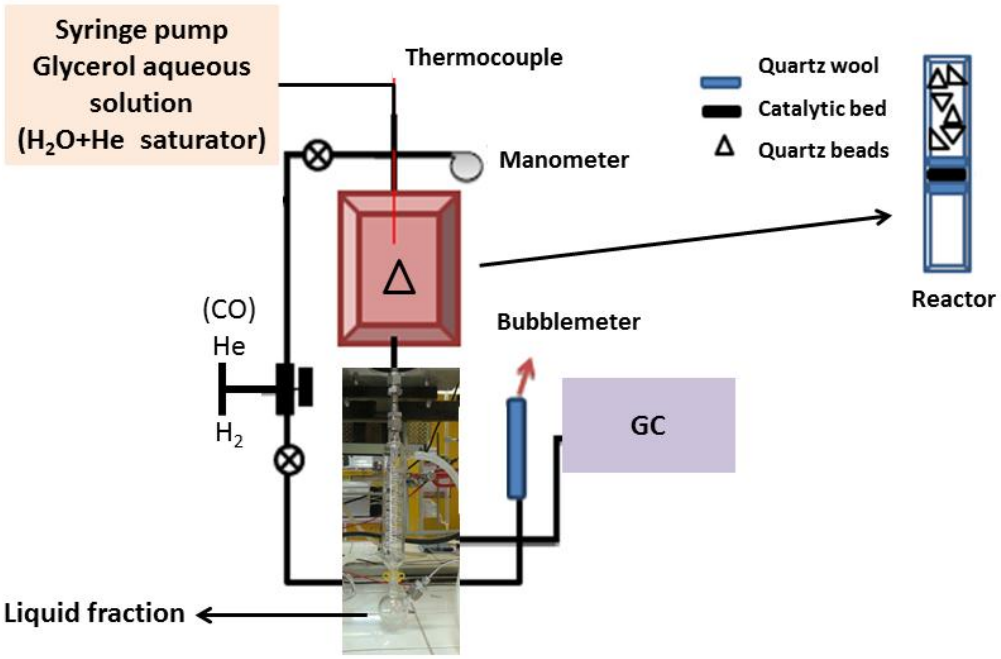

GSR reaction tests were performed in the catalytic unit depicted in Scheme 3.1. The catalyst (100 mg) was diluted in 400 mg of ground quartz and reduced *in situ* at 500 °C, 10 °C min^{-1} for 1 h in 35 mL min^{-1} of H_2. The reaction was performed at 400 °C for 2h. A glycerol aqueous solution (3.3 mol L^{-1}) was fed into the reactor by a Cole Parmer 74900 syringe pump (at a rate of 1.9 mL h^{-1}) and vaporized before reaching the catalyst bed, using He as carrier gas (30 mL min^{-1}). The total liquid fraction was collected in a condenser flask and the gaseous products H_2, CO, CO_2 and CH_4 were analyzed by an Agilent GC7890A gas chromatograph, using a TCD and He as carrier gas. Glycerol total conversion was obtained by detection of unreacted glycerol in the liquid fraction in an Agilent GC7890A using a Flame Ionization Detector (FID). The liquid components were identified by an Agilent GC7890A using a mass spectrometer detector quadrupole 5978C inert XL NSD Agilent.

3.5 RESULTS AND DISCUSSION

3.5.1 CHARACTERIZATION

The diffraction profiles of the catalysts and the bare γ-Al_2O_3 support are shown in Figure 3.1 The diffraction pattern of **PtAl** catalyst is similar to the γ-Al_2O_3 support and the absence of peaks corresponding to crystalline phases of Pt and/or PtO_2 indicates that the metallic phase is well dispersed over the alumina surface. For the **xVPtAl** catalysts, an increase in the diffracted intensity can be seen below 2θ ~30°. In fact, for the V_2O_5 standard, the three main peaks are found at 2θ equal to 20.28°, 26.15° and 31.01° and correspond to the (001), (110) and (031) reflections of the α-phase, respectively (PDF 041-146). Therefore, the observed slight increase in the intensity of the signal at this 2θ region for the **xVPtAl** catalysts suggests the absence of a highly ordered V_2O_5 phase. Table 3.1 shows the Pt and V wt % obtained by XRF. Considering these values and the specific surface area obtained for the PtAl catalyst (BET 300 m^2/g), it was possible to estimate the vanadium surface coverage (V atoms per nm^2) for each catalyst (Table 3.1). At these loadings, below 2 V nm^{-2}, the formation of V_2O_5 nanoparticles, not detected by XRD, was not indeed expected [130–133]. For example, Carrero *et al.* [134] found that V_2O_5 nanoparticles were formed when using ammonium metavanadate as precursor for coverages of 6.1 V nm^{-2} and greater, which is about three times higher than the maximum V loading of our samples. For other precursors the threshold was even higher (V loading necessary to form a monolayer over alumina is about 8 V nm^{-2}). Similar results were found by Wu *et al.* [131] that detected that crystalline V_2O_5 becomes the dominant species only at much higher coverage, i.e., 14.2 V nm^{-2}, although it started to be formed at coverages of 4.4 V nm^{-2}. The absence of crystalline V_2O_5 domains in our samples indicated by XRD were also confirmed by visible Raman spectroscopy that did not show the characteristic intense band around 994 cm^{-1} of the crystalline V_2O_5 phase [69,75,131,134] (not shown).

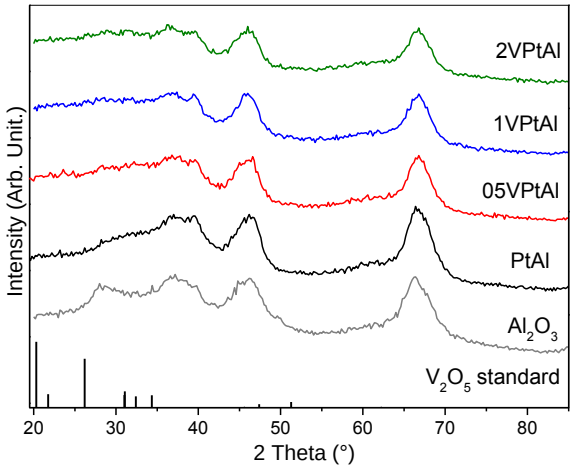

Figure 3.1: Diffraction profiles of xVPtAl catalyst and γ-Al_2O_3 support; V_2O_5 standard (PDF 041-146) is shown for comparison.

Table 3.1: Chemical composition obtained by XRF and V surface coverage (V atoms/ nm^2).

Sample	Pt (% wt.)	V (%wt.)	V (nm^{-2})
PtAl	0.55	-	-
05VPtAl	0.43	1.18	0.5
1VPtAl	0.44	2.51	1.0
2VPtAl	0.49	4.79	1.9

One of the interesting and challenging aspects of vanadium is that it presents a variety of oxidation states and oxide structures. When dealing with vanadium oxides dispersed on alumina, it has been shown that the main species depend on the V loading. At low loadings, these species can be monomeric, having V-O bonds with the support, and polymeric, with bridging V-O-V bonds, as depicted in Figure 3.2**.** It is also important to consider the existence of hydroxyl species due to hydrated conditions [132].

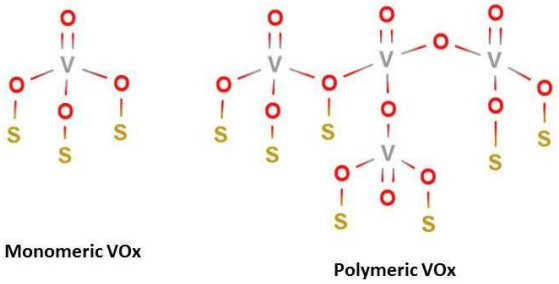

Figure 3.2: Illustration of V structures as a function of V loading over alumina surface. The S symbol stands for the alumina support.

Nevertheless, the loading range that dictates the prevalence of one or another structure and which one would render the support a higher reducibility depend on several factors, such as the vanadium precursor [134] and the oxide support. For instance, according to Nguyen-Thanh *et al.* [75] the predominant species over ZrO_2 at low V loadings (up to 2.8 V nm^{-2}) are monomeric VO_x (having at least one V-O-Zr bond with the support). At higher loadings, the amount of these isolated species increases to the limit in which the formation of polymeric VO_x and a monolayer are favored; which possess more V-O-V bridging bonds, therefore interacting less with the support. The authors then correlated the high concentration of monomeric-units to the increase in the support reducibility, which in turn was attributed as the main factor to the enhanced catalytic activity observed for WGS reaction in Pt-VO_x/ZrO_2 catalysts. In contrast, Wu *et al.* [130,131] investigated the surface of Al_2O_3 after impregnation with vanadium and suggested that the presence of dispersed polymeric units rendered facilitated reducibility in comparison with the monomeric ones. This observation was in agreement with the work by Ballarini *et al.* [133] in samples containing about 2 % wt of V_2O_5 impregnated over γ-Al_2O_3 (0.7 V nm^{-2}), which reported the reduction of isolated VO_x species at higher temperatures. Samples with higher V loadings (7 and 10 % wt) presented

predominance of polymeric species and bulk vanadium oxide that reduced at lower temperatures.

To compare the samples concerning the geometric and electronic structure of vanadium over **xVPtAl** catalysts, XANES spectra of the fresh samples (as-prepared) were collected at V K- and Pt L_3-edges and are shown in Figure 3.3a and b, respectively.

Figure 3.3a shows that at room temperature all **xVPtAl** catalysts, in average, are composed by similar species in respect to their electronic and geometric nature. It is also evident that the dominant species are not similar to bulk V_2O_5, although the presence of the pronounced pre-edge peak around 5470 eV is consistent with a similar local environmental, with V^{5+} species in a non-centrosymmetric coordination with oxygen atoms [127]**.** The XANES data is in accordance to the works by Tanaka *et al.* [135] and Ruitenbeek *et al.* [136], who identified V species impregnated over alumina as VO_4 units having V^{5+} ions in distorted tetrahedral coordination, as illustrated in Figure 3.2**.** These results are also in agreement with the absence of V_2O_5 crystalline phase on the surface of the catalysts. In the case of Pt, the XANES spectra for all catalyst (Figure 3.3b) indicate the presence of oxidized Pt species; however, the spectra do not match the PtO_2 standard indicating the formation of a highly dispersed PtO_x phase.

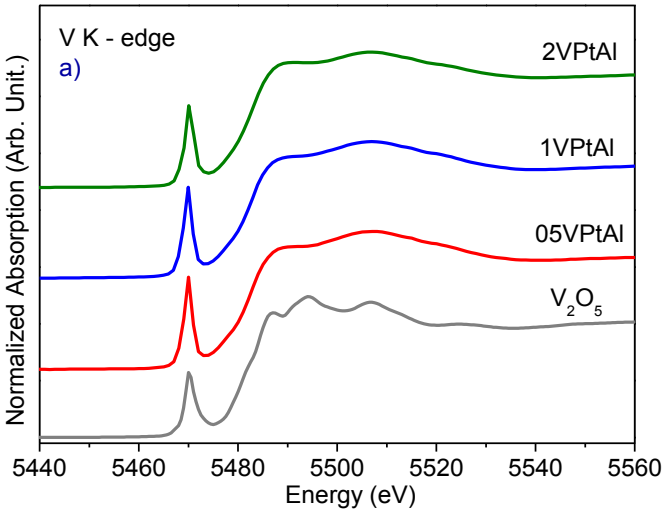

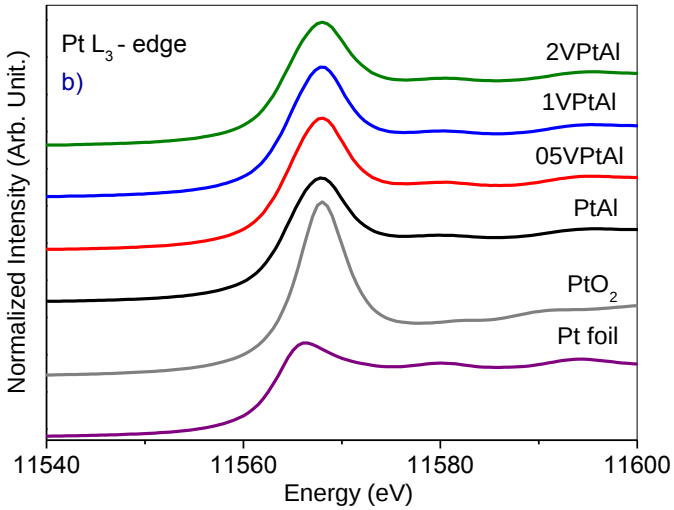

Figure 3.3: XANES spectra of the fresh samples at a) V K-edge and b) Pt L_3-edge. Bulk V_2O_5, Pt^0 and PtO_2 are shown as references.

To gain more insights about the evolution of VO_x species as a function of V loading, the samples were analyzed by UV-Vis DRS and the profiles are shown in Figure 3.4. It is worth to point out that the **1VPtAl** and **2VPtAl** samples may have sufficient V to present polymeric VO_x species, following the work of Nguyen-Thanh *et al.* [75] and Ballarini *et al.* [133].

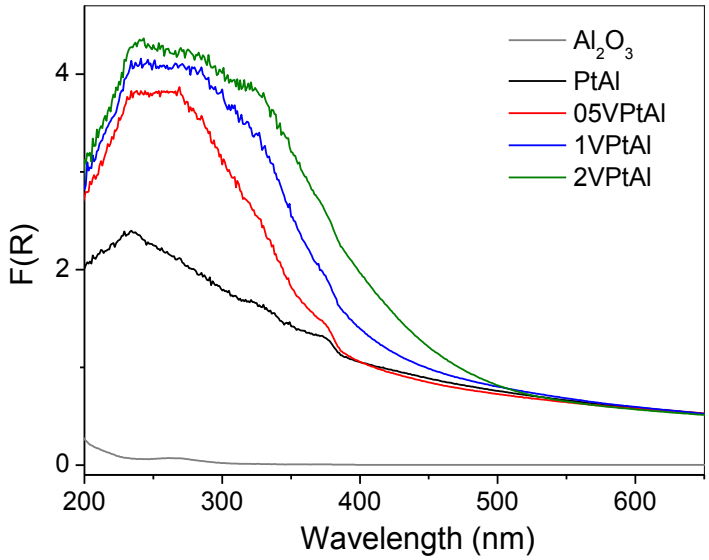

Figure 3.4: UV-VIS DRS spectra of the fresh samples.

According to several authors [131,137,138], the absorption bands of the UV-Vis DRS spectra around 240 nm can be assigned to monomeric species of vanadium, while the bands at higher wavelengths (near 300-400 nm) would be related to polymeric VO_x. Crystalline V_2O_5 would present a broad absorption extending to longer wavelengths (> 450 nm). A more quantitative analysis based on the linear relationship between the energy edge determined by UV-Vis DRS and the number of V-O-V bonds found in polymeric species was proposed

[139]. In our xVPtAl catalysts, the absorption bands are broad and due to the presence of Pt a quantitative evaluation is difficult. Nevertheless, it seems a consensus that the bands at longer wavelengths can be attributed to polymeric entities (once V_2O_5 NPs are excluded) and as a consequence, Figure 3.4 indicates that the amount of polymeric species seems to increase as a function of the loading (especially by observing the shift to higher wavelengths from 05VPtAl to 2VPtAl and the raise in the bands around 330 and 400 nm). These results are in accordance with previous works on bare alumina up to the monolayer coverage [131,139,140].

So far, the fresh catalysts were characterized and they are composed of dispersed PtOx and monomeric and polymeric VO_x species over the surface, with the latter probably increasing with V loading. Nevertheless, prior the reaction the catalysts were activated under H_2 up to 500 °C for 1 h and Figure 3.5 shows the modification of the catalyst during TPR-H_2. The reduction profiles provide information about the reducibility of species as well as indirect information about the interaction between the components of the catalysts (V-Pt).

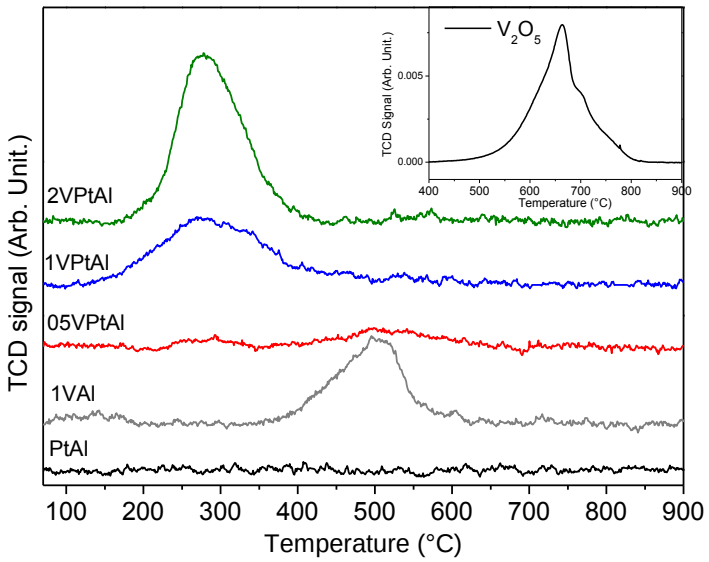

Figure 3.5: TPR-H_2 profiles of xVPtAl samples. The inset shows the TPR-H_2 profile of bulk V_2O_5.

Due to the small Pt loading (0.5% wt), the H_2 consumption corresponding to PtO_x reduction could not be detected in the **PtAl** catalyst, in agreement with the work by Garcia et *al.* [137]. On the other hand, clear H_2 consumption is observed for **1VPtAl** and **2VPtAl** catalysts and the **1VAl** support (prepared in a similar way to **1VPtAl** but without Pt), indicating that the reduction of the VO_x species could be detected. The inset in Figure 3.5 shows the reduction profile of bulk V_2O_5, which exhibits a broad peak centered at about 670 °C [131]. No H_2 consumption at higher temperatures was found for all catalysts, which further corroborates

the absence of a crystalline V_2O_5 phase. Comparing to the **1VAl** support, the H_2 consumption peak shifts the center to about 500 °C, indicating that VO_x species dispersed on the alumina surface are reduced more easily than bulk V_2O_5, in accordance with the literature [131,133,140]. Comparing the **1VAl** support and **1VPtAl** catalyst, it is clear that the presence of Pt shifts further the reduction towards lower temperatures (around 300 °C). This effect has been associated to H_2 spillover promoted by Pt over VO_x species [137,141], suggesting some degree of Pt-V interaction. By comparing **1VPtAl** with **05VPtAl** and **2VPtAl** catalysts, the H_2 consumption is in line with the V loading increase. The similar reduction profiles of **1VPtAl** and **2VPtAl** suggest the predominance of similar VO_x species, in agreement with the DRS UV-Vis and V K-edge XANES data. Therefore, the TPR-H_2 profiles indicate that the interaction with alumina and the presence of Pt facilitates the reducibility of the VO_x species independently of the vanadium content, as also observed by Zheng *et al.* [142]. This property has been pointed out as an important factor in catalytic processes such as propane total oxidation [137] and WGS reaction [40]. The support reducibility can induce the formation of active OH species and/or promote their mobility over the catalyst surface [75], which are important steps in the WGS and steam reforming mechanisms [6,40].

As an attempt to clarify the catalysts changes during the reduction process, *in situ* XANES experiments at Pt L_3- and V K-edges were performed. In the case of Pt, the results show the evolution of PtO_x species to metallic Pt, as evidenced in Figure 3.6. The analysis of the EXAFS data are shown in Table 3.2 and indicates that **xVPtAl** samples undergo a decrease in Pt dispersion compared to **PtAl**, which was possibly caused by the additional calcination performed after vanadium impregnation.

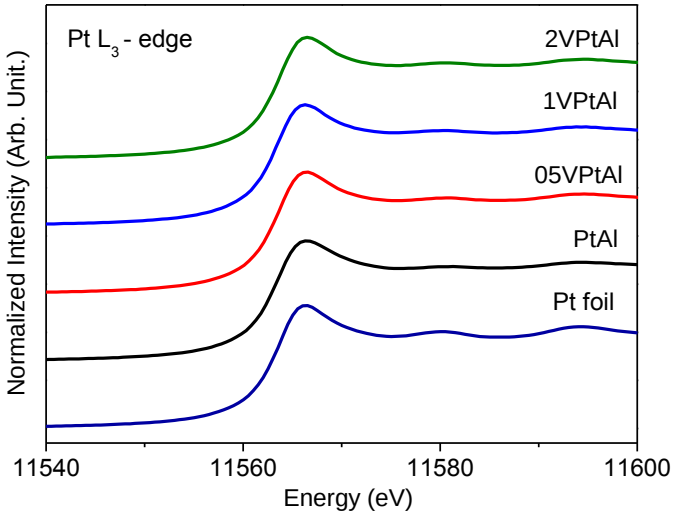

Figure 3.6: *In situ* XANES spectra at Pt L_3-edge of the catalysts after TPR-H_2. The Pt standard is shown for comparison.

Table 3.2: Structural parameters obtained from the EXAFS analysis at Pt L_3-edge of catalysts after the reduction, at room temperature.

Sample	N_{Pt-Pt}	R_{Pt-Pt} (Å)	σ^2_{Pt-Pt} (Å^2)	Pt Dispersion (%)
PtAl	8.5	2.75	0.007	79.9
05VPtAl	9.8	2.75	0.007	48.5
1VPtAl	9.7	2.75	0.008	50.6
2VPtAl	9.9	2.75	0.007	47.3

In the case of V K-edge, the analysis is more complex. Wong *et al.* [127] analyzed the main oxide phases and several other compounds with known structure and coordination. Among the most important vanadium oxide structures are V_2O_5, V_2O_4, V_4O_7, V_2O_3 and VO; their V oxidation states varies from +5 to +2 and their coordination evolves from distorted square pyramid (V_2O_5) to distorted octahedral and finally to regular octahedral (VO). For a better comparison of the samples, the authors took the zero of energy with respect to the first maxima of the first derivative of V reference foil spectra (at 5465.0 eV) and the position of all peaks was then given respective to this energy. To support the analysis of the catalysts, we first performed the *in situ* reduction of bulk V_2O_5 and followed the changes of V K-edge spectra. In this way, the position of the features of the selected spectra measured here was compared to the data published by Wong *et al.* [127] and the intermediate vanadium oxides formed on the catalysts during reduction was assigned. Figure 3.7a presents the results for bulk V_2O_5 under TPR-H_2. The intense pre-edge peak at 5.0 eV in V_2O_5 spectra (spectrum taken at room temperature) is characteristic of a non-symmetric local coordination, as in the distorted square pyramid, and correspond to the dipole-forbidden 1s→3d transition that becomes partially allowed due to the mixing of 3d-4p metal orbitals and overlap from V 3d orbitals with O 2p [127]. When the structure evolves from V_2O_5 to VO (regular octahedral) the symmetry increases and therefore the pre-edge peak decreases. The decrease in the V oxidation state from +5 to +2 also shifts the absorption edge to lower energies. Therefore, by heating under H_2 the V K-edge XANES spectra evolves (Figure 3.7a), with a progressive decrease in the pre-edge peak intensity and energy and a rise of the white line intensity. The corresponding assignments of the intermediate vanadium oxides are shown in Figure 7b. Accordingly, at 512 °C the structure of V_2O_4 is formed, with V^{4+} in distorted octahedral coordination. At 602 °C the V_4O_7 phase can be identified, with V^{3+} and V^{4+} ions in distorted octahedral coordination. Finally, at 650 °C the spectra is similar to the one attributed to V_2O_3. Comparing to conventional TPR-H_2 (inset, Figure 3.5) for bulk V_2O_5, the H_2 consumption up to 650 °C can be associated to the reduction of V_2O_5 to V_2O_3, which is probably reduced further to VO up to 800 °C.

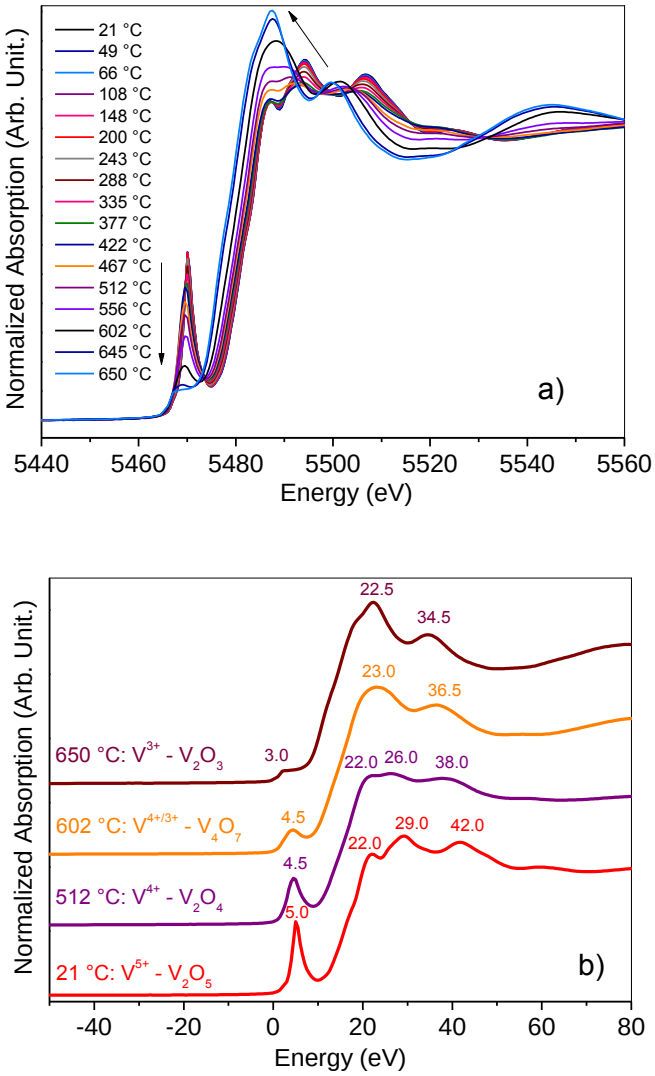

Figure 3.7: a) *In situ* XANES at V K-edge spectra for bulk V_2O_5 during TPR-H_2; b) identification of V oxide phases formed during TPR-H_2 and the corresponding temperatures.

After the successful assignment of the intermediary vanadium oxides formed during bulk V_2O_5 reduction, **xVPtAl** catalysts were also investigated by *in situ* XANES at V K-edge. The corresponding spectra obtained at selected temperatures are shown in Figure 3.8**.**

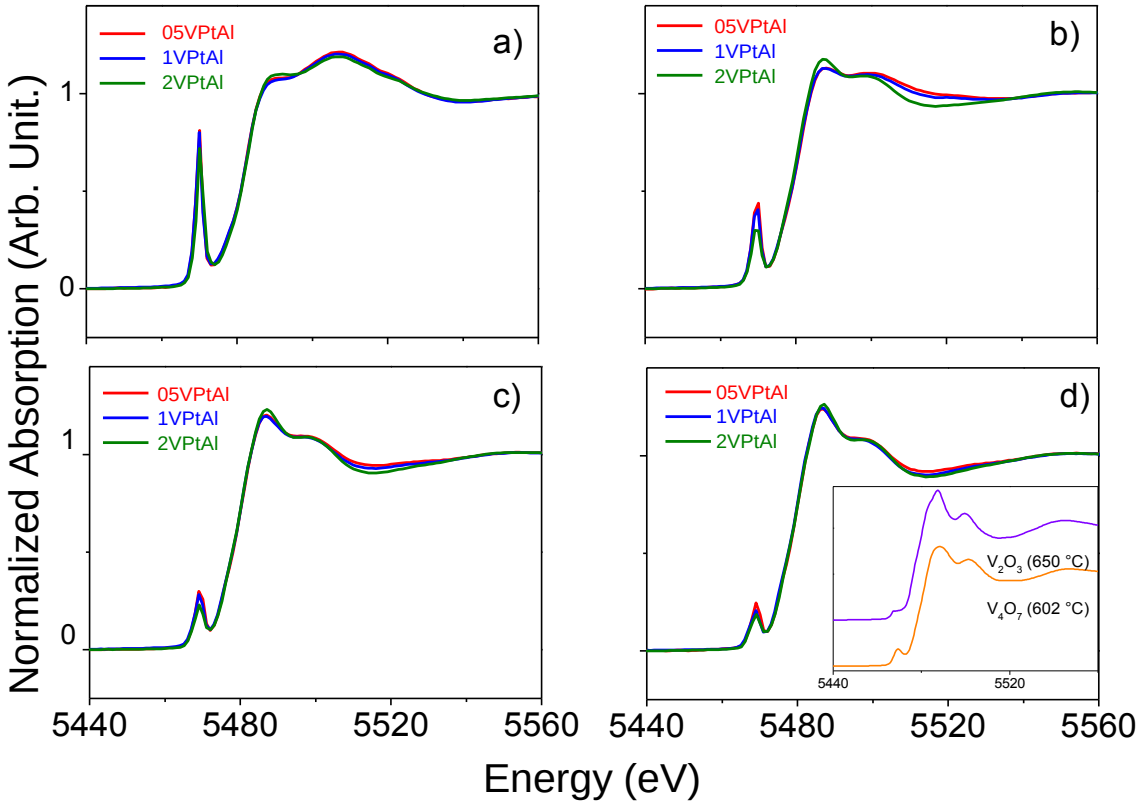

Figure 3.8: Selected XANES spectra of **xVPtAl** catalysts obtained at V K-edge during TPR-H_2 a) room temperature, b) 300 °C, c) 400 °C and d) 500 °C. The inset in (d) shows the spectra corresponding to the V_4O_7 and V_2O_3 phases (see Figure 3.7b) for comparison.

Comparing the samples under reduction, above 400 °C all three catalyst have similar profiles that did not change at 500 °C. The main reduction of vanadium species up to 400 °C was in accordance with conventional TPR-H_2 results (Figure 3.5), which showed no H_2 consumption above this temperature for **xVPtAl** samples. The similarities of the spectra at 500 ^{o}C for the three catalysts and V_4O_7 and V_2O_3 bulk phases suggest the presence of V^{3+} and V^{4+} ions coordinated in a more centrosymmetric configuration, consistent with distorted VO_6 species. The small discrepancies with the bulk phases are likely originated by the dispersed nature of the species in the catalysts [127,136]. The presence of mixed valence (V^{3+} and V^{4+}) species after reduction in H_2 was also found by Wu *et al.* [130] on VO_x/Al_2O_3 samples. Therefore the results suggest that all three **xVPtAl** samples after reduction, including **05VPtAl**, present mixed valence (V^{3+} and V^{4+}) VO_x species on the surface that would be the species available for the reaction after catalysts activation.

3.5.2 WGS REACTION

Figure 3.9 shows the performance of the catalysts for the WGS reaction and became evident that the presence of VO_x species significantly increases the CO conversion

in comparison with **PtAl** catalyst, especially above 300 °C. Table 3.3 shows the specific rate obtained at 250 and 300 °C. Interestingly, a clear correlation with V loading was not found.

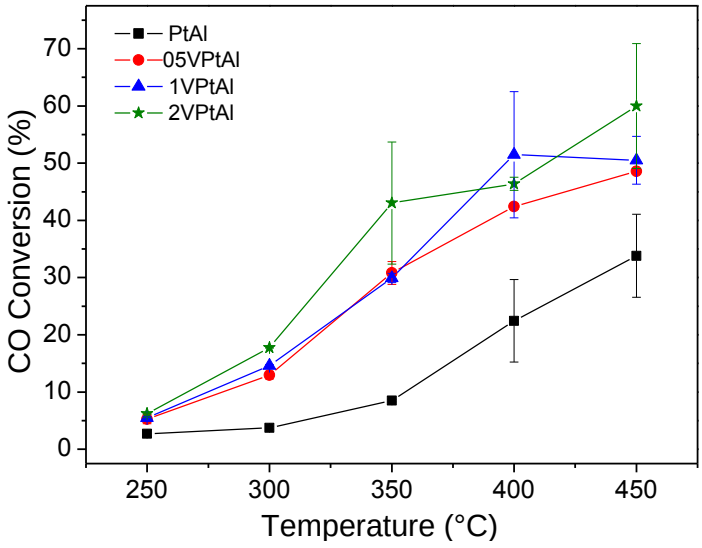

Table 3.3: Specific rate calculated at 250 and 300 °C.

	Specific rate, r (s^{-1})	
Sample	**250 °C**	**300 °C**
PtAl	0.001	0.002
05VPtAl	0.005	0.011
1VPtAl	0.005	0.012
2VPtAl	0.006	0.015

Figure 3.9: CO conversion (%) for VPtAl catalysts as a function of temperature.

The fivefold increase in the specific rate at both temperatures for **xVPtAl** catalysts compared to **PtAl** evidences the promoting effect of vanadium; however, the results suggests that the enhancement was not significantly affected by the V loading. Based on the previous results, the nature of VO_x species over the surface of the catalysts may be very similar in spite of the increased V content.

To understand the nature of V and Pt species under WGS reaction conditions, *in situ* XANES at V-K and Pt-L_3 edges were measured. The results for **1VPtAl** catalysts are shown in Figure 3.10**;** the other ones (not shown) have similar profiles. The behavior of Pt and V species were not altered under WGS conditions, while Pt was in metallic form as after the reduction step, the vanadium remained in mixed V^{3+}/V^{4+} oxidation state in a distorted octahedral coordination.

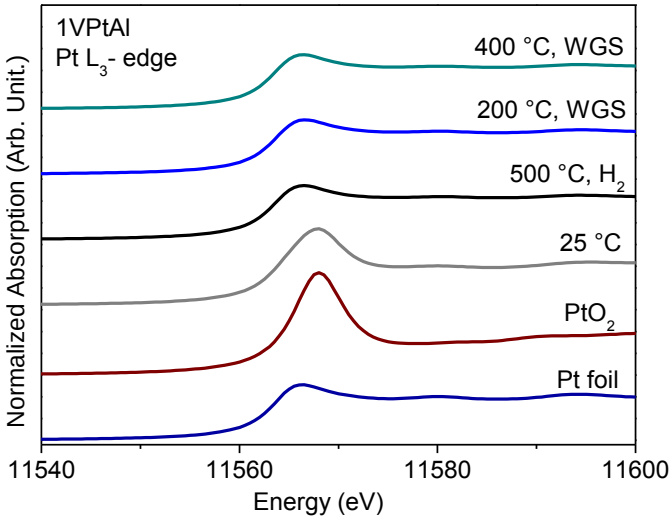

a)

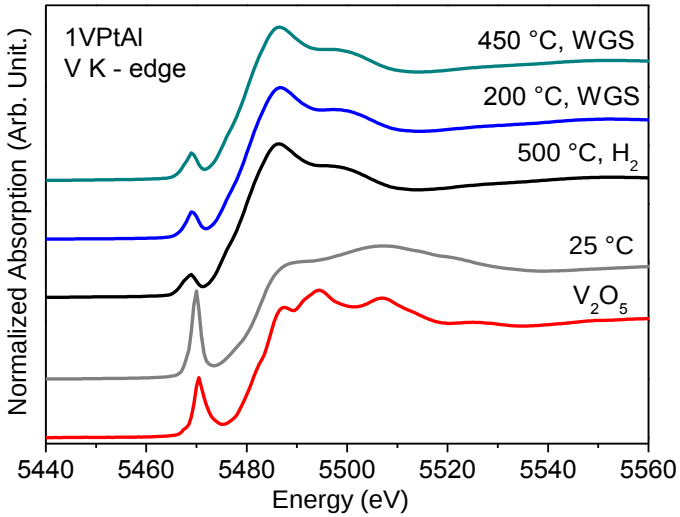

b)

Figure 3.10: *In situ* XANES of 1VPtAl at (a) Pt L_3-edge and (b) of V K-edge. Spectra corresponding to fresh catalyst (at 25 °C); after activation and under H_2 at 500 °C; under WGS reaction at 200 °C and 450 °C. Pt^0, PtO_2 and V_2O_5 references are shown for comparison.

The increase in the CO conversion of the **xVPtAl** samples when compared to the unpromoted **PtAl** catalyst can be thought considering the important role of the support in the WGS reaction mechanism. The addition of other oxides in Pt-based catalysts can modify the catalytic activity in several ways, such as by improving the dispersion and stabilization of the metal phase over the surface of the support, changing the reducibility of the support, altering the electronic state of metal phase, by creation of new active sites at the metal-support interface, among others [41,69,143]. Accordingly, the results presented in this work indicate that the enhanced catalytic activity observed for V promoted catalysts may be associated to the increase in the reducibility of the support and/or the creation of more active interface sites.

The presence of polymeric VO_x could lead to the formation of a higher amount of OH species on the catalyst surface, compared to **PtAl**, and these species would react to produce the intermediates as formate [141]. It has been proposed that the polymeric moieties could also increase the mobility of these OH species through the support, favoring the reaction [75]. It is interesting to note, however, that the lack of correlation with V content, suggests that the further addition of V in **1VPtAl** and **2VPtAl** creates additional VO_x species that do not significantly participate in the reaction. This behavior is different from the one found for model Pt/Al_2O_3 catalysts promoted with cerium, where a correlation with CeO_2 loading was found [41] suggesting that an increase in the promoter content increases the probability of forming metal-oxide interfacial sites. In the case of vanadium, however, the interaction with alumina and the tendency to form polymeric species spread on its surface [144] might frustrate the odds to form new Pt-VO_x interfacial sites with increasing loading. It is interesting to note that in the **2VPtAl** there are 30 times more V atoms than Pt ones. The importance of interfacial sites has been demonstrated in other systems. For example, Sener *et al.* [63], applying controlled surface reactions to produce Pt/Mo bimetallic catalysts, reported that the turnover frequency for WGS reaction exhibited a linear correlation with the amount of MoOx species in close contact with Pt metallic sites. The authors then suggested that the interfacial Pt-Mo sites would be the active ones for the reaction, and the MoOx promoter would have the role to stabilize water and/or OH groups, thus increasing their coverages, facilitating the reaction. DFT has also helped to highlight the important role played by the Pt-metal oxide interfacial sites, revealing a complex framework depending on the system [57]. In this sense, for the **xVPtAl** catalysts the interfacial Pt-VO_x sites may be the responsible for the 5-fold enhancement of the activity for WGS reaction compared to the **PtAl** catalyst.

3.5.3 GSR REACTION

Considering the positive impact of vanadium in the WGS reaction, the **VO_x-Pt/Al_2O_3** catalysts were tested for the GSR reaction and it was expected a maximization of H_2 production through the WGS step. Figure 3.11 shows the gaseous products distribution (CO_2, H_2, CH_4 and CO) obtained under GSR reaction.

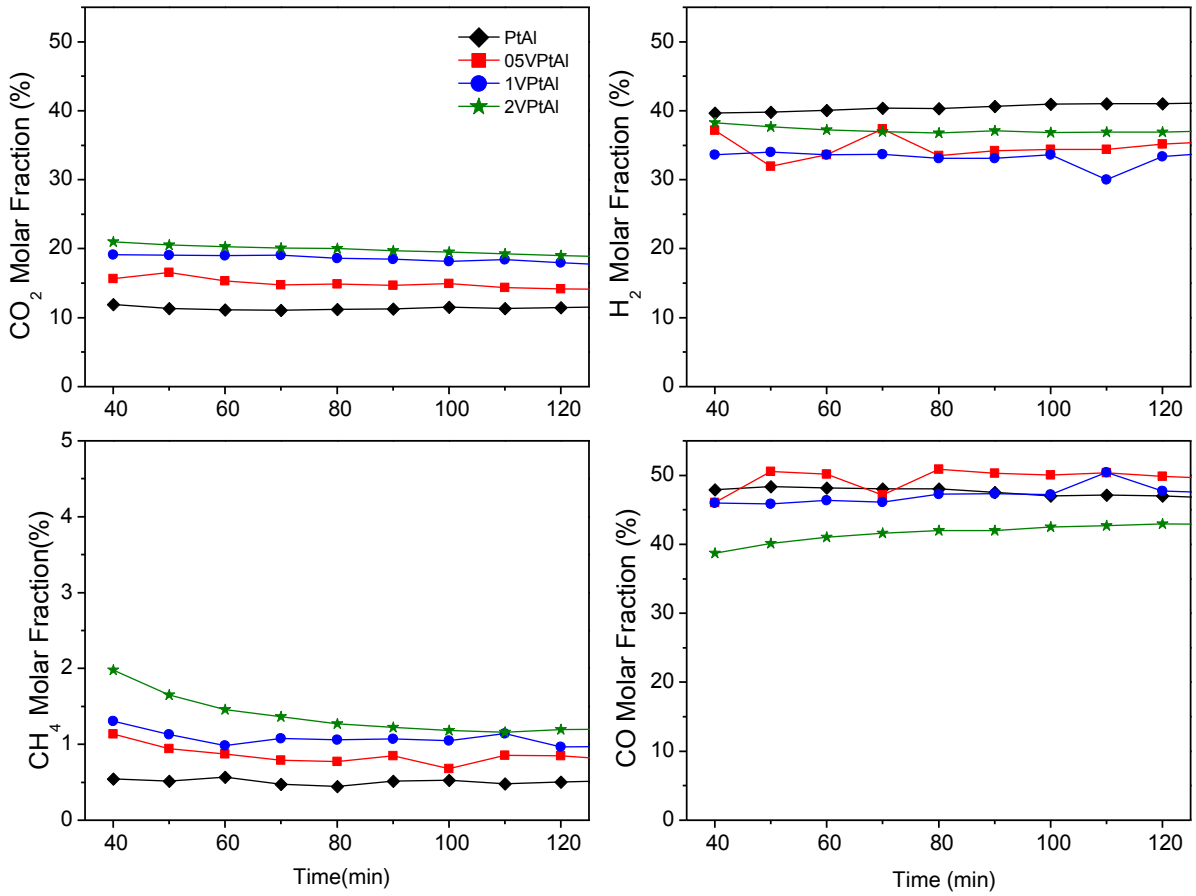

Figure 3.11: Distribution of gaseous products CO_2, H_2, CH_4 and CO as a function of time on stream during GSR reaction at 400 °C for **xVPtAl** samples.

The results showed that for all samples the major gaseous products were CO and H_2, followed by CO_2 and a small fraction of CH_4. The product distribution was consistent with glycerol decomposition reaction (Eq. 2); however, the presence of CO_2 indicated that WGS reaction (Eq. 3) was also occurring. The CO_2 fraction was higher for the **xVPtAl** catalysts and increased with the V loading, in agreement with the presence of VO_x species favoring the WGS reaction. However, an opposite behavior for H_2 was found; the **xVPtAl** catalysts showed lower H_2 fraction compared to **PtAl** and there was a slight decrease in H_2 production for higher vanadium loading. This suggests that the H_2 produced by WGS reaction may have been consumed by parallel reactions. According to Pompeo *et al.* [23], Pt-Al_2O_3 catalysts in GSR reaction favor the dehydration pathway of glycerol molecule, due to the acid nature of alumina, forming CH_4 and CO_2, by the following overall reaction:

$$\boldsymbol{C_3H_8O_3 \rightarrow CO_2 + CO + CH_4 + 2H_2} \qquad \text{(Equation 3.4)}$$

The authors reported that this reaction would proceed alongside the decomposition reaction (Equation 1.2), leading to the additional formation of CO and H_2. Taking this reaction into account and the formation of the small amount of CH_4, it is

suggested that this step may occur as a minor route. Moreover, the higher fraction of CH_4 and the reduced amount of H_2 for **xVPtAl** and vanadium content suggest that parallel reactions are enhanced by the vanadium presence.

The total liquid fraction of the products, collected at the end of the reactions, indicated no residual glycerol within the range of the calibration curve (up to 95%), showing that the reaction conditions led to total conversion of glycerol. The major products detected in the liquid fraction for all catalysts were ethanol, 2-propenal (acroleyn), 1-hydroxy-2-propanone, propanal and phenol, which strongly evidences the presence of glycerol dehydration reactions in acid sites of the support (Al_2O_3 and VO_x/Al_2O_3) [23,103]. In fact, it has been reported the increase in support acidity with the addition of VO_x species over Al_2O_3 within monolayer coverage regime [140]. Furthermore, the lower selectivity for H_2 observed for **xVPtAl** catalysts are consistent with the reported activity of vanadium catalysts for the dehydration reactions of acetaldehyde and glycerol [132,145], that would be promoted by the acid sites of VO_x, therefore leading to the formation of the aforementioned byproducts.

In summary, although the V promoted catalysts exhibited higher CO conversions in WGS reaction when compared to **PtAl** sample, under GSR the presence of vanadium seems to favor the formation of byproducts, decreasing the fraction of H_2, likely due to the acidic nature of VO_x species.

3.6 CONCLUSIONS

Vanadium oxides are interesting and challenging structures to apply in catalysis and their addition on Pt/Al_2O_3 catalysts illustrated the powerful tuning of the catalysts properties, as observed by their performance on WGS reaction. The promoted samples showed a five-fold increase in the WGS activity when compared to **PtAl**, therefore demonstrating the success of this approach. However, the increase of V content did not clearly impact in the WGS activity, which might be related to the formation of polymeric VO_x species interacting with alumina surface instead of new interfacial Pt-VO_x sites that would favor the reaction. The *in situ* characterization of the catalysts showed that metallic Pt and V^{3+}/V^{4+} species are present during WGS reaction regardless of V loading. When applied to GSR reaction, the presence of VO_x species favored the WGS step; however, the H_2 fraction did not increased as expected, probably due to its consumption in parallel reactions and/or due to the acidic nature of VO_x species over the surface that would lead to the formation of byproducts. Therefore, the overall result for both reactions reinforces necessity of finding the right tuning of several aspects to optimize the catalyst activity and selectivity. In this sense, a new set of catalysts was designed to simultaneously present higher activity and selectivity for both reactions and allow the study of crucial parameters dictating the catalytic performance.

Chapter 4

Pt/CeO_2/SiO_2 SYSTEM

4.1 OVERVIEW

In light of the findings about the activity of VO_x-Pt/Al_2O_3 catalysts towards GSR reaction, it was clear a new set of catalytic materials needed to be developed to optimize the properties of the support and metal oxide promoter to decrease the formation of byproducts and enhance the selectivity for H_2 production. Moreover, the preparation of materials focusing on synthesis methods that allow the tuning of metallic sites may help the understanding of how GSR reaction proceeds and what can be done to improve catalysts performance. It this sense, Pt/CeO_2/SiO_2 materials were developed applying different approaches so it was possible to evaluate key properties relevant to glycerol conversion and H_2 selectivity.

This chapter starts with the synthesis of Pt/CeO_2/SiO_2 catalysts, which comprises a set of catalysts having the Pt metallic phase obtained by distinct methods and another set having samples differing in the preparation of CeO_2 phase. The characterization section compares the main properties of the catalysts, followed by a section concerning the WGS activity evaluation, including in situ experiments performed by ME-DRIFTS for selected samples. After, the catalytic results for GSR reaction for Pt/CeO_2/SiO_2 systems are discussed, and the final remarks regarding this chapter is presented in the last section.

4.2 MATERIALS AND METHODS

4.2.1 CATALYST PREPARATION

4.2.1.1 SYNTHESIS OF CeO_2 NPs (5 and 9 nm)

CeO_2 NPs with mean size of 5 nm were synthesized as described by Lee *et al.*[146]. The precursor $Ce(NO_3)_3.6H_2O$ (1 mmol) was added to a round-bottom flask containing 5.0 mL of 1-octadecene under stirring. Oleylamine (3 mmol) was added and the system was purged with vacuum and N_2 for 3 times and left under stirring in N_2 atmosphere. The mixture was heated following the protocol: 80 °C, 10 °C min^{-1}, soak time of 30 min; 260 °C, 10 °C min^{-1} and soak time of 2 h. The mixture was quickly cooled (with a stream of compressed air outside the flask) up to 60 °C, precipitated with a 1:1 (v/v) acetone:methanol (25 mL) solution and centrifuged at 4500 rpm for 30 min to remove the excess of ligands and 1-octadecene. The precipitation/washing was repeated for 5 times. Finally the NPs were redispersed in

hexane. Scheme 4.1 shows an illustration of the synthesis procedure for 5 and 9 nm CeO_2 NPs.

The synthesis of CeO_2 NPs of 9 nm was also performed following the work of Lee *et al.*[146]. Briefly, in a round-bottom flask containing 12.7 mL of 1-octadecene, the precursor $Ce(NO_3)_3.6H_2O$ (10 mmol) was added, followed by oleylamine (30 mmol), under stirring and N_2 flow. Subsequently, distilled water was added (4 mmol) and the mixture was heated at 80 °C, 10 °C min^{-1} and 30 min soak time. The temperature was raised to 260 °C, 10 °C min^{-1} and held for 2 h. The mixture was quickly cooled, and then the NPs were precipitated, washed and stocked in hexane.

Scheme 4.1: Synthesis of Colloidal CeO_2 NPs.

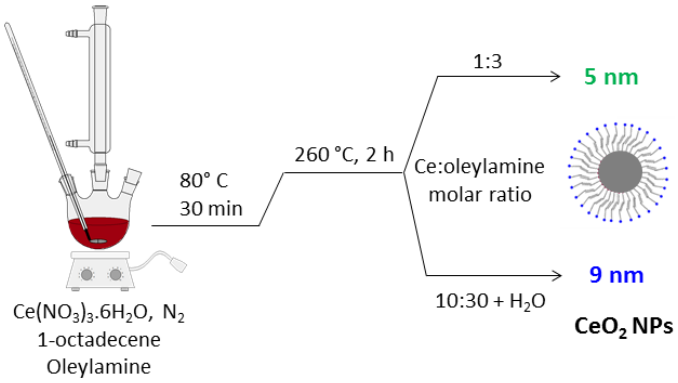

4.2.1.2 SYNTHESIS OF CeO_2/SiO_2 SUPPORTS

The synthesis of CeO_2/SiO_2 supports containing 5 and 9 nm CeO_2 NPs was performed by the impregnation of silica with colloidal ceria NPs with nominal loading of 12 % (w/w). For that, 0.5 g of silica was suspended in 30 mL of toluene under stirring for each size of CeO_2 NPs. The corresponding volume of the initial dispersion of CeO_2 NPs were diluted in 20 mL of toluene and added to the silica suspension. The mixture was kept under stirring for 19 h, centrifuged at 4500 rpm for 10 min and the solvent was removed in a rotating evaporator. The solid was dried overnight in an oven at 70 °C, calcined at 450 °C, 5°C min^{-1}, for 1 h under flow of synthetic air (80 mL min^{-1}). The samples were labeled **CeO2_5** (silica with 5 nm CeO_2 NPs) and **CeO2_9** (silica with 9 nm CeO_2 NPs) and their preparation is illustrated in Scheme 4.2.

Scheme 4.2: Preparation of CeO_2 supports with 5 and 9 nm CeO_2 NPs.

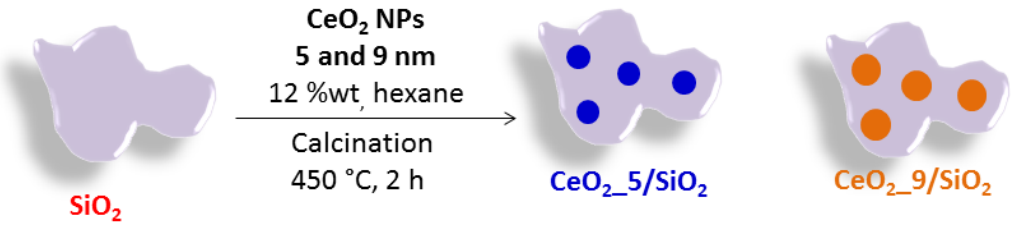

A second set of CeO_2/SiO_2 supports with varying CeO_2 loadings was prepared by impregnation and decomposition of a Ce^{3+} precursor salt, aiming nominal loadings of 6, 12 and 20% w/w of CeO_2 on silica. For each support, 1.0 g of silica was suspended in 65 mL of ethanol under stirring, while the corresponding weight of $Ce(NO_3)_3.6H_2O$ was dissolved in 30 mL of ethanol. The Ce^{3+} solution was then added to the silica suspension and the mixture was kept under stirring for 1h. The solvent was removed in a rotating evaporator and the solids were dried overnight in an oven at 70 °C. The powders were calcined at 450 °C, 5 °C min^{-1} for 1h under flow of synthetic air (80 mL min^{-1}). The resulting supports were then used for the preparation of NP_Pt catalysts (described on Item 4.2.1.5). They were labeled **i6CeO2**, **i12CeO2** and **i20CeO2**, where the prefix "i" stands for the method of CeO_2 preparation (impregnation of Ce precursor) and the number refers to the nominal CeO_2 loading (6, 12 or 20% w/w).

4.2.1.3 PREPARATION OF iPt CATALYSTS BY $Pt(acac)_2$ IMPREGNATION

A set of samples was prepared by wet impregnation of Pt precursor salt over two supports (bare silica and **CeO2_5**) followed by calcination. Silica Aerosil® 380 from Evonik was used for being commercially available and having high surface area (350-410 m^2 g^{-1}, as reported by the manufacturer), without any pre-treatment.

The Pt impregnation was performed on the two supports to result in 2% (w/w) of Pt. The precursor platinum acetylacetonate (II), $Pt(acac)_2$ (0.05 mmol), was dissolved in 4 mL of acetone, while 0.49 g of the support was dispersed in 25 mL of acetone in another flask, both kept under stirring for 30 min. The Pt solution was added to the support and the mixture was kept under stirring overnight. The solvent was removed in a rotating evaporator and the resulting solids were dried in an oven at 60 °C for 2 h and calcined at 400 °C, 10 °C min^{-1} for 4 h. The final catalysts were denominated **iPt/SiO_2** and **iPt/CeO2_5**. The prefix "i" indicates the method used for Pt addition.

4.2.1.4 SYNTHESIS OF COLLOIDAL Pt NANOPARTICLES

Colloidal Pt NPs were obtained according to the procedure described in literature [147], as depicted in Scheme 4.3. The precursor $Pt(acac)_2$ (0.2 mmol) was added under stirring

to a round-bottom flask containing trioctylamine (22.9 mmol) and then oleylamine (2.0 mmol) and oleic acid (8.0 mmol) were added. The mixture was kept under vacuum at room temperature for 5 min. Trioctylphosphine (0.1 mmol) was injected and the mixture was heated to 120 °C, 15°C min^{-1}, for 30 min. The atmosphere was changed to N_2 and the flask was quickly heated to 250 °C (40 °C min^{-1}) and held for 30 min. After cooling to room temperature, the NPs were precipitated with a mixture of 15 mL of isopropanol and 20 mL of methanol and centrifuged at 6500 rpm for 3 min, the procedure repeated twice. The NPs were collected and dispersed in hexane.

Scheme 4.3: Synthesis of colloidal Pt NPs.

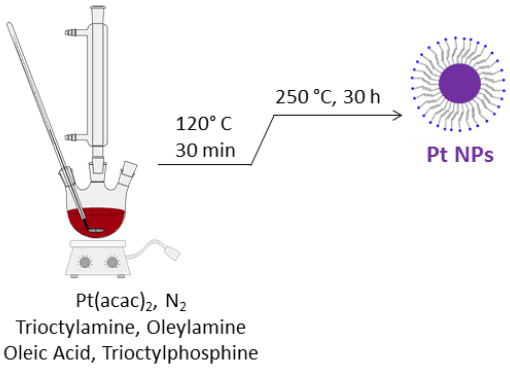

4.2.1.5 PREPARATION OF NP_Pt CATALYSTS BY Pt NPs DEPOSITION

In this group of samples the Pt metallic phase was added by the deposition of the previously synthetized colloidal Pt NPs (item 4.2.1.4) over the supports (bare silica, **CeO2_5** and **CeO2_9**). For the deposition of the colloidal Pt NPs, the procedure is the same as the deposition of CeO_2 NPs, aiming for a Pt loading of 2% w/w and was performed simultaneously for the three supports (bare silica, **CeO2_5** and **CeO2_9**), followed by the same calcination step to remove organic ligands. The resulting samples were named **NP_Pt/SiO2**, **NP_Pt/CeO2_5** and **NP_Pt/CeO2_9**, and generally denominated as NP_Pt catalysts.

The deposition of Pt NPs on the supports with CeO_2 at varied loadings obtained by impregnation (**i6CeO2**, **i12CeO2** and **i20CeO2**) followed the same procedure, resulting in the samples **NP_Pt/i6CeO2**, **NP_Pt/i12CeO2** and **NP_Pt/i20CeO2.** Scheme 4.4 shows the how iPt and NP_Pt catalysts were obtained.

Scheme 4.4: Preparation of iPt and NP_Pt catalysts (with CeO_2 NPs and varying CeO_2 loading from Ce^{3+} impregnation).

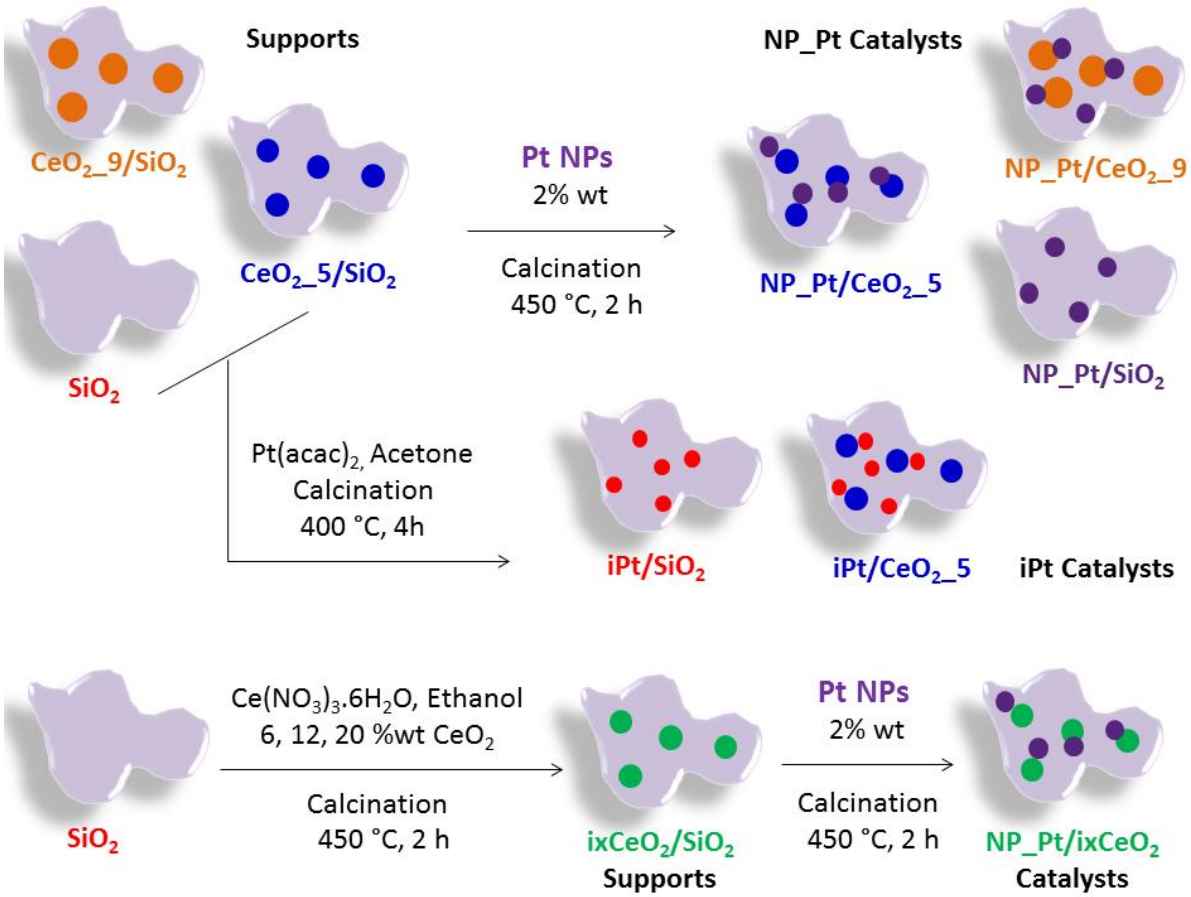

4.2.2CHARACTERIZATION

All samples were characterized by X-ray diffraction (XRD) on a Shimadzu XRD7000 equipped with Cu target (Kα = 1.5406 Å) and a crystal analyzer, operating at 40 kV and 30 mA. For the colloidal NPs the dispersion on hexane was deposited on a Si substrate to reduce the background signal from the glass sample holder. Cerium loadings were obtained by X-ray fluorescence (XRF) in a Shimadzu XRF1800, both techniques available at IQ-UNICAMP. Pt loadings were determined by Inductively Coupled Plasma Optical Emission Spectroscopy (ICP-OES) using an iCAP 6000 Thermo Scientific spectrometer at Italian Institute of Technology (IIT). The powder catalysts were digested in HCl/HNO_3 3/1 (v/v) for 1h at 250 °C, followed by dilution with deionized water (14 mS), and filtered using a PTFE filter (45 µm) before each measurement. For each sample the procedure was repeated three times.

The colloidal NPs were analyzed by transmission electron microscopy (TEM) on a TEM-MSC JEOL 2100 200 kV at Brazilian Nanotechnology National Laboratory at Brazilian Center for Research in Energy and Materials (LNNano-CNPEM) The TEM images for

powder samples were obtained by a JEOL JEM-1400 Plus 120 kV. The experiments performed at LNNano were done in collaboration with Dr. Luelc Souza da Costa.

The catalysts **iPt/SiO2**, **iPt/CeO2_5** and **NP_Pt/CeO2_5** were analyzed by X-ray absorption spectroscopy (XAS) at XAFS2 beamline at Brazilian Synchrotron Light Laboratory (LNLS-CNPEM). The measurements were taken in transmission mode, with ionization chamber detectors and a Si (111) monochromator. The powder samples were diluted with boron nitride and pressed into pellets, which were used for the acquisition of XANES (X-ray absorption near edge structure) spectra collected at room temperature at Pt-L_3 edge (11564 eV). The spectra of Pt foil and PtO_2 references were also acquired for comparison. The samples were also reduced *in situ* under 10% H_2/He (100 mL.min^{-1}) up to 400 °C for 1h and after cooling to room temperature, EXAFS spectra were acquired at Pt-L_3 edge. All procedures for data reduction and analysis were performed as described in section 3.4.2.

4.2.3 CATALYTIC TESTS

WGS reaction was conducted in the catalytic unit previously pictured in Scheme 3.1, section 3.4.3 and the reaction conditions are also similar, except that the amount of catalyst was changed to 25 mg of catalyst and 75 mg of diluent. The reduction was conducted at 400 °C for 1h. Two types of tests were conducted in this chapter, in one the catalytic evaluation was performed at different temperatures (250, 300 and 350 °C), while in the other the catalysts were tested at 400 °C only, at the same temperature and time on stream of the GSR reaction.

For the GSR catalytic runs, the amount of catalyst was varied to have similar Pt amounts or exposed Pt sites for comparison. The catalyst weight ranged from 12-25 mg. The diluent weight was kept at 75 mg. Before the reaction the samples were reduced under 35 mL.min^{-1} of H_2 at 400 °C, 1h. Glycerol solution (glycerol:H_2O molar ratio of 1:13, concentration of 30 % w/w glycerol, 3.27 mol.L^{-1}) was fed to the reactor at a flow rate of 1.9 mL.h^{-1}, (1.04 mmol.min^{-1}) with 40 mL.min^{-1} of He as carrier gas. The reaction was conducted at 400 °C for 2h. It was noted the assessment of the catalytic activity could be improved (compared to the ones in Chapter 3) to ease the comparison of reaction rates with data from literature, thus some reaction parameters and measurements were modified for this catalyst set.

The total flow of gaseous products in the outlet of the reactor was measured by a calibrated rotameter to allow the estimate of glycerol conversion to gas products, which was obtained by carbon basis, using the molar flow ratio of detected gaseous carbon products and the inlet carbon flow on glycerol feed.

$$\textit{Glycerol conversion to gas products (\%)} = \frac{(\boldsymbol{fCO_2} + \boldsymbol{fCO} + \boldsymbol{fCH_4}) * \mathbf{100}}{\mathbf{3} * \boldsymbol{f_{gly,inlet}}} \quad \text{(Equation 4.1)}$$

Where fCO_2, fCO and fCH_4 are the molar flows of gaseous carbon products CO_2, CO and CH_4 (mol.min^{-1}), respectively and $f_{gly,inlet}$ is the glycerol feed. The amount of C_2 and C_3 gas products (such as ethene and acetone) was negligible.

The conversion rate of glycerol to gas products (glycerol molecules converted by minute) was obtained by multiplying the glycerol feed flow rate by the conversion to gas products every 8 min. Each rate value was divided by the amount of exposed Pt sites available on the catalyst bed and thus the glycerol conversion rate per exposed Pt site per minute (Gly_Rate) was obtained.

4.2.4 *IN-SITU* ME-DRIFTS

DRIFTS spectra were acquired by a Vertex 70 infrared spectrometer (Bruker Optics) equipped with a DRIFT cell (Praying Mantis, Harrick) and a liquid nitrogen cooled MCT detector. Two gas flow mixtures could be alternatively allowed inside the DRIFT cell through a gas supply system equipped with mass flow controllers (Bronkhorst) and a two position valve actuator (VICI-Valco). This valve allowed a quick and periodic switch between the two gas mixtures with a desired frequency. Gas exiting the cell was analyzed online through a mass spectrometer (Omnistar, Pfeiffer). Spectra were reported in absorbance units. Prior to the experiments, the catalyst was reduced *in situ* at 400 °C for 1 h under H_2 flow (25 ml min^{-1}) and cooled to the reaction temperature. A background spectrum was collected in He at each temperature before the catalyst exposure to analysis gas.

For CO adsorption experiments, the catalyst was exposed for 10 min to a flow of 1%CO/He, 80 mL min^{-1} and the spectra were collected at room temperature every 10 seconds for the first 2 min (which already showed saturation of Pt surface), then every 30 s for the following 5 min. For CO desorption the flow was switched to He (80 mL min^{-1}) with a 10°C min^{-1} heating rate to 400 °C, while the spectra were collected at the same conditions. After 1h at 400 °C under He, when necessary the flow was changed to H_2, 25 mL min^{-1} and spectra were acquired to observe the desorption of CO from Pt surface.

Modulation excitation spectroscopy (MES) experiments during WGS reaction were carried out through the periodic stimulation of the catalytic system by alternating the gas feed concentration at a given frequency. After *in situ* reduction, at each desired temperature (250 and 300 °C), the catalyst was exposed alternately to a flow of 1 mL min^{-1} CO and 3 mL min^{-1} of H_2O (balance He; total flow 103 ml min^{-1}) and pure He. A second experiment was performed similarly for selected samples, however modulating the feed gas

as CO+H_2O/CO with CO in the same concentration and total flows in both streams. Scheme 4.5 illustrates the experiment and shows that the periodic stimulation (in this case the alternating gas flows) generates a periodic response of the probed species, captured by spectra acquisition. During a modulation period, which comprises one cycle with the two alternating gas atmospheres, CO+H_2O/He (period T = 300 s, frequency, ω = 3.3 mHz), 60 consecutive spectra were collected at resolution of 4 cm^{-1}. Thus, two sets of spectra containing 30 spectra each were acquired for each gas flow in one cycle. Each spectrum is a snapshot of the catalyst surface at a given time in one cycle (for example, at *tx* and *ty* seconds). To increase the signal to noise ratio, the full cycle was repeated twenty–two times; only the last twelve were averaged to take into account the time required for the system to reach a quasi-steady state condition (stabilization time). The resulting averaged spectra, each at a given time (*tx*, *ty*, in time domain), was processed into phase-resolved spectra using phase-sensitive detection (PSD).

The PSD procedure allows the observation of IR active species signals with enhanced signal-to-noise ratio with respect to the time-resolved spectra and filters out all contributions of signals not responding with the same frequency as that of the stimulation (in this case, the variation of the gas feed). The averaged time-resolved spectra collected, which would be response A(t) obtained by MES, was mathematically processed using Matlab® software to extract the kinetic information, i.e., phase domain spectra, by means of the PSD method according to the following equation:

$$\boldsymbol{A_k(\varphi_k^{PSD}) = \frac{2}{T}\int_0^T A(t) sin\left(k\omega t + \varphi_k^{PSD}\right) dt} \qquad \text{(Equation 4.2)}$$

where T is the length of one period, ω is the modulation frequency, k is the demodulation index, φ is the demodulation phase angle for kω demodulation, and A(t) and A_k are the active species response in time- and phase-domain, respectively [96–98,148–150].

Since the stimulation is a periodic function, the frequency of a full modulation cycle is related to a 360 ° phase angle (which corresponds to a 0 ° phase delay). Analysis of the phase angle (0°–360°), i.e., time-delay of reaction intermediates, provides kinetic information of chemical species involved in the surface processes. For example, an intermediate species responding to the modulation in the gas feed with a 350 ° phase responds quickly, with almost the same phase of the stimulation, thus meaning this intermediate is involved in the reaction pathway [96,151]. The intensity of the signals in the phase domain spectra are related to the magnitude of the change caused by the perturbations in the concentration of the feed gas.

Scheme 4.5: Illustration of a MES experiment showing the periodic stimulation (modulation) of a system and the corresponding response of active species (Adapted from [96]).

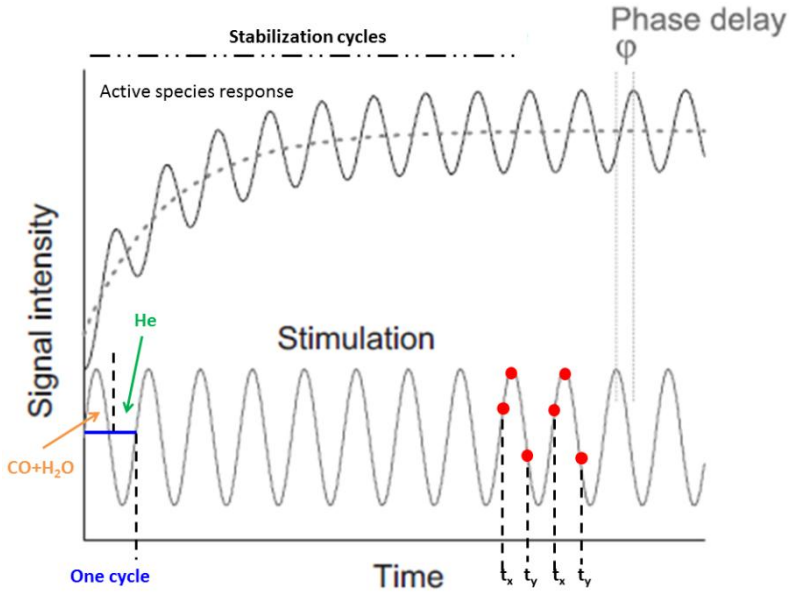

4.3 RESULTS AND DISCUSSION

4.3.1 CHARACTERIZATION

Figure 4.1a shows the XRD for the as-synthetized colloidal 5 nm CeO_2 NPs and the final **iPt/CeO2_5** and **iPt/SiO2** catalysts. The size estimated for the crystalline CeO_2 domain is 5 nm, based on the Scherrer equation using CeO_2 (220) reflection (since (111) and (200) reflections may have contribution from the Si sample-holder). Figure 4.1b shows the TEM image of **iPt/CeO2_5** and the counting of CeO_2 NPs revealed a similar average size of 5.4 ± 0.5 nm, suggesting the CeO_2 NPs would be monocrystalline entities. TEM image also illustrates the dispersion of CeO_2 and Pt NPs over silica surface. It can be seen that the impregnation of the Pt salt generates small Pt NPs, smaller than the 5 nm CeO_2 NPs (see arrows in Figure 4.1.b).

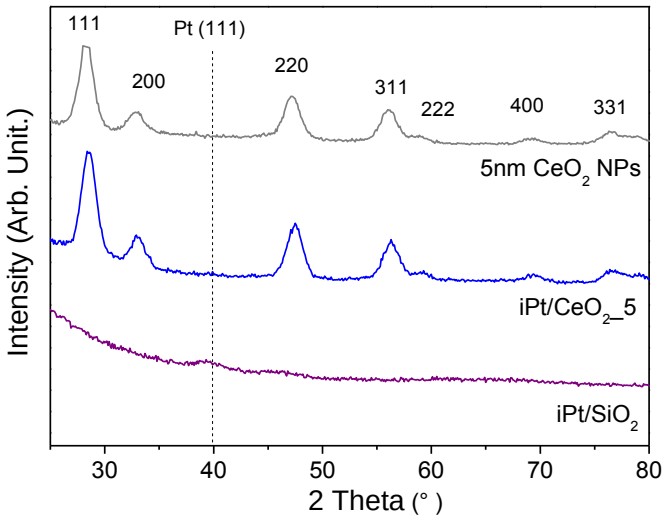

a)

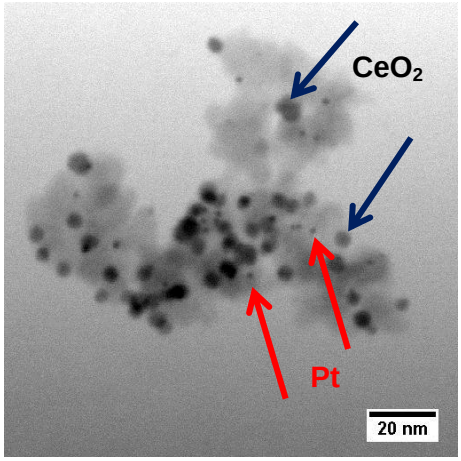

b)

Figure 4.1: a) XRD of colloidal CeO_2 NPs compared to the final catalysts iPt/CeO_2_5 and iPt/SiO_2. The dashed line indicates the position of (111) reflection of Pt fcc structure. b) TEM image of iPt/CeO_2_5 catalyst. The blue arrows indicate CeO_2 NPs and the red arrows indicate Pt NPs.

The XRD in Figure 4.1a indicates the CeO_2 crystalline domain did not increase significantly after the successive thermal treatments for catalyst preparation. The slight increase of the signal around 2θ = 40 ° in **iPt/SiO2** suggests that Pt metallic phase formed on bare silica may have a larger crystalline domain. This observation goes in line with the already know ability of ceria support in stabilizing the metallic phase over the surface [152,153]. Table 4.1 indicates that Ce and Pt loadings were close to the nominal ones (2 % wt.) for **iPt/CeO2_5**, while for **iPt/SiO2** the Pt loading was inferior, reinforcing the stronger interaction of the Pt salt precursor with ceria.

Table 4.1: CeO_2 and Pt loading obtained by XRF.

Sample	% wt. CeO_2	% at. Ce	% wt. Pt	% at. Pt
iPt/SiO2			1.1	0.1
iPt/CeO2_5	11.8	1.5	1.7	0.2

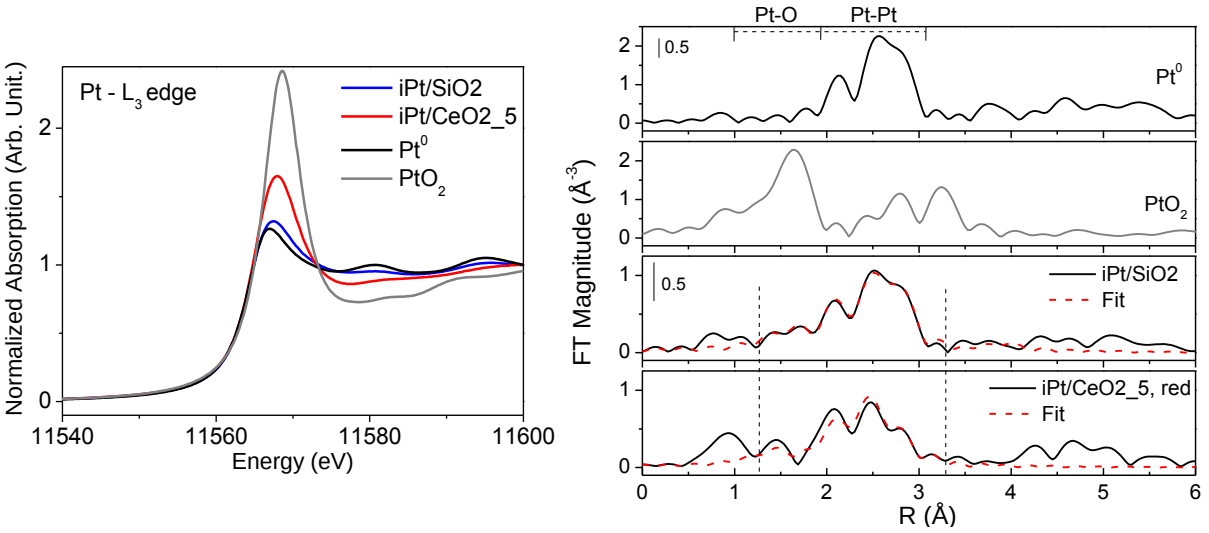

a) b)

Figure 4.2: a) XANES spectra at Pt-L_3 edge for Pt^0 and PtO_2 references and the fresh catalysts **iPt/CeO2_5** and **iPt/SiO2** b) Fourier transform of EXAFS signal for the catalysts **iPt/SiO2** and **iPt/CeO2_5** after reduction (100 mL/min, 5%H_2/He, 400 °C, 1h) and the best fits for the first Pt coordination shell. Vertical dashed lines indicate the fitting range (1.3-3.3 Å) and signals before 1.3 Å mainly arise from data noise.

Figure 4.2a shows XANES spectra at Pt-L_3 edge for as-synthetized **iPt/SiO2** and **iPt/CeO2_5,** where it can be seen that the Pt species are more oxidized in **iPt/CeO2_5**. This is in agreement with the stronger interaction of Pt with CeO_2 NPs [41], corroborating the lower Pt loading and the more crystalline nature of the metallic phase observed for **iPt/SiO2**.

These two catalysts were reduced *in situ* and EXAFS measurements at Pt-L_3 edge were performed under room temperature to observe possible structural differences among the samples and to estimate Pt metallic dispersion. Figure 4.2b shows the Fourier transforms of the EXAFS signals for the references and reduced catalysts, as well as the best fits for the first coordination shell of Pt in the samples. The comparison with Pt^0 and PtO_2 references help visualizing the regions for Pt-O and Pt-Pt contributions. Qualitatively, EXAFS data shows the presence of small Pt domains in both samples (low magnitude of Pt-Pt first nearest neighbors, especially compared to Pt^0 signal) and that **iPt/SiO2** is structurally quite similar with the Pt^0, while **iPt/CeO2_5** exhibits a distinct profile. The structural parameters obtained by the best models are found in Table 4.2 for the reduced catalysts, as well as for the Pt^0 reference.

Table 4.2: Structural parameters obtained by EXAFS analysis at Pt-L_3 edge for the reduced iPt catalysts.

Sample	Pt L_{III} edge				
	Scattering	**CN**	**R (Å)**	**σ^2 (Å^2)**	**R-factor**
Pt^0 reference	Pt-Pt	12[a]	2.769 (0.003)	0.005 (0.001)	0.007
iPt/SiO2, reduced	Pt-O	0.8 (0.1)	1.964 (0.012)	0.006 (0.001)	0.005
	Pt-Pt	7.6 (0.4)	2.755 (0.003)		
iPt/CeO2_5, reduced	Pt-O	0.7 (0.3)	1.856 (0.046)	0.007 (0.001)	0.035
	Pt-Pt	6.9 (1.4)	2.732 (0.012)	0.007 (0.001)	
	Pt-O_L	3.0 (1.6)	3.163 (0.051)	0.007 (0.001)	

[a] fixed, according to fcc structure of bulk Pt.

CN: average coordination number of a given type of scattering (for example, CN_{Pt-Pt} is the average number of Pt neighbors an Pt atom experiences in its first coordination shell)

Pt-O_L stands for a long Pt-O bond, longer than the one found for Pt first nearest neighbors.

For each parameter in the columns there is a correspondent type of scattering, giving the parameters CN_{Pt-Pt} and $_{RPt-Pt}$, R_{Pt-O}, for example.

The quantitative analysis confirms that the CN_{Pt-Pt} are similar to both samples and smaller than Pt^0 reference. It also shows that both samples present a very small CN_{Pt-O} contribution, mostly due to Pt interaction with supports (SiO_2 and/or CeO_2). For **iPt/CeO2_5** an additional long Pt-O contribution is found (Pt-O_L) and although the error in CN_{Pt-OL} is significant, it suggests the existence of a distinct environment for the ceria sample. A long Pt-O bond was already observed in other Pt/CeO_2[41] and other systems and associated to neighbor atoms that do not constitute a chemical bond; it has still to be better understood.

Hence, the impregnation of Pt precursor on these different supports might generate Pt species with distinguished properties, creating an additional variable that may turn the observation of CeO_2 size effects more difficult. To allow the study of the impact of CeO_2 NPs with 5 and 9 nm, a set of catalysts was prepared by the impregnation of pre-formed Pt NPs. Table 4.3 shows Pt and Ce loading determined by ICP and XRF for **NP_Pt/SiO2, NP_Pt/CeO2_5** and **NP_Pt/CeO2_9**, evidencing similar Pt loading for all the samples. In the case of Ce, the **NP_Pt/CeO2_5** sample presents a CeO_2 loading 9% lower than the nominal value (12 %wt.), while for **NP_Pt/CeO2_9** the amount is 30 % lower.

Table 4.3: Pt and CeO_2 loading for NP_Pt catalysts.

	% wt.	
Sample	**Pt**	**CeO_2**
NP_Pt/SiO2	2.0	-
NP_Pt/CeO2_5	2.2	11.0
NP_Pt/CeO2_9	2.1	8.5

In Figure 4.3a, a representative TEM image of the as-synthetized Pt NPs obtained by colloidal method is shown, with mean size of (2.0 ± 0.3) nm. The small size of Pt NPs is reflected on the XRD (Figure 4.3b) by the broadening of (111) and (200) reflections of Pt fcc structure.

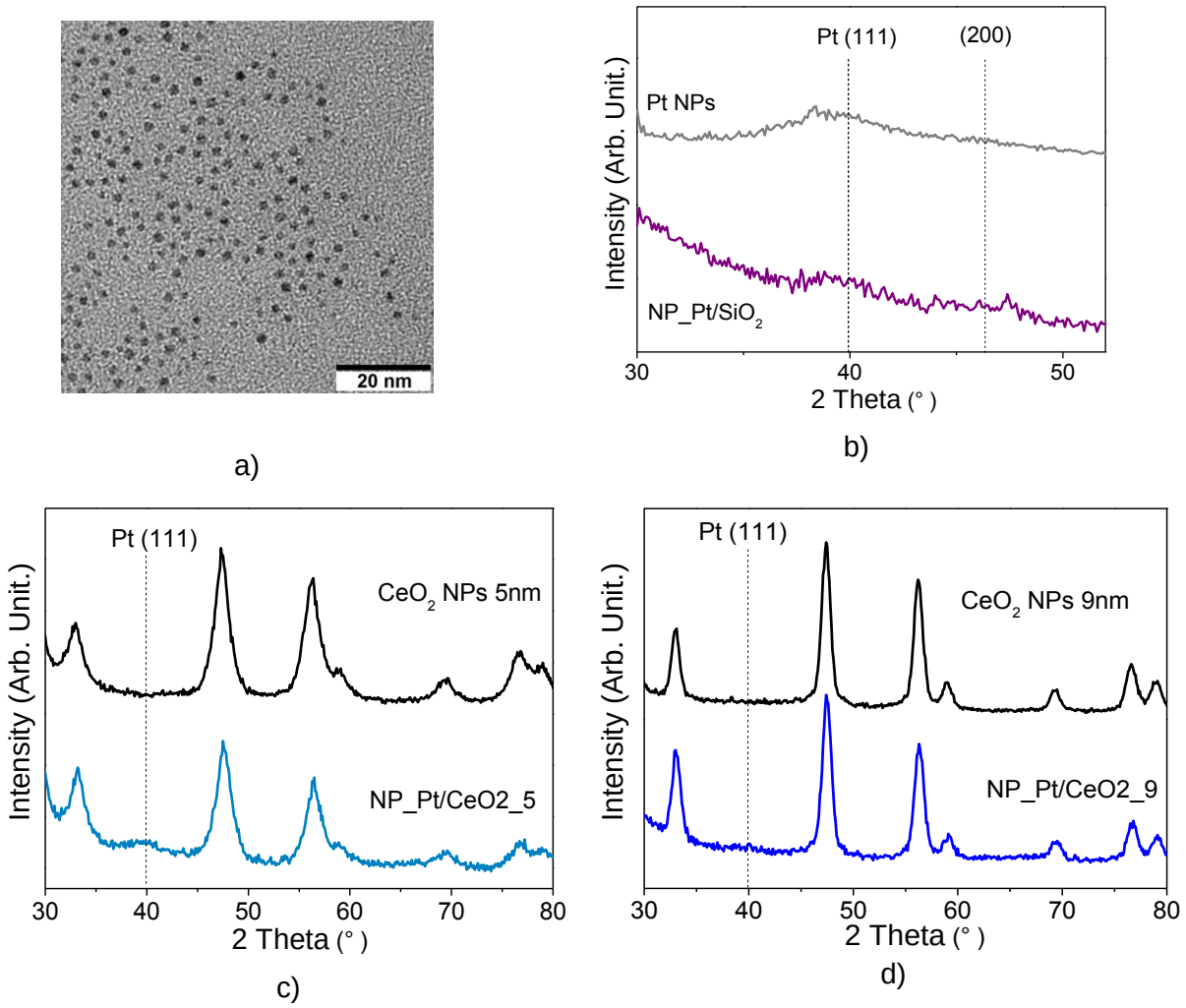

Figure 4.3: a) TEM image of colloidal Pt NPs. XRD patterns of b) Pt NPs and **NP_Pt/SiO2**, c) 5 nm CeO_2 NPs and **NP_Pt/CeO2_5** and d) 9 nm CeO_2 NPs and **NP_Pt/CeO2_9**.

Figure 4.3b-d shows the XRD of catalysts prepared with the Pt NPs. In the case of **NP_Pt/SiO2**, the signal from the amorphous silica is observed from 2θ = 30 ° and it is also not possible to detect reflections from Pt domains. In the case of **NP_Pt/CeO2_5** and

NP_Pt/CeO2_9, by comparing with the CeO_2 NPs patterns, it can be noted the presence of Pt (111) reflection for both catalysts, nevertheless for NP_Pt samples the size estimate for Pt domain is not possible since the reflections are very broad and weak. The comparison of the patterns from catalysts and colloidal CeO_2 NPs indicate no significant changes took place on CeO_2 NPs during the preparation steps.

Figure 4.4 shows TEM images of the final catalysts containing Pt NPs. The counting of NPs showed that after deposition on the support and calcination steps the Pt NPs suffered a slight increase in mean size for **NP_Pt/SiO2,** (2.6 ± 0.7) nm, and for **NP_Pt/CeO2_9,** (2.5 ± 0.6) nm. In the case of **NP_Pt/CeO2_5** catalyst it was not possible to obtain a reliable estimate because the distinction between CeO_2 and Pt phases is not straightforward due to the similarities in size and contrast. Nevertheless, it can be assumed that Pt NPs in all samples have the same mean size on account of the comparable values found for **NP_Pt/SiO2** and **NP_Pt/CeO2_9**.

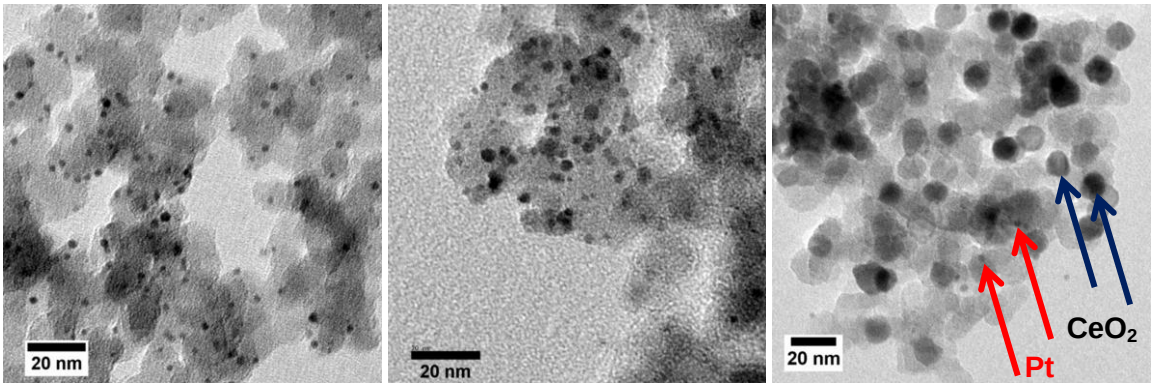

a) b) c)

Figure 4.4: TEM image of final catalysts a) **NP_Pt/SiO2**, b) **NP_Pt/CeO2_5** and c) **NP_Pt/CeO2_9**. The red arrows indicate Pt domains while blue arrows show CeO_2 NPs.

The similar nature of Pt NPs over the different supports was reinforced by CO adsorption experiment results (Figure 4.5a). The normalized spectra for the three catalysts illustrate one main asymmetric band with approximately same widths and maxima around 2070 cm^{-1}. The band at this wavenumber is often associated with CO linearly bound to WC Pt atoms (8-9 Pt neighbors). The similarity of these bands, within the resolution, indicates that CO molecule is bound to Pt sites which are identical regarding their coordination environment in all samples. In other words, intrinsic Pt NPs properties, such as size, Pt coordination number, as well as electronic properties remain constant in this set of catalysts.

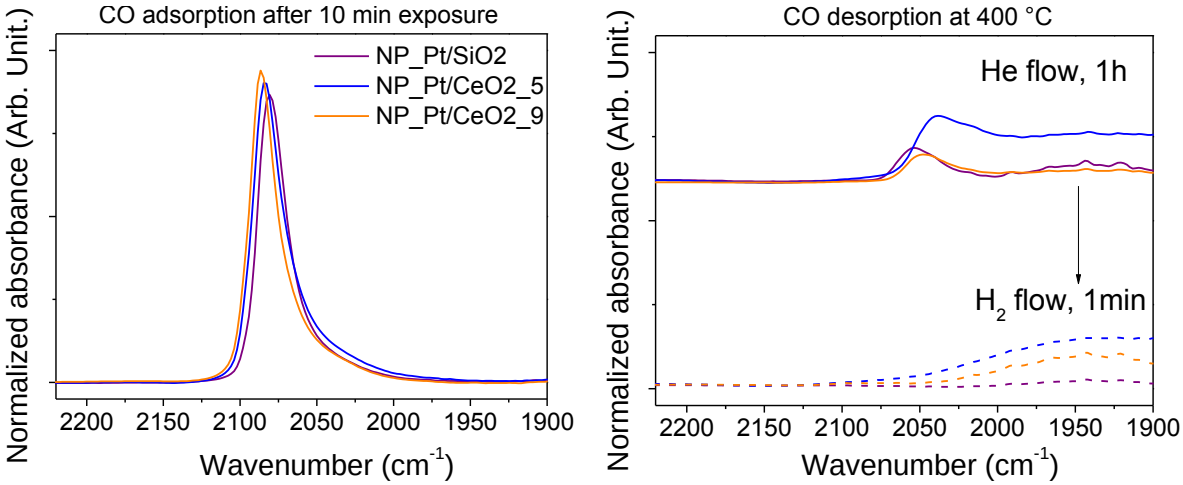

Figure 4.5: DRIFTS spectra of the NP_Pt catalysts a) after exposure to CO flow for 10 min, b) after desorption under He flow at 400 °C for 1h and after 1 min under H_2 flow at 400 °C.

Figure 4.5b shows that after CO desorption under He flow at 400 °C for 1h, a band at 2050 cm^{-1} is still clearly observed, despite the high variation in the signal background due to the high temperature of the DRIFTS cell. This signal at such low wavenumber is usually attributed to CO bound to HC Pt sites [90,91,154,155], and the fact that CO could not be desorbed totally from these Pt sites even at 400 °C illustrates the strong interaction between them. These Pt entities would have a higher electronic density that WC or UC ones, weakening the C-O bond, thus making its vibration appear at lower wavenumbers. The surface of Pt NPs could only be cleaned from CO by flowing H_2, which quickly replaced CO molecules as observed in Figure 4.5b.

To understand the differences between iPt and NP_Pt catalysts, a comparison of the XANES and EXAFS spectra at Pt-L_3 edge is shown in Figure 4.6. From the XANES data in Figure 4.6a the results evidence that the samples containing equivalent ceria NPs but differing in the Pt formation (**iPt/CeO2_5** and **NP_Pt/CeO2_5**) do not show similar Pt species after reduction. While in the **NP_Pt/CeO2_5** platinum is more reduced, close to the profile of metallic Pt reference, in the case of **iPt/CeO2_5** the Pt species are more oxidized.

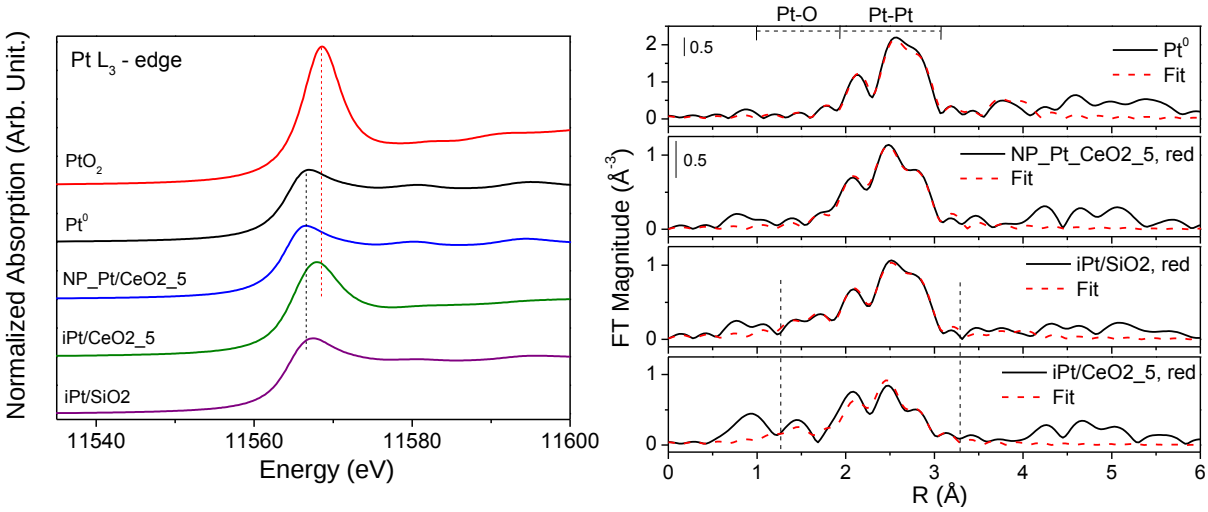

a) b)

Figure 4.6: a) XANES spectra and b) Fourier transform of EXAFS oscillations for the catalyst **NP_Pt/CeO2_5** after reduction (100 mL/min, 5%H_2/He, 400 °C, 1h) and the best fits for the first coordination shell. The results for Pt^0 reference, **iPt/SiO2** and **iPt/CeO2_5** are presented for comparison. Vertical dashed lines indicate the fitting range (1.3-3.3 Å) for all samples.

The analysis of the EXAFS signal (Figure 4.6b) shows that **NP_Pt/CeO2_5** also has a Pt-Pt contribution smaller than the bulk. The quantitative analysis for this sample (representative for all NP_Pt samples), is presented in Table 4.4. It shows that CN_{Pt-Pt} is larger for the NP_Pt samples compared to iPt samples. Also, it is observed that NP_Pt sample does not have a Pt-O contribution at short bond distances as iPt samples, only a similar small Pt-O_L contribution as seen in **iPt/CeO2_5**, which can be an indicative of a different structural feature derived from the Pt-CeO_2 interaction as discussed before.

Table 4.4: Structural parameters of Pt domains for **NP_Pt/CeO2_5** obtained by EXAFS analysis at Pt-L_3 edge.

Sample	**Pt L_{III} edge**				
	Scattering	**CN**	**R (Å)**	**σ^2 (Å^2)**	**R-factor**
Pt^0 reference	Pt-Pt	12[a]	2.769 (0.003)	0.005 (0.001)	0.007
NP_Pt/CeO2_5 reduced	Pt-Pt	8.9 (0.6)	2.743 (0.004)	0.007 (0.001)	0.007
	Pt-O_L	1.6 (0.6)	3.205 (0.028)	0.007 (0.001)	

[a] fixed, according to fcc structure of bulk Pt.

Pt-O_L stands for a long Pt-O bond, longer than the one found for Pt first nearest neighbors.

The dispersion values (Di) could be estimated by EXAFS structural data in Table 4.2 and Table 4.4 as explained in section 3.5.1. Thus, for **iPt/SiO2**, **iPt/CeO2_5** and **NP_Pt/CeO2_5** Pt dispersion values are 96, 100 and 69 %, respectively. The higher Pt

dispersion indicates that iPt samples have more exposed Pt sites over the catalyst surface, hence an increased probability of creating active sites (interfacial sites) than NP_Pt samples in a given amount of catalyst.

Accordingly, the DRIFTS spectra collected for **iPt/SiO2**, **iPt/CeO2_5,** **NP_Pt/CeO2_5** and **NP_Pt/SiO2** (Figure 4.7) at 250 °C under CO+H_2O flow illustrates the dissimilarity of iPt and NP_Pt samples regarding the proportion of Pt sites with different coordination. Despite the presence or absence of CeO_2, the broader bands observed for iPt samples indicate a higher fraction of UC and HC Pt sites than for NP_Pt samples, result that agrees well with the higher Pt dispersion for iPt samples by EXAFS analysis. As seen in Scheme 2.4, the proportion of such sites is related to NP size, thus larger Pt NPs as in NP_Pt samples, (~ 2 nm) would present a smaller fraction of HC and UC sites than the iPt samples (Pt domain barely detectable by XRD), which are probably composed of smaller particles and also may present a less homogeneous size distribution. It is also observed in Figure 4.7c that the distribution of Pt sites on iPt samples are very similar (the inset shows how the bands are well superposed when they are shifted in the *x* axis). There is only a slight difference in the band position that is within the resolution of the measurement. These results contrast to the XANES data (Figure 4.6) that showed that the Pt is more electron deficient in the **iPt/CeO2_5** compared to **iPt/SiO2**, even after reduction. This might be related to the use of dilute hydrogen (5%H_2/He) in the XAFS experiments, which may not be enough to fully reduce the catalysts.

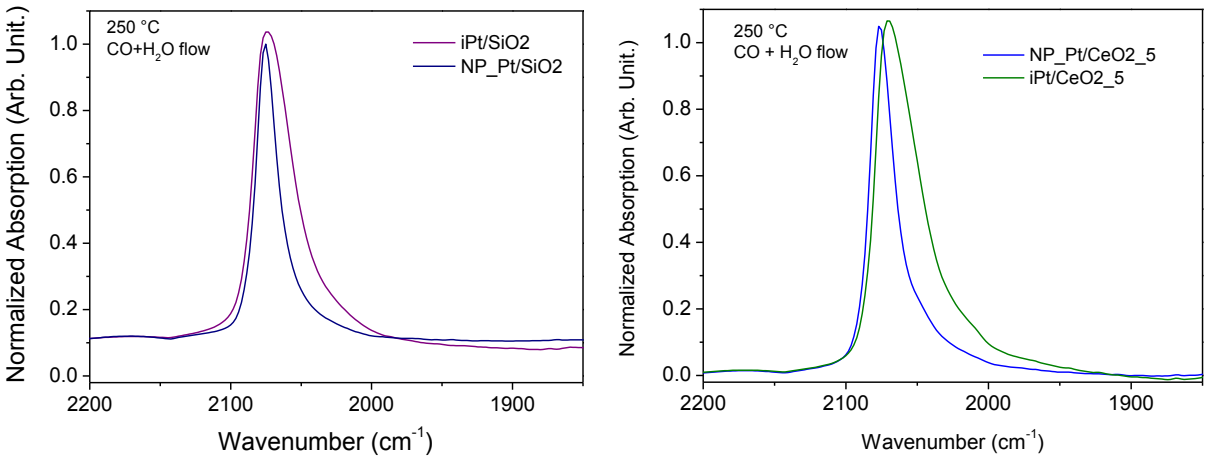

a) b)

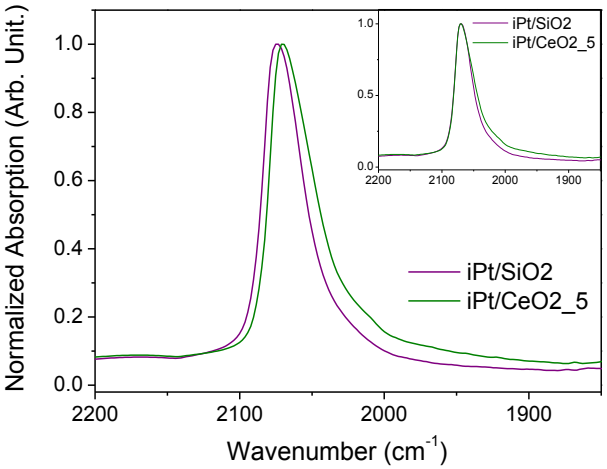

c)

Figure 4.7: DRIFTS spectra of catalysts after exposure to CO+H_2O flow at 250 °C for a) **iPt/SiO2** and **NP_Pt/SiO2**, b) **iPt/CeO2_5** and **NP_Pt/CeO2_5** and c) **iPt/SiO2** and **iPt/CeO2_5**, inset shows the aligned bands on X axis to compare band areas.

Finally, a set of samples obtained from the deposition of the same batch of Pt NPs over the supports containing different CeO_2 loading (formed by Ce^{3+} impregnation) was prepared to keep Pt species as similar as possible in all samples. Such approach would allow a better evaluation of the effect of CeO_2 dispersion over the surface and the size distribution homogeneity of CeO_2 domains on catalytic properties and activity. Figure 4.8a illustrates the XRD profiles of the samples, showing mostly the principal reflections of CeO_2 fluorite structure, suggesting the formation of more crystalline ceria domains with loading increase, whereas Figure 4.8b shows the similarity of Pt species in NP_Pt samples.

The similarity in Pt species over **NP_Pt** catalysts in Figure 4.8b is observed by the band corresponding to CO linearly bound to Pt which shows equivalent shape and whose center only shifted within experimental error among the samples. Therefore, it can be assumed that Pt species over **NP_Pt** samples are equivalent. Table 4.5 summarizes the properties for iPt and NP_Pt samples.

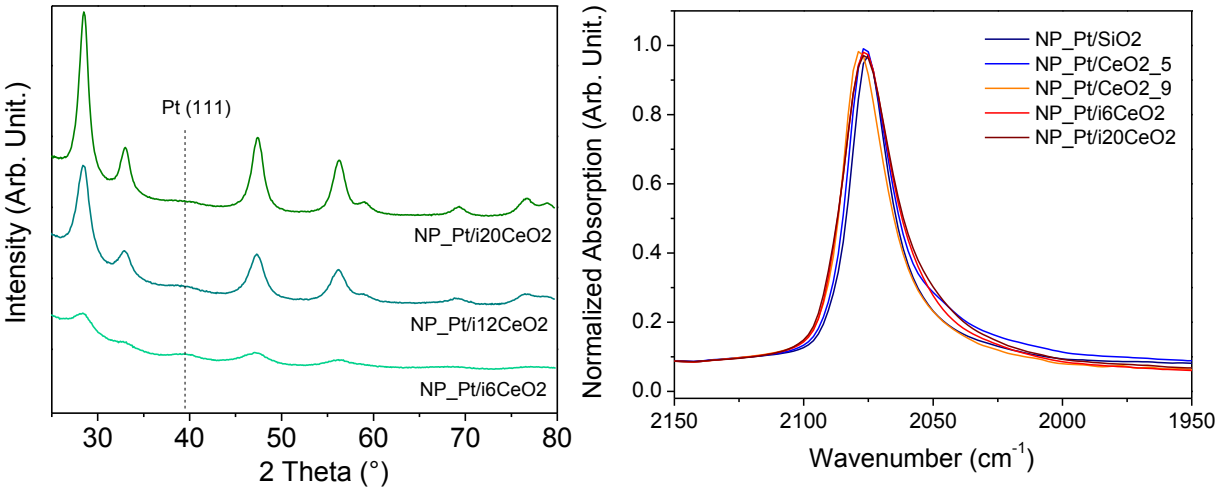

a) b)

Figure 4.8: a) XRD of samples with varying ceria content and b) Normalized DRIFTS spectra showing similar Pt-CO absorption bands for **NP_Pt** catalysts during CO+H_2O gas feed at 250 °C.

Table 4.5: Pt and CeO_2 loading, Pt dispersion and CeO_2 crystalline domain size for the samples.

Sample	**Loading (% wt.)**		**Pt dispersion (%)[a]**	**CeO_2 domain (nm)[b]**
	Pt	**CeO_2**		
iPt/SiO2	1.1		96	-
iPt/CeO2_5	1.7	11.8	100	5
NP_Pt/SiO2	2.0		69	-
NP_Pt/CeO2_5	2.2	11.0	69	5
NP_Pt/i6CeO2	2.1	6.1	69	3
NP_Pt/i12CeO2	2.2	9.1	69	4
NP_Pt/i20CeO2	2.2	16.7	69	5

[a]: Obtained by EXAFS measurements on Pt-L_3 edge (section 4.2.2, Table 4.2 and Table 4.4).

[b]: Obtained by XRD using Scherrer's equation.

In agreement with XRD results, TEM images for NP_Pt samples with varying CeO_2 loading are shown in Figure 4.9. Although the distinction between Pt and CeO_2 domains was not possible, it is noted that for **NP_Pt/i6CeO2** and **NP_Pt/i12CeO2** there are no large CeO_2 domains (since Pt NPs are the same in all samples), with NPs well dispersed over silica. On the other hand, for **NP_Pt/i20CeO2** the presence of larger domains and/or NPs aggregates are evidenced, possibly of CeO_2 due to the increased loading.

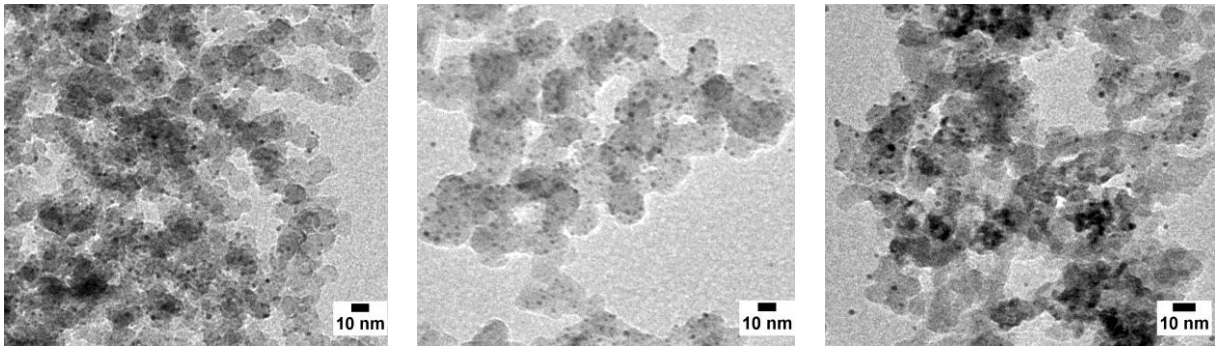

a) b) c)

Figure 4.9: TEM of samples with varying ceria content a) **NP_Pt/i6CeO2**, b) **NP_Pt/i12CeO2** and c) **NP_Pt/i20CeO2**.

In summary, the analysis of this three set of samples showed that iPt catalysts have higher Pt metallic dispersion compared to NP_Pt catalysts. Also, in the former group Pt domains present an increased fraction of HC and UC Pt sites than the ones in NP_Pt samples. Among iPt catalysts, the presence of ceria led to the formation of more oxidized Pt species before reduction with a slight distinct structure when compared to bare silica support. The DRIFTS data indicates, however, that after reduction the Pt species are similar. For the NP_Pt group, Pt species present similar proportion of HC and UC sites and oxidation state and can be regarded as the same in all NP_Pt catalysts. Concerning NP_Pt samples with varying CeO_2 loading, ceria crystalline domains present a slight increase in mean size with loading increment. It is suggested that CeO_2 NPs present a lower degree of dispersion over silica surface and/or broad size distribution at the highest ceria loading (**NP_Pt/i20CeO2**).

4.3.2 WGS REACTION

4.3.2.1 CATALYTIC TESTS

Starting the discussion with the comparison of iPt catalysts, the catalytic activity for WGS reaction at different temperatures for these samples is exhibited in terms of CO conversion in Figure 4.10a. It evidences the promoting effect of ceria, as expected, leading to an increased activity (by up to 35-fold, 300 °C) for **iPt/CeO2_5** when compared to **iPt/SiO_2** sample.

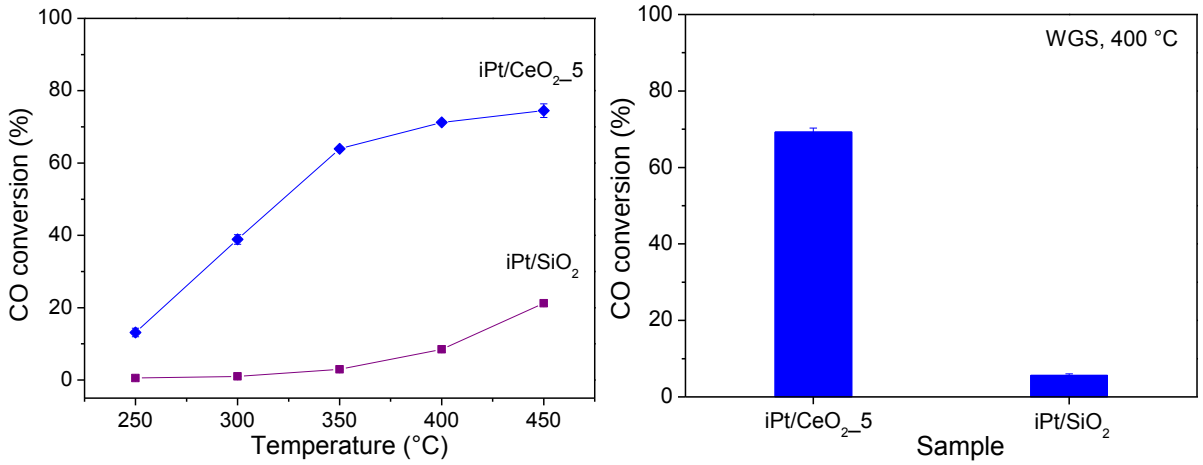

a) b)

Figure 4.10: a) CO conversion (%) of the iPt/CeO_2 catalysts at different temperatures for WGS reaction, normalized by the mass of catalyst, m_{cat}. Conditions: CO:H_2O v/v ratio of 1:3, total flow 115 mL/min, 4.3 % CO. b) average CO conversion of the catalysts during WGS reaction under GSR reaction conditions, 400 °C, normalized by the mass of catalyst, m_{cat}. Conditions: CO:H_2O v/v ratio of 1:3, total flow 115 mL/min, 4.3 % CO, 2 h on stream.

To verify the impact of WGS activity under GSR conditions, the samples were tested for WGS at 400 °C for 2h using the similar amount of catalyst, temperature and time on stream of GSR reaction (section 4.3.3). As shown in Figure 4.10b, the CO conversion levels are consistent to the ones observed in Figure 4.10a and thus it is expected that the samples containing ceria have a significant and similar role in converting CO to CO_2 and steam to H_2 during the GSR reaction.

Concerning the NP_Pt catalysts, the catalytic activity observed for WGS reaction at 400 °C is shown in Figure 4.11a. As in the case of the iPt catalyst, **NP_Pt/SiO2** catalyst shows very low activity compared to **NP_Pt/CeO2_5.** **NP_Pt/CeO2_5** also presents higher CO conversion than **NP_Pt/CeO_2_9**.

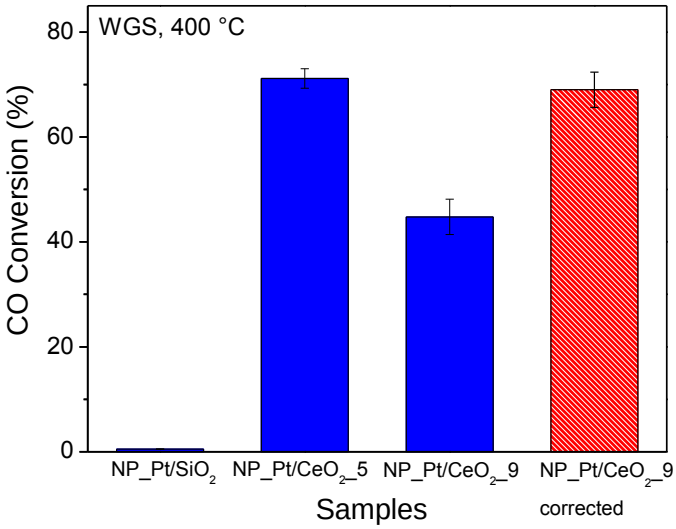

Figure 4.11: WGS activity of **NP_Pt** catalysts at GSR conditions, 400 °C normalized by the mass of catalyst, m_{cat}, together with the corrected conversion for the NP_Pt/CeO_2_9 sample with respect to the ceria loading and probability of formation of Pt-Ce sites. Conditions: CO: H_2O v/v ratio of 1:3, total flow 115 mL/min, 4.3 % CO, 2 h on stream.

To understand the difference in activity of **NP_Pt/CeO2_5** and **NP_Pt/CeO2_9** two main factors have to be evaluated: the amount of interfacial Pt-Ce sites, which are believed to be the active ones for the reaction [41,49,50] , and differences in reactive due to Pt and/or CeO_2 size effects. The creation of interfacial Pt-Ce sites depends on the probability of contact between both phases, which is related to the exposed areas of CeO_2 and Pt. Since Pt NPs have the same size in these two samples, the probability of creating interfacial sites rely on Pt loading and CeO_2 NPs loading and size.

To evaluate if the lower CeO_2 loading (30% lower) and larger particle size of **NP_Pt/CeO2_9** led to the decreased activity compared to **NP_Pt/CeO2_5**, an attempt to normalize the CO conversion taking into account the CeO_2 exposed area was performed. Table 4.6 shows the available areas of CeO_2 and Pt per gram of catalyst for both samples, calculated based on loading, determined by XRF, and particle size, estimated by XRD for CeO_2 (crystalline domain) and by TEM, in the case of Pt NPs.

Table 4.6: Available areas of CeO_2 and Pt per gram of catalyst, as well as the percentage of Pt that could interact with CeO_2.

Sample	CeO_2 exposed area (m^2/g)	Pt available area (m^2/g)	Probability of Pt to interact with CeO_2 (%)
NP_Pt/CeO2_5	9.4	9.3	100
NP_Pt/CeO2_9	4.1	8.7	47

In the case of CeO_2, to determine the amount of particles per gram of catalyst, it was considered the loading and that in one CeO_2 unit cell (fluorite structure) there are 4 Ce atoms (stoichiometric composition). Assuming a spherical CeO_2 NP, the total surface area of ceria was calculated (Scheme 4.6). The fraction which is available over the surface of silica corresponds to half of this value, assuming that the half of the particle is exposed. This rough estimate suggests that **NP_Pt/CeO2_5** has about twice the CeO_2 exposed area than **NP_Pt/CeO2_9.**

Regarding Pt NPs, since the same batch was used and the loading was similar, the exposed area was also similar (Table 4.6). The latter was calculated based on the projected area of a spherical Pt NP (area of the base of a half sphere) which would be available to interact with the CeO_2. As consequence, when we deposit the Pt NP in the CeO2_5 or CeO2_9 supports, the probability that the Pt NPs interact with the CeO_2 NPs will mostly be determined by the CeO_2 exposed area, which is twice for the **NP_Pt/CeO2_5** catalyst, reflecting directly in the number of Pt-Ce interfacial sites. Scheme 4.6 shows the model applied to estimate the exposed area of NPs over **NP_Pt/CeO2_5** and **NP_Pt/CeO2_9**.

Scheme 4.6: Illustration of the model used to estimate the exposed area of CeO_2 and Pt over the catalysts.

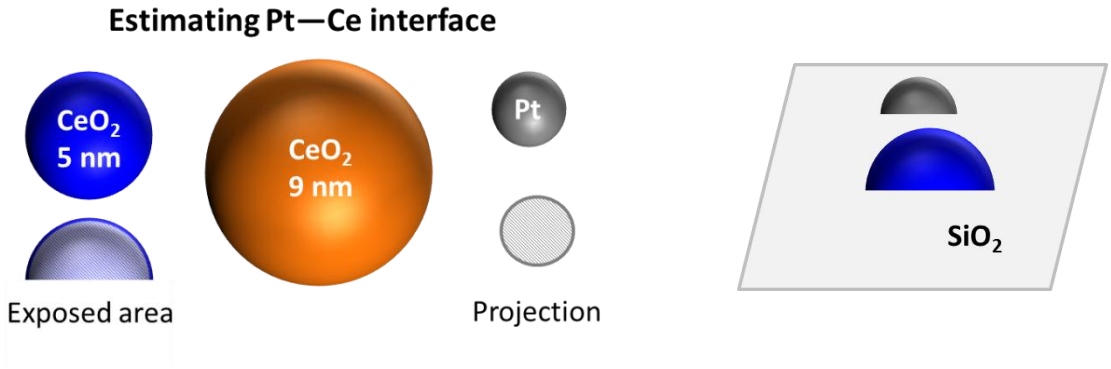

Thus, if the probability difference (100-47=53%) is applied to the CO conversion found for **NP_Pt/CeO2_9**, the catalytic activity reaches the level exhibited for **NP_Pt/CeO2_5**, as illustrated in Figure 4.11 (red bar). This observation (although involving rough approximations) suggests that the difference in catalytic activity between these samples may be related to the probability of creating Pt-Ce interfacial sites, and not to an intrinsic size effect of CeO_2 NPs.

The creation of Pt-Ce interfacial sites with Ce loading was investigated by Buitrago *et al.*[82], by comparing Pt catalysts with different CeO_2 amounts supported on activated carbon. The authors attributed the higher activity of the sample with the highest ceria loading (40% wt) to the increased probability of creating Pt/CeO_2 interfacial sites. The

enhanced WGS activity with incremental Ce loading was also demonstrated by Meira *et al.*[41], and the creation of new interfacial sites was suggested as the main reason for the improvement. Nonetheless, it is important to mention that the samples studied in the two aforementioned works were obtained without any size control of CeO_2 domain, by impregnation of the Ce precursor salt, and the variation in ceria loading would certainly create CeO_2 domains with distinct properties, such as the size. In that case, varying the size and the amount of supported CeO_2 with the loading, the magnitude of exposed CeO_2 area would depend on a compromise among them. Additionally, the increment in Pt-Ce interfacial sites would also depend of the Pt loading; however no attempt to correlate such parameters with the creation of new interface sites was demonstrated.

Although size effects could be expected in our samples, as described in Chapter 2, the difference in the performance of both catalysts were small and can be taken into account considering possible differences in the creation of Pt-Ce interfacial sites.

To get further insights about the role of Pt and CeO_2 size effects as well as the Pt-Ce interface, a larger set of samples were evaluated in WGS as a function of temperature. Table 4.7 summarizes the characteristics of the catalysts tested for WGS reaction. Figure 4.12a shows the CO conversion per m_{cat} follow the order: **iPt/CeO2_5** > **NP_Pt/CeO2_5** > **NP_Pt/i6CeO2** > **iPt/SiO2** ~ **NP_Pt/SiO2** (at 350 °C). Although **iPt/CeO2_5** has the highest CO conversion levels among the tested samples, it also has more Pt and Ce exposed sites (about 3x, Table 4.7). Indeed, it can be observed in Figure 4.12b that the activity per each Pt active site) (given by the CO_2 rate as the amount of CO_2 molecules produced per exposed Pt site per min) follows a different order: **NP_Pt/CeO2_5** > **iPt/CeO2_5** > **NP_Pt/i6CeO2** > **iPt/SiO2** ~ **NP_Pt/SiO2** (at 350 °C), where the **NP_Pt/CeO2_5**, is the most active one.

Table 4.7: Samples tested in WGS at different temperatures. The amount of Ce and Pt sites corresponds to the total number based on the mass used in the catalytic test.

Sample	**Loading (% w/w)**		**Mass of catalyst (mg)**	**CeO_2 (x10^{-6} mol)**	**Pt sites (x10^{17})[a]**	**Exposed Ce atoms (x10^{18})**
	Pt	**CeO_2**				
iPt/SiO2	1.1		75		23.9	
iPt/CeO2_5	1.7	11.8	75	52.1	39.0	10.0
NP_Pt/SiO2	2.0		25		10.6	
NP_Pt/CeO2_5	2.2	11.0	25	16.5	12.3	3.3
NP_Pt/CeO2_9	2.1	8.5	25			
NP_Pt/i6CeO2	2.1	6.1	25	9.1	11.7	3.2

[a]: Obtained using Pt dispersion estimated by EXAFS.

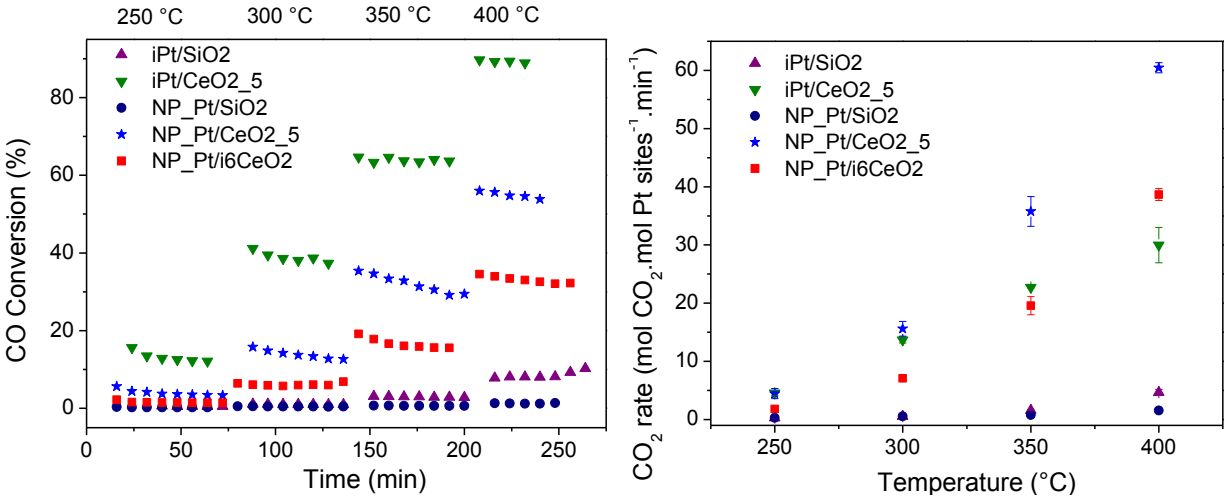

Figure 4.12: WGS activity at different temperatures: a) CO conversion (%) per m_{cat} and b) corresponding CO_2 rate per Pt exposed site. Conditions: CO:H_2O v/v ratio of 1:3, total flow 115 mL/min, 4.3 % CO.

Interestingly, when we calculate the rate of CO_2 production per exposed Ce atom or per total Ce amount (Figure 4.13), we can see that trend in the first case is similar to the CO_2 rate per Pt site, indicating that the exposed Ce factor is more related to the activity than the CeO_2 total amount (mol). The rates per exposed Ce atoms indicates that even with 3 times less Pt sites the activity of **NP_Pt/i6CeO2** is very similar to **iPt/CeO2_5**, and eventually overcomes it at 400 °C. The results suggest that part of the exposed Pt sites on **iPt/CeO2_5** is not contributing to the activity. One possibility is that only a portion of the Pt sites (mostly HC Pt sites, even from single atoms) are interacting strongly to the ceria, being the real active sites, whereas the majority of Pt atoms would not be involved in the reaction, with similar behavior of Pt over bare silica [55,156,157]. Another possibility is that some HC Pt sites not in close contact with ceria could be strongly poisoned by CO, decreasing the number of available active sites. It can also be observed in Figure 4.12b for **NP_Pt/CeO2_5** and **NP_Pt/i6CeO2** (which have similar Pt and CeO_2 exposed sites) that the CO_2 rate is higher for the former. This could be a reflection of the effectiveness of the interface Pt/Ce formed on each sample, but with the data so far to propose an explanation is not straightforward.

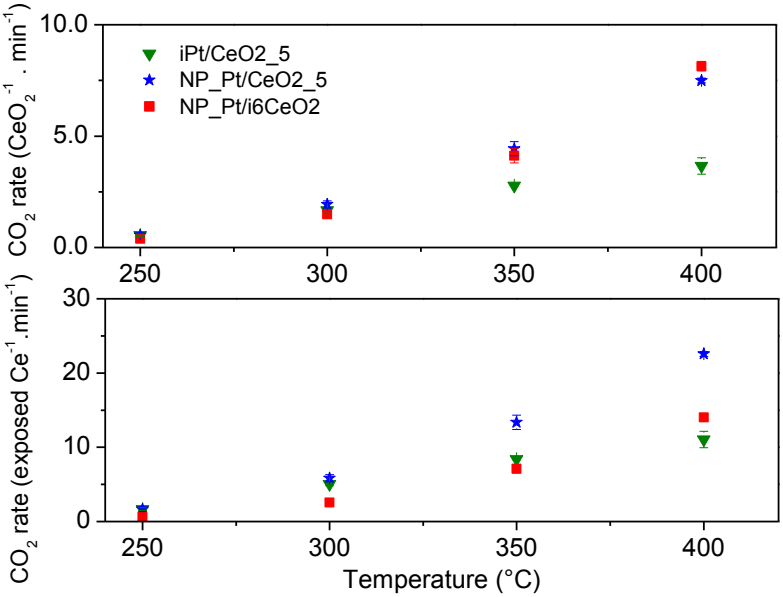

Figure 4.13: CO_2 rates normalized by CeO_2 content (by mol and by exposed Ce atoms).

To rationalize these results, we have to take into account what are the most likely active sites in the WGS reaction. Therefore, a detailed analysis for selected samples was performed by ME-DRIFTS coupled with PSD, as explained in section 4.2.4.

4.3.2.2 *IN SITU* ME-DRIFTS

To better understand the relation of parameters such as the presence and the size of CeO2 with catalytic activity towards WGS reaction, in situ ME-DRIFTS coupled with PSD method was performed for selected catalysts. The reaction was conducted at 250 and 300 °C and the spectra acquired in time domain (Figure 4.14) under the modulation of reactants (CO+H2O/He) was transformed to phase domain spectra (Figure 4.15) by the PSD methodology. The spectra were divided in three wavenumber regions for clarity, high (HWR), middle (MWR) and low (LWR) wavenumber regions. In time domain spectra, it is possible to observe all the bands associated to the intermediate species formed on the surface during reaction (CO+H2O stream) and also the ones remaining during pure He flow. On the other hand, the phase domain spectra only shows the bands related to intermediates that are responding to the modulation of gases (true active ones), whereas the bands associated to spectator species remaining on the catalyst surface vanish. Therefore, it is possible to distinguish true active intermediates from the spectator species, which do not contribute to the reaction pathways, obtaining insights about the reaction mechanism. Additionally, kinetic information can also be provided by phase domain spectra, through the phase angles of the maximum signal corresponding to an active intermediate. Each intermediate will respond to the periodic stimulation (gas changes) with a given phase angle (from 0 to 360 °) and will

then present a phase delay in relation to the corresponding stimulation frequency. The species showing high phase angles, for example, 350 °, respond fast to the stimulation, with a phase delay of only 10 °, while species with low phase angles, 160 °, respond more slowly, with a delay of 200 ° in relation to the modulation frequency [96,98,151,158].

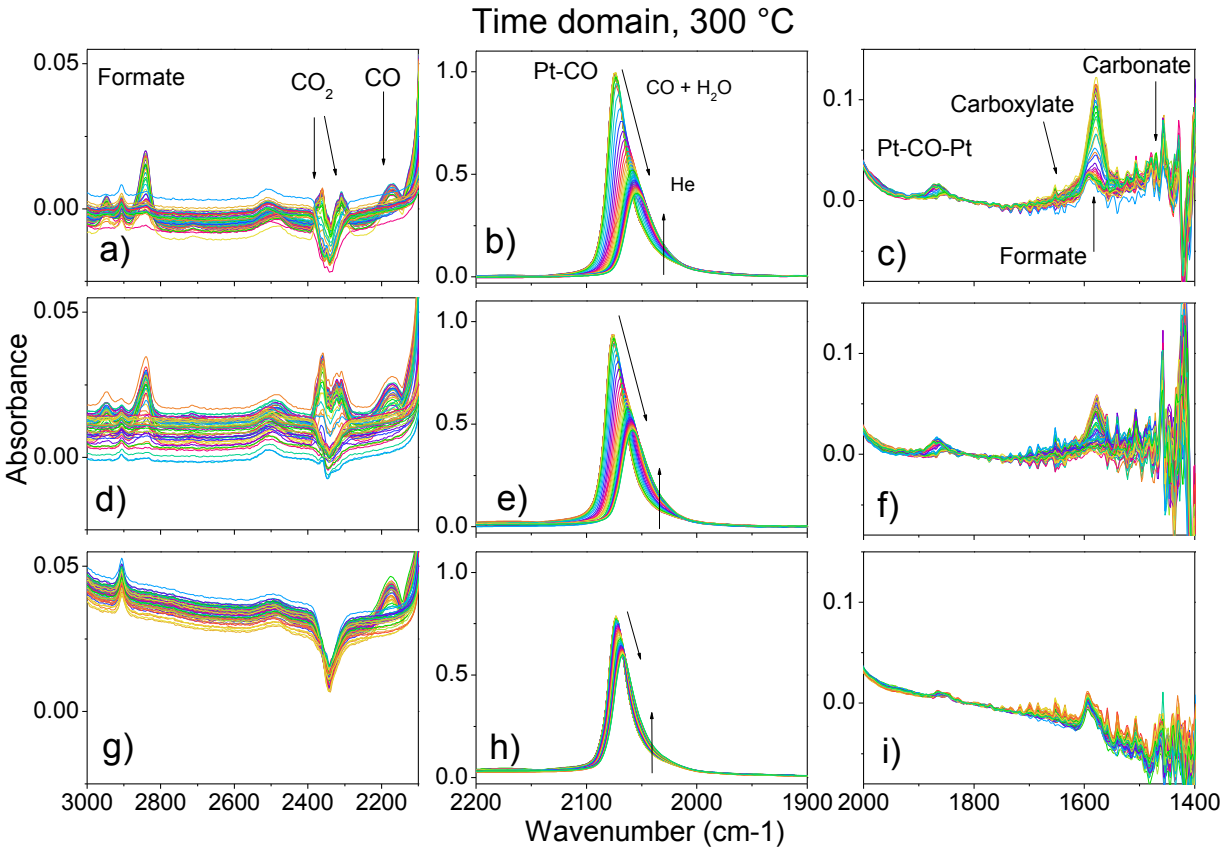

Figure 4.14: Time domain spectra during reactants modulation ($CO+H_2O$/He) cycle at 300 °C, shown in three wavenumber regions, 3000-2100 cm^{-1} (HWR), 2200-1950 cm^{-1} (MWR) and 2000-1400 cm^{-1} (LWR) for: a-c) **NP_Pt/CeO2_5**, d-f) **NP_Pt/CeO2_9** and g-i) **NP_Pt/SiO2**.

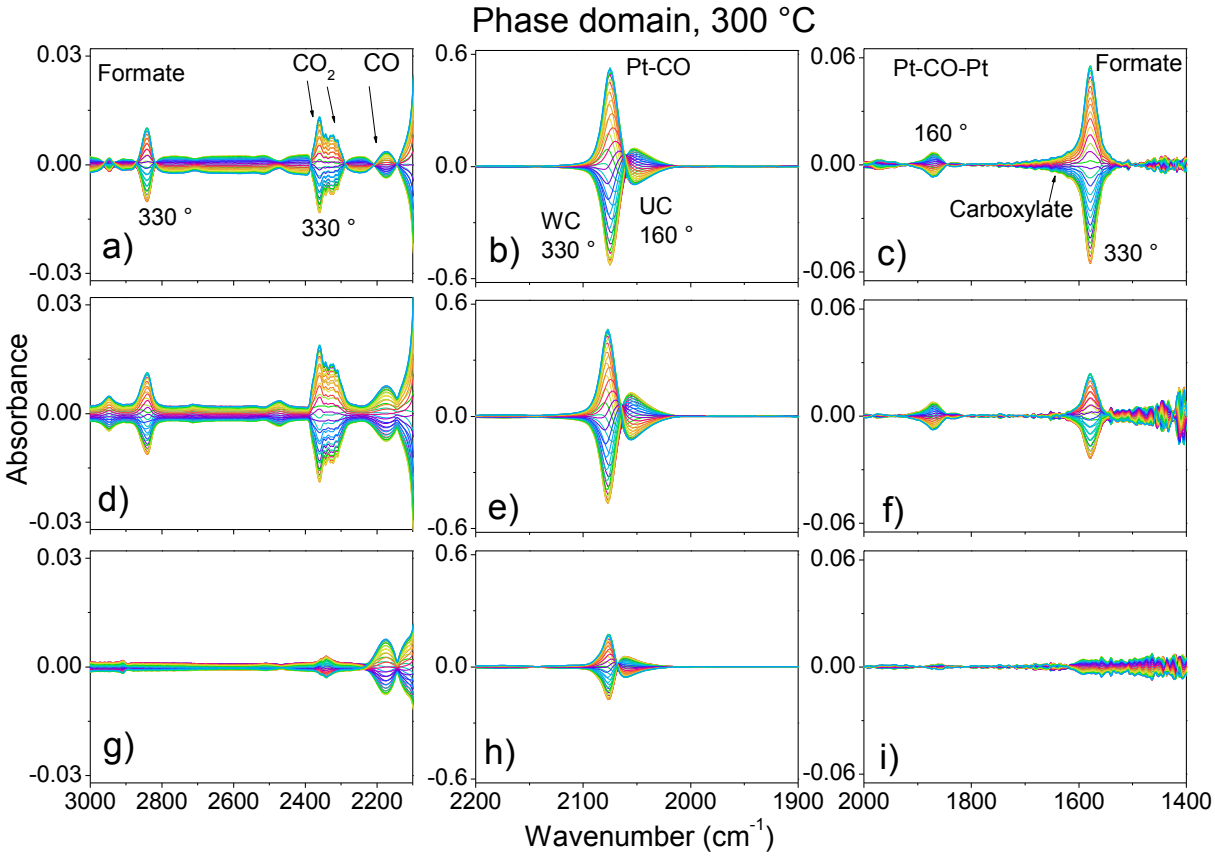

Figure 4.15: Phase domain spectra during reactants modulation ($CO+H_2O$/He) cycle at 300 °C with the corresponding phase angles for each intermediate for: a-c) **NP_Pt/CeO_2_5**, d-f) **NP_Pt/CeO_2_9** and g-i) **NP_Pt/SiO_2**.

We will start the description of all surface species identified from time domain spectra shown in Figure 4.14; later, from the phase domain spectra (Figure 4.15), the distinction between true active and spectator species will be provided; and lastly, the kinetic information about the reaction pathway will be discussed. Observing Figure 4.14 it is clear that to retrieve information about how the active species are evolving from the time domain spectra is not straightforward. All averaged spectra collected over time during the modulation of reactants are shown, i. e., 30 spectra acquired under reaction feed ($CO+H_2O$) and 30 under He. On the HWR, (Figure 4.14a, d, g), the bands corresponding to vibrations of gas phase CO_2 (2400-2300 cm^{-1}), as well as formate bands (C-H stretching, 3000-2850 cm^{-1}) and gas phase CO (2170 cm^{-1}) appear. The presence of OH groups (from water and support) causes an intense variation in the background in this region. The MWR (Figure 4.14c, f, i) exhibits the CO stretching band from a bridged Pt-CO-Pt species, as well as bands assigned to OCO stretching, related to other possible WGS reaction intermediates such as carboxylates (COO^-), formates ($HCOO^-$) and carbonates (CO_3^{2-}) [148,158,159] . The latter region (Figure 4.14g-i), the HWR mainly shows the bands corresponding to formate species (2900 cm^{-1}) and free CO. The formate is also observed in the LWR (1590 cm^{-1}), while the band for

CO linearly bound to Pt is observed in the MWR, 2070 cm^{-1}. These would be species formed on the catalyst surface during reaction, however, there is barely no evolution of CO_2-related bands between 2200-2400 cm^{-1}. Additionally, the linear Pt-CO species changes only slightly with the modulation of the reactants, showing a shift in the maxima of the band to lower wavenumber with the switch from CO+H_2O to He flow. Under CO+H_2O gas stream, the CO coverage of Pt surface increases fast and remains high (reaching the saturation of Pt surface at this temperature). When the atmosphere is changed to He, there is a stepwise decrease in intensity and shift of the center of the band to lower wavenumbers due to decrease in the CO coverage on Pt. This sharp band centered at higher wavenumbers due to high CO coverage can be related to two effects: one static and one dynamic. The static effect can be understood considering the Pt metallic phase as a source of electrons. With the increase of adsorbed CO molecules on the metal, it becomes poorer in electrons and then diminishes the back donation to a single CO molecule, thus causing the strengthening of CO bond. The dynamic effect concerns with the coupling between molecular dipoles, the intensity of low wavenumber vibrations can be transferred to high wavenumbers ones on account of the coupling of CO vibrators[160]. Thus, the observed shift in the band corresponding to linearly bound Pt-CO in time domain spectra (Figure 4.14h) towards lower wavenumbers is in agreement with the decrease in CO coverage on Pt surface due to desorption under He flow and/or to conversion to CO_2. Taking into account the very low catalytic activity of **NP_Pt/SiO_2** sample, the desorption is the most important contribution.

Figure 4.14a-f shows the spectra for the ceria catalysts, which have very similar behavior. It is observed the appearance of CO_2 bands (2200-2400 cm^{-1}) and more intense formate bands between 2800-3000 cm^{-1}, along with the one at 1590 cm^{-1}. The presence of the bands related to bridged Pt-CO-Pt species (1950 cm^{-1}) and the shoulders corresponding to carboxylate and carbonate species (1660 and 1500 cm^{-1}, respectively) are also more evident. Moreover, the change in the band corresponding to linear Pt-CO species with the modulation (MWR) is more expressive compared to the **NP_Pt/SiO_2** catalyst, exceeding the effect of the decrease in CO coverage. Since the CO adsorption is similar in the three samples (Figure 4.8b) these results show that such entities are more easily desorbed and/or converted from Pt surface on ceria samples with He flow. All these observations are in agreement with the higher activity of **NP_Pt/CeO_2** samples.

Despite the information gathered from time domain spectra in Figure 4.14, it does not allow the distinction between active and spectator intermediate species among the species present on the catalyst surface (formate, carboxylate, carbonates, linear CO bound to Pt, as well as bridged Pt-CO-Pt species). For that, it is important to analyze the phase domain spectra in Figure 4.15. Starting with **NP_Pt/SiO_2**, Figure 4.15g-i, the only evident signals are the ones arising from CO in the gas phase, as well as the linear Pt-CO species.

The latter arises from CO coverage changes with the signal shape (with a node in 2070 cm^{-1}) reflecting the shift of the band to lower wavenumbers. Additionally, the small bands corresponding to formate species identified on time domain spectra have vanished, indicating that they did not respond to the modulation of the gases. This lack of response in phase domain spectra can arise from the following possibilities: a) the formates were formed on the surface by CO+H_2O flow, but were not decomposed to form products CO_2 and H_2 (thus being spectator entities) or b) they actually responded to the modulation of reactants and led to products (being true active intermediates), however their transformation was fast enough to be missed, i. e., the lifetime of such intermediates would be shorter than the time resolution of the measurement. Since it is widely accepted that WGS reaction on Pt/SiO_2 catalysts occurs by the associative mechanism (due to the limited ability of Pt to activate water molecule), it would be expected to identify formate or carboxylate as active intermediate species, responding to the modulation of reactants in Figure 4.15i [53]. Thus, the participation of the formates on the reaction over **NP_Pt/SiO_2** cannot be ruled out, especially taking into account the very low activity at 300 °C shown by this sample, and thus the observation of active intermediate species could be within the detection limit.

Analyzing the phase spectra for ceria samples (Figure 4.15a-f), it is observed a similar behavior again. Also, the variation of the signals related to linear Pt-CO species with the modulation is significantly larger, indicating that despite the changes arising from CO coverage differences, linear Pt-CO entities are key active intermediates for WGS reaction. For both samples, the signals corresponding to formate (low and high wavenumber regions), carboxylate (shoulder near 1660 cm^{-1}) and bridged Pt-CO-Pt entities can also be identified as active intermediates for the catalysts containing ceria. The broad band related to carbonates (observed on time domain around 1500 cm^{-1}, Figure 4.14c,f) vanishes in phase domain, confirming that this entity is a spectator species, in accordance with literature discussed in Chapter 2. For the bands related to gas phase CO_2 on the high wavenumber region, the background signal seems to be deeply affected by the water in the feed and the surface OH of the support, thus to compare CO_2 evolution among the samples by the intensity of the bands is not possible. This is also the reason why the identification of formate species is easier in the low wavenumber region.

Concerning the kinetic information that can be extracted from phase domain spectra in Figure 4.15, it is observed that changing the gas flows results in a fast response (330 °, almost the same frequency as the modulation, 360 °) of the gas product CO_2, CO linearly bound to WC Pt sites and formates (for ceria samples). The signal associated to gas-phase CO also respond fast (330 °), since its concentration is being modulated. For CO bound to UC/HC Pt sites and bridged Pt-CO-Pt the responses are slower (160 °). Given the observations for **NP_Pt/SiO2** sample, such phase angle values for Pt-CO bands can be a

result of both the massive CO coverage variations on the surface and the kinetics of desorption of species over distinct sites. The high phase angle of the band associated to CO on WC Pt sites is consistent with the fast desorption of species bound to these sites and the fast shift of the band center to lower wavenumbers with the He flow. This shift due to the reduced CO coverage can be caused by the fast decrease of CO coupling magnitude (more expressive in NP terraces) and by the increase in Pt electronic density on CO bound to WC Pt sites. In turn, the smaller phase angle for the bands at lower wavenumbers is consistent with the slower response of the bands associated to CO bound to UC/HC Pt sites, since they are less affected by CO coverage effects. Such behavior occurs either because CO is more strongly bound on these sites, thus its desorption and/or conversion are slow, and because CO coupling effect on such sites is not expressive. Regarding the phase angles for CO_2 and formate species, they all respond fast to the gas flow changes (330 °), being involved in the reaction under such conditions. Indeed, the large variation in CO coverage between the two gas streams ended up masking the phase angles related to the behavior of intermediate species.

To obtain more information, especially for the linear Pt-CO region which strongly responds to CO coverage variations, we repeated the experiment for the samples **NP_Pt/CeO2_5** and **NP_Pt/SiO2**, this time cycling CO+H_2O/CO gas flows. It was possible to avoid the shift in the linear Pt-CO band by keeping the CO flow and modulated periodically the water concentration. The aim was to observe the changes on Pt-CO bands under WGS reaction to evaluate whether UC/HC Pt sites have a different participation depending on the support (bare silica or silica with CeO_2 NPs). Figure 4.16 compares the time and phase domain MWR spectra acquired during WGS reaction for **NP_Pt/SiO2** and **NP_Pt/CeO2_5** samples.

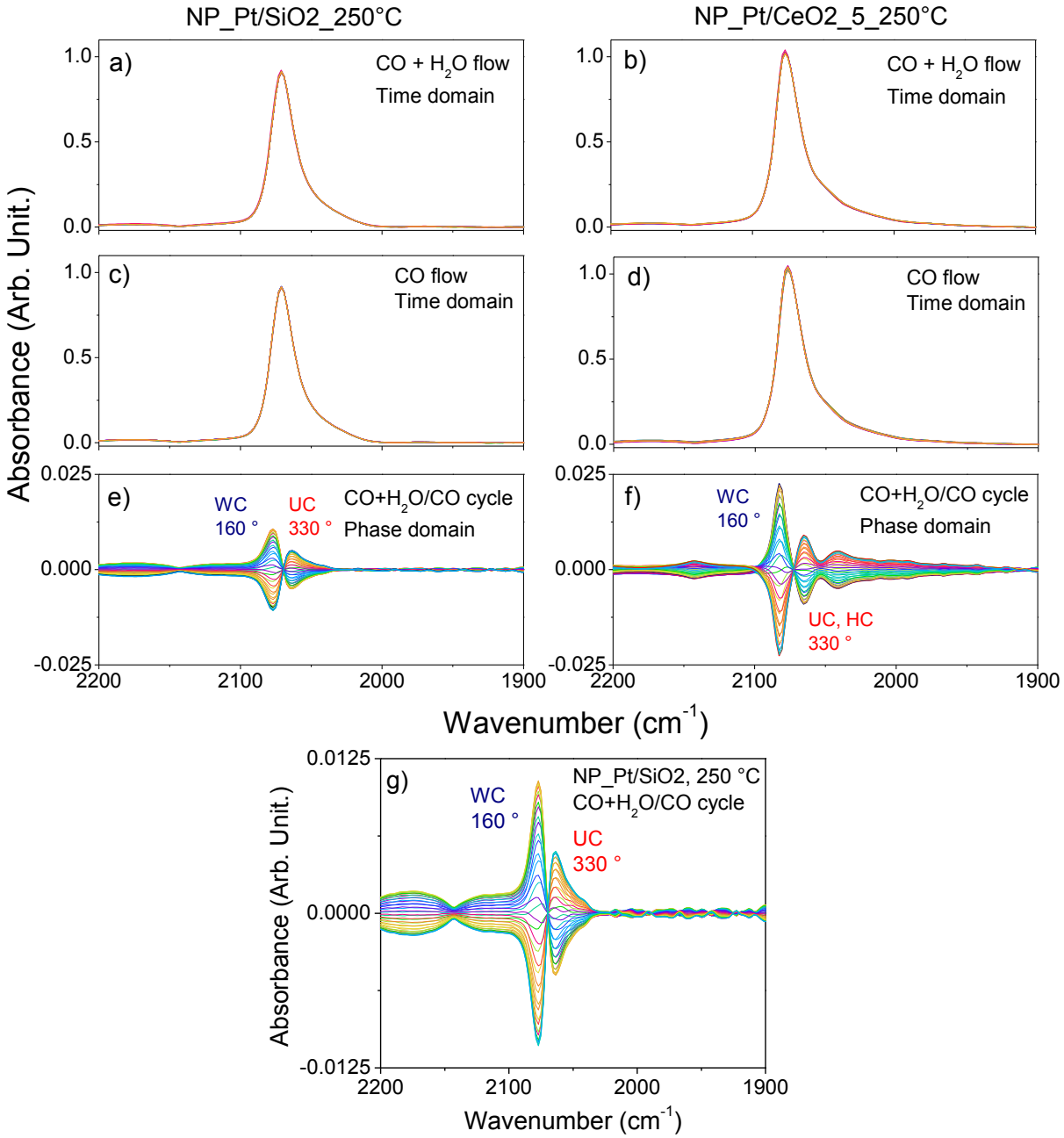

Figure 4.16: Comparison of time domain spectra at Pt-CO wavenumber region for **NP_Pt/SiO2** (left) and **NP_Pt/CeO2_5** (right) during CO+H_2O (a,b) and CO (c,d) modulation flows at 250 °C and the corresponding phase domain spectra (e,f). g) The same phase domain spectra for **NP_Pt/SiO2** (e) at a smaller scale on y axis to better visualize the absence of response of Co bound toHC Pt sites.

Analyzing the data obtained by modulating the presence/absence of water (CO+H_2O/CO cycle) it can be inferred that CO coverage is kept constant, thus it is possible to observe the variations rising only from the reaction of CO bound to different Pt sites with steam. Although the changes are much less pronounced, it is clearly observed in the phase

domain spectra for **NP_Pt/CeO2_5** (Figure 4.16f) the presence of three components, whereas for **NP_Pt/SiO2** (Figure 4.16e) only two are well-defined. For **NP_Pt/CeO2_5,** these three components are consistent with the CO bound to Pt sites with different coordination (WC, UC and HC Pt sites, 2080, 2060 and 2042 cm^{-1}, respectively), whereas for **NP_Pt/SiO2**, the signal corresponding to HC sites is not well-defined. It is also observed that CO bound to low coordination Pt sites (UC and HC) responds faster to the modulation, with a phase angle of 330 °, while WC Pt sites have an intense and more delayed response (phase angle of 160 °). This suggests that CO bound to all Pt sites (WC, UC and HC) have a key role on the reaction mechanism for ceria catalysts (WC and UC for **NP_Pt/SiO2)**, but UC and HC would have faster kinetics than WC, with the CO being readily reactive in the presence of steam. Interestingly, since the Pt NPs are the same in both samples (Figure 4.8b), such HC Pt sites responding for the ceria sample may evidence a direct effect of the interface Pt-CeO_2 on the WGS reaction mechanism. As observed in theoretical studies [50] and in Scheme 2.5, HC Pt sites would be the ones available to both interaction with ceria (corners) and exposure to reactants (CO and H_2O), and only part of them would be in close contact with ceria. The participation of HC Pt sites on **NP_Pt/CeO2_5** would represent both the enhanced Pt activity caused by the interaction with ceria, as well as the clean-up of such Pt sites from CO poisoning, which is again a feature promoted by the interfacial sites.

Therefore, for both samples the phase angles related to CO bound to the different Pt sites shows that UC ones (and HC for **NP_Pt/CeO2_5)** respond faster to the modulation of water, being kinetically more important than WC sites, which present a delayed response. For **NP_Pt/CeO2_5**, the CO bound to HC Pt sites also shows a fast response (330°). The correlation of the phase angles found for the CO bound to distinct Pt sites with the values observed for CO_2 produced during modulation can be helpful to associate the intermediate involved in product formation and also to probe true active sites during reaction. The spectra showing the wavenumber region of gas phase CO_2 and CO during CO+H_2O/CO modulation at 250 °C are shown in Figure 4.17.

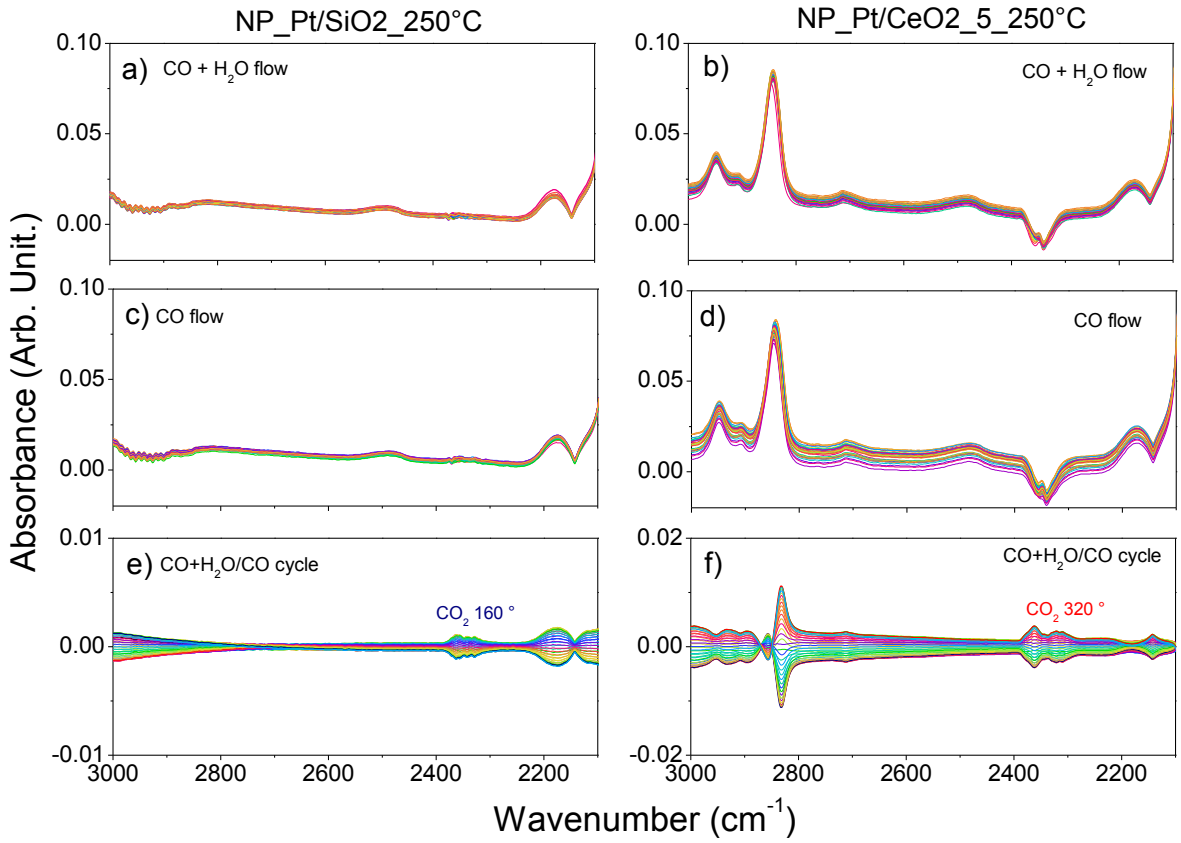

Figure 4.17: Comparison of time domain spectra at high wavenumber region for **NP_Pt/SiO2** (left) and **NP_Pt/CeO2_5** (right) during $CO+H_2O$ (a,b) and CO (c,d) modulation flows at 250 °C and the corresponding phase domain spectra (e,f).

In the case of **NP_Pt/SiO2** (Figure 4.17e), CO_2 exhibits a 160 ° phase, similar to CO bound to WC Pt sites indicating that it is mainly produced on them. In contrast, for **NP_Pt/CeO2_5** (Figure 4.17f), a 320 ° phase angle is observed for the CO_2 signal, similar to CO bound to UC and HC Pt sites, indicating a major participation of CO bound to these low-coordination Pt sites with CO_2 formation. Additionally, since CO bound to HC Pt sites only responds with the modulation on **NP_Pt/CeO2_5**, it is evidenced their exclusive role on WGS mechanism over the ceria catalyst. Therefore, during WGS reaction over ceria catalysts at 250 °C, CO_2 is mainly formed by a faster path involving CO bound to UC and HC Pt sites, whereas a slower path involves WC Pt sites. For **NP_Pt/SiO2**, the reaction pathway mainly occurs by a slow route through CO bound to WC sites**,** while it is possible that UC sites are involved in a faster and minor route. Again, it is difficult to make a similar association with formate bands at high wavenumber region due to the irregular background. The information of formate and carboxylate species can be found in Figure 4.18.

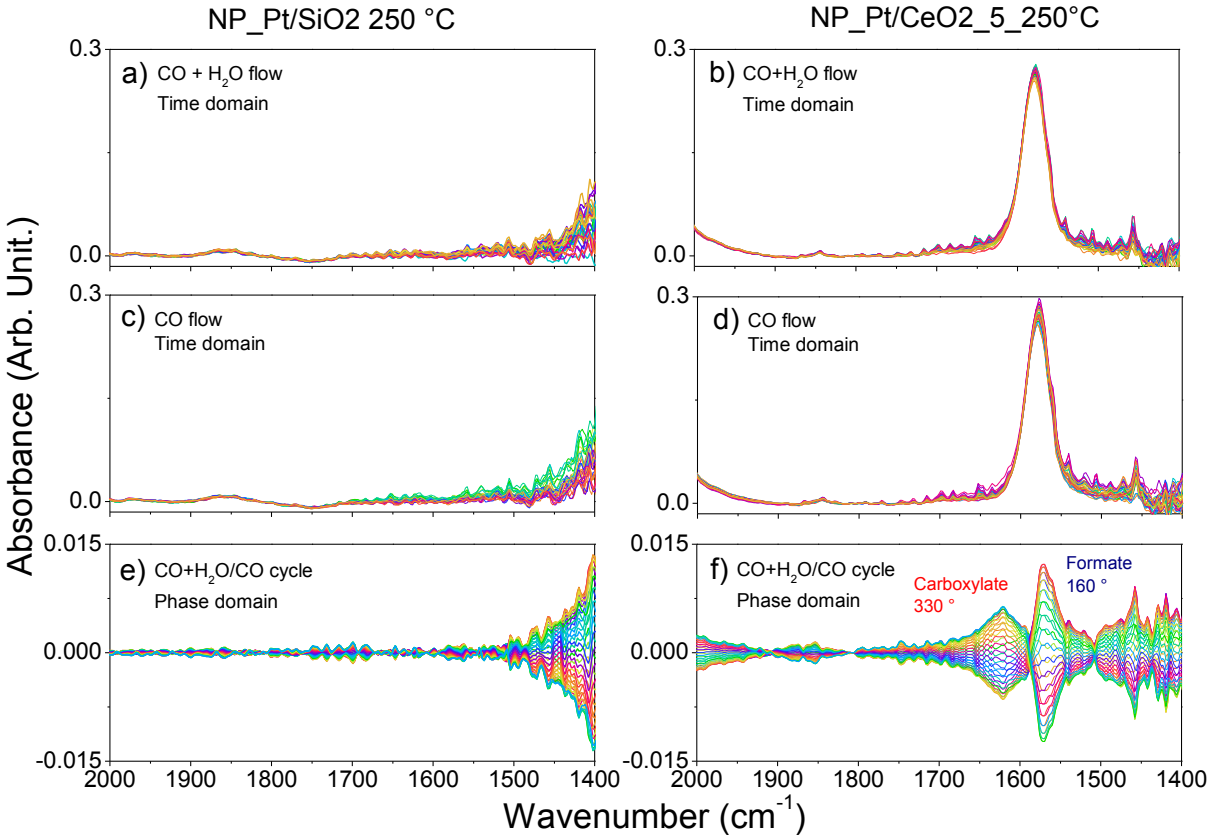

Figure 4.18: Comparison of time domain spectra at low wavenumber region for **NP_Pt/SiO2** (left) and **NP_Pt/CeO2_5** (right) during CO+H_2O (a,b) and CO (c,d) modulation flows at 250 °C and the corresponding phase domain spectra (e,f).

The LWR of the spectra acquired under CO+H_2O/CO cycle at 250 °C (Figure 4.18) shows additional overlapping bands from vibrations of carbon intermediates (carboxylate, formate and carbonate) formed on the catalysts surface. Time domain spectra show an intense band for **NP_Pt/CeO2_5**, whereas for **NP_Pt/SiO2** only broad and less intense signals are evident. For both samples, the band related to bridge Pt-CO-Pt entities is also observed. On the other hand, phase domain spectra for **NP_Pt/CeO2_5** clearly shows that only carboxylate and formate intermediates are responding to the modulation of reactants, while for **NP_Pt/SiO2** no response is detected.

Also, the residual bands observed in time domain spectra for ceria samples indicate that not all carboxylates/formates and CO adsorbed on Pt participate on the reaction rates, remaining bound to the catalyst surface, in agreement with results reported by Kalamaras *et al.* [49] and proposed by Aranifard *et al*.[50].

The analysis of phase angles values for **NP_Pt/CeO2_5** indicates that carboxylate (1620 cm^{-1}) has the same phase delay of the CO bound to UC and HC Pt sites (330 °), while the formate band (1580 cm^{-1}) has the delayed response similar to the ones on

WC Pt sites (160 °). The results shows that while carboxylate and CO bound to UC and HC Pt sites are the active intermediates from the faster path of WGS mechanism, CO bound to WC Pt sites and formate species are also active intermediates but through a reaction route with slower kinetics. Therefore, the results show parallel pathways with different kinetics under these conditions. Nevertheless, it is not possible to identify whether the formation of such intermediates occurs by the classic “associative” or the “associative mechanism with redox regeneration” pathways, due to the inability to probe the response of oxygen vacancies. Additionally, for the same reason, it was not possible to infer about the contribution of the pure “redox” mechanism in our experiments. In this sense, theoretical studies can shed a light on this matter, and interestingly, Aranifard *et al.* [50,56] have demonstrated that the “associative carboxyl pathway with redox regeneration” would present higher reaction rates and lower activation barriers than the “associative carboxyl pathway” over Pt/CeO_2 catalyst. The authors also predicted higher energy barriers for the redox regeneration pathway involving formate, in comparison to the carboxyl one, which is in line with the carboxylate path being the faster route in our findings. Even more interesting, they suggested that the “associative carboxyl pathway with redox regeneration” and the redox mechanism could take place simultaneously, however the former would have a dominant contribution. Thus, it can be suggested that in our ceria samples, besides the true “redox” mechanism, the redox regeneration could be taking place instead of the classical associative pathway, with the route involving the carboxylate as the faster path. Accordingly, Kalamaras *et al.*[49] also suggested that for Pt/CeO_2 catalyst the participation of formate would occur by the redox regeneration pathway.

Regarding the contribution of carboxylate and formate pathways, Meunier *et al.*[43] based on SSITKA studies performed on a 2 wt % Pt/CeO_2 catalyst prepared by a homogeneous precipitation of Pt(II) in urea method, reported that at 160 °C formate was practically an inactive entity, while it became a true reaction intermediate at 220 °C. The authors stated that over quite a narrow temperature range, the kinetic importance of a surface species can be dramatically different, and therefore caution is required when attempting to generalize the reaction mechanism based on data using different reaction temperatures or feed compositions, or even differently prepared and pretreated catalysts having the same nominal composition (e.g., distinct calcination and reduction conditions). Thus, formate species were reported to switch from being active intermediates at 220 °C to inactive species at 160 °C over the Pt/CeO_2 under the given reaction conditions. Kalamaras *et al*. [49] also suggested that formate species would be active intermediates on WGS reaction conducted over Pt/CeO_2 catalysts, however quantitative measurements evidenced that the route involving formate would have a minor role in the activity, which was dominated by the redox pathway. The authors also suggested that the formation of CO_2 by the redox

mechanism would be faster than the associative (formate) path and that not all adsorbed CO and formate entities would participate in the overall WGS reaction rate. Hence, the dominant reaction pathway over Pt/CeO_2 catalysts may be strongly dependent on reaction conditions, as well as the role of carboxylate and formate species on the activity. Still, the dominant route between "associative carboxyl pathway with redox regeneration" and the pure redox mechanism which would dictate the catalytic activity in our catalysts still has to be determined.

About the literature for WGS reaction over Pt/CeO_2 catalysts using ME-DRIFTS coupled with PSD methodology, it has been reported only once by Vecchietti *et al.* [159], which identified the participation of similar active intermediates, linear Pt-CO species, formates and carboxylates during reaction. Interestingly, it is the only experimental work to demonstrate the participation of carboxylates on WGS reaction by a transient DRIFTS, since such signal is commonly overlapped with formate and carbonate bands in DRIFTS spectra, and the distinction was only possible by the PSD approach. The aforementioned work was focused in evaluating the role of oxygen vacancies on the WGS reaction mechanism, by investigating two Pt catalysts supported on pure CeO_2 and gallium-doped ceria ($Ce_{80}Ga_{20}$ 9.3 % wt of Ga). The authors proposed that during ME-DRIFTS, the band associated to Ce^{3+} forbidden electronic transition ($^2F_{5/2} \rightarrow {}^2F_{7/2}$ at 2130 cm^{-1}, which is also the region of gas phase CO) did not respond to the modulation of reactants ($CO+H_2O$/He) and thus the oxygen vacancies were not participating in the WGS reaction mechanism at 250 °C. They concluded that the enhanced reducibility of the doped support was not correlated with catalytic activity, especially in the water activation step which would involve oxygen vacancies. Additionally, the authors did not describe the behavior of the distinct Pt sites over the ceria catalysts during modulation and did not take particular attention to the effect of CO coverage on Pt, since the experiment modulated $CO+H_2O$ and He gas slows. Hence, although the active intermediate species could be identified at the given reaction conditions, the aforementioned work lacks information on the role of distinct Pt sites and on the kinetics of WGS reaction. In comparison with our work, our samples did not evidence the Ce^{3+} band, which could be caused by masking such signal by the gas phase CO band, or due to a decreased reducibility of the surface ceria on the NPs over our catalysts, in comparison with theirs. However, the authors also identified the carboxylate and formate as active intermediates but both had fast responses (330 °) and they did not relate this phase delay with CO_2 formation. Since the phase angles obtained in our work were different for carboxylates and formates, this is strong evidence that the reaction pathways may be deeply dependent on the catalyst nature, since both studies involved Pt/CeO_2-based systems, and also on reaction conditions.

The fact that NP_Pt samples have similar distribution and nature of Pt sites and that HC Pt sites do not participate on the WGS reaction for **NP_Pt/SiO2** sample, whereas

they do for **NP_Pt/CeO2_5**, reinforces the argument that CO is tightly bound to these sites and remain adsorbed. However, in the latter these CO can participate on the reaction due to the interface with ceria, which enables its oxidation to CO_2 by the oxygen transfer, whether by a redox or associative (with or without redox regeneration) pathways. Thus, poisoning of HC Pt sites may be very effective on **NP_Pt/SiO2** since such oxygen transfer is not favored over silica.

Although ME-DRIFTS proved to be an interesting approach to gain insights about the routes which involve the formation of intermediates as formates and carboxylates and the role of the distinct Pt sites in the reaction, the pure redox path, which is described in literature to be the dominant one in Pt/CeO_2 samples, is not straightforwardly detected by such methodology since it does not lead to the formation of intermediates such as formates and carboxylates.

Finally, regarding the distinct activity of **iPt/CeO2_5** and **NP_Pt/CeO2_5** on WGS reaction (Figure 4.12) and remembering that both contain the same CeO_2 NPs at similar loadings but differ on Pt dispersion, ME-DRIFTS experiments can be valuable to better understand their reactivity. Figure 4.19 shows the time domain spectra at linear Pt-CO region for the final spectra under each flow ($CO+H_2O$ and He) at 250 °C for both samples.

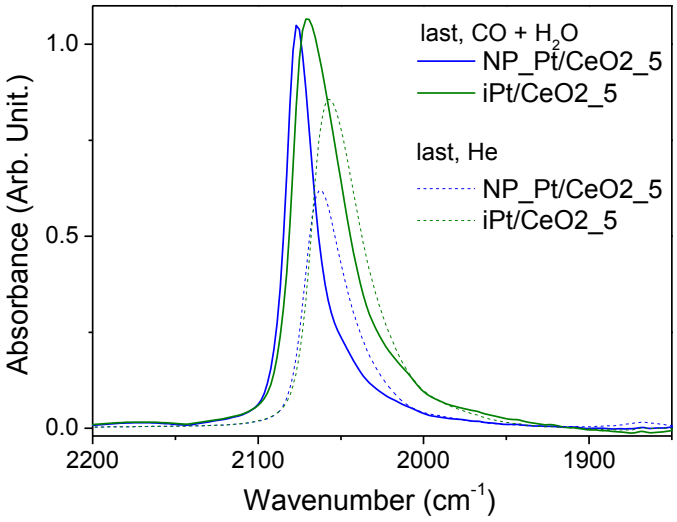

Figure 4.19: DRIFTS spectra showing the last spectra for each gas flow, illustrating the different stability of CO bound to Pt sites for **iPt/CeO2_5** and **NP_Pt/CeO2_5** at 250 °C.

Although the changes in Pt-CO region is dominated by the CO coverage differences, it is possible to observe that He desorption after $CO+H_2O$ cycle lead to more changes on Pt-CO band for **NP_Pt/CeO2_5** than for **iPt/CeO2_5**. In the latter, under $CO+H_2O$ flow the CO species are more strongly bound to Pt and do not desorb under He flow at 250 °C, leaving a broader and more intense residual band. This observation is in line

with the possibility that over **iPt/CeO2_5** some Pt sites (probably HC Pt sites) remain inactive during reaction since they are blocked by strong CO adsorption, as proposed in section 4.3.2.1. Ceria would be able to clean such sites provided the oxygen transport to CO was efficient, however if a significant blocking by carbonate species is taking place, the strongly bound CO removal as CO_2 would not be possible. Indeed, time domain spectra at LWR shown in Figure 4.20 suggests that there is an increased proportion of carbonate (1500 cm^{-1}) than formate species (1590 cm^{-1}) for **iPt/CeO2_5** sample, whereas the opposite occurs for **NP_Pt/CeO2_5**. Since carbonate is not an active intermediate, its signal does not appear in the phase domain spectra (lower right panels). The explanation for the higher amount of carbonates can only be explained by a hypothetical distinct Pt-CeO_2 interaction arising from the different formation of Pt phase on the catalysts. It appears that there might be a compromise between favoring the creation of interfacial sites and increasing the amount and stability of spectators on the catalyst surface.

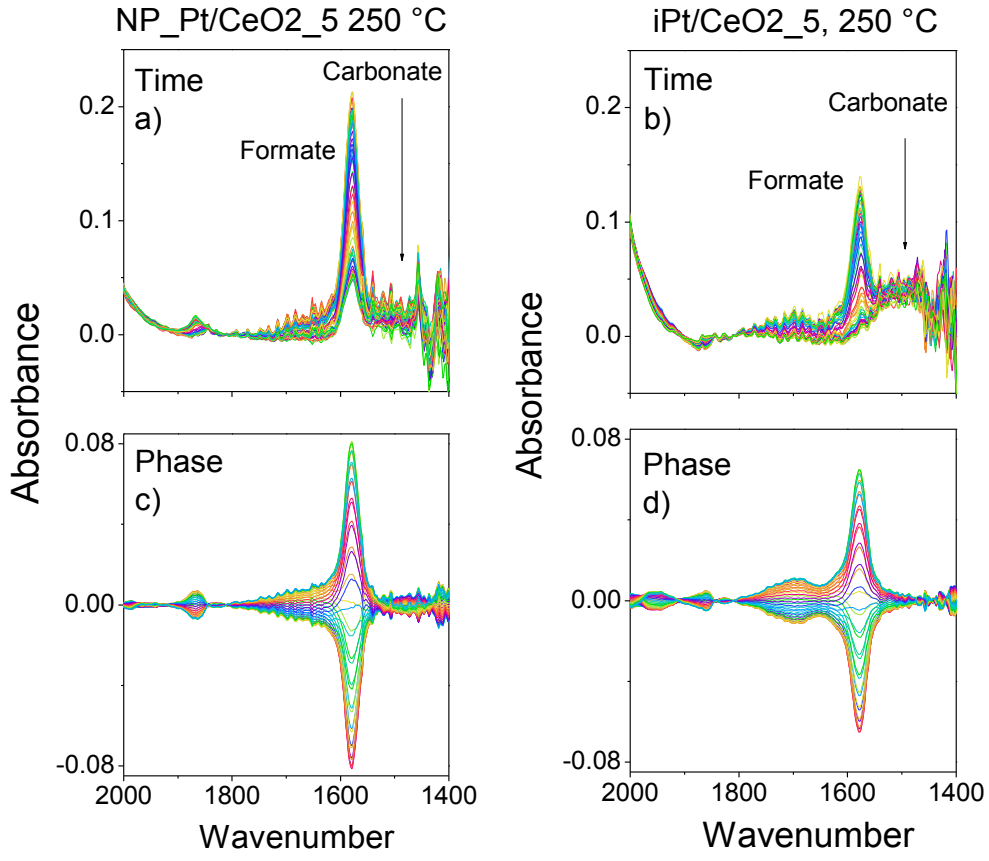

Figure 4.20: Spectra acquired during reactants modulation ($CO+H_2O$/He) cycle at 250 °C in the 2000-1400 cm^{-1} wavenumber region. a) and c) represent time and phase domain spectra, respectively, for **NP_Pt/CeO2_5** and analogously for **iPt/CeO2_5**, b) and d).

Thus, these results help to explain the trend in WGS activity observed in Figure 4.12, where **NP_Pt/CeO2_5** showed an increased CO_2 rate per Pt exposed site than

iPt/CeO2_5. It is verified that in **iPt/CeO2_5** a higher fraction of Pt sites remain bound to reaction intermediates.

4.3.2.3 WGS - MAIN CONCLUSIONS

By investigating the iPt and NP_Pt catalysts for WGS reaction, it was demonstrated that the Pt phase has a key role in the catalytic activity. More specifically, the proportion of HC, UC and WC Pt sites is determinant, since HC and UC sites were identified as the most active ones. It was also highlighted that such sites can strongly bind intermediates and decrease conversion rates and that an effective Pt-CeO_2 interface is crucial to promote the release of active sites.

Regarding the size effect of 5 and 9 nm CeO_2 NPs, no impact on catalytic activity was evidenced under the tested reaction conditions. The comparison of NP_Pt samples having different CeO_2 domains (**NP_Pt/CeO2_5** and **NP_Pt/i6CeO2**) also did not evidence a trend in catalytic activity with CeO_2 size. Both the formation of CeO_2 with controlled NPs with distinct mean size or the presence of a wide size distribution were suggested to be determinant mostly on favoring the creation of interfacial Pt-CeO_2 sites.

In situ ME-DRIFTS studies evidenced that in fact Pt/CeO_2 interfacial sites are the most active ones under WGS reaction. It was also demonstrated that over ceria samples the CO_2 formation proceeds with the participation of formate (slow pathway) and carboxylate (faster pathway), with WC Pt sites associated with the former while HC and UC sites are involved in the latter pathway. It is known that the redox pathway is also taking place, however it was not possible to follow this route.

4.3.3 GSR REACTION

Based on the WGS findings presented in the previous section, now we evaluate the impact of the Pt phase and CeO_2 size distribution in GSR reaction. Figure 4.21 shows the results for the **iPt/SiO2** and **iPt/CeO2_5** during GSR reaction. The analysis of the condensate after reaction showed no liquid byproducts were present. Concerning the gaseous products distribution exhibited in Figure 4.21a, **iPt/CeO2_5** produces significantly lower CO and higher CO_2 and H_2 fractions when compared to **iPt/SiO2** sample, corroborating the role of ceria on enhancing the WGS reaction step. The WGS activity predicted for ceria catalyst in Figure 4.10b is satisfactory achieved during GSR reactions (expected fractions of H_2 and CO of about 70% and lower than 10%, respectively), as observed in Figure 4.21a.

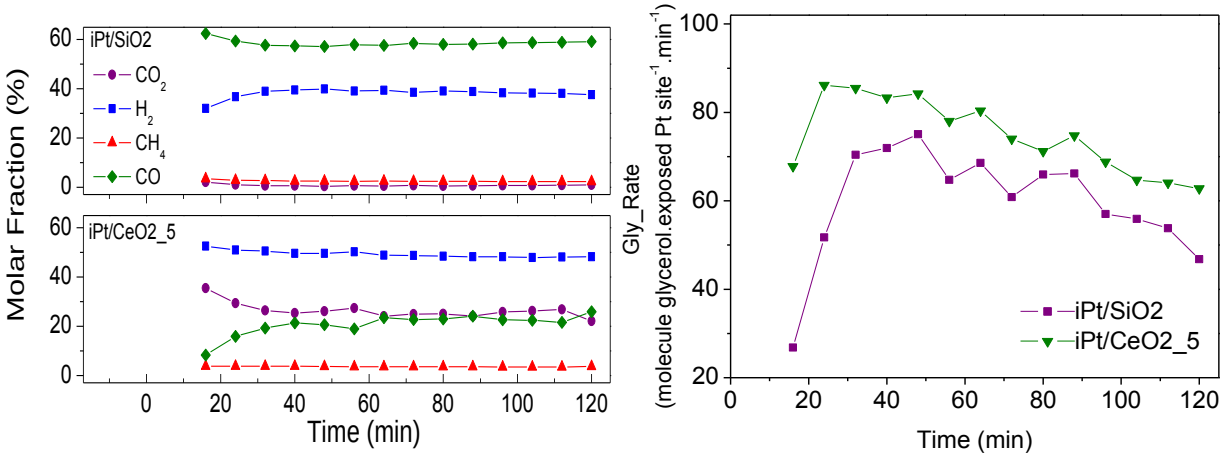

a) b)

Figure 4.21: a) Distribution of gaseous products and b) glycerol conversion rates per exposed Pt site during GSR reaction at 400 °C for **iPt/SiO2** and **iPt/CeO2_5** samples.

Figure 4.21b shows glycerol conversion rate to gas products as a function of time (calculated by (Equation 4.1 for both iPt catalysts). The **iPt/CeO2_5** catalyst presents Gly_rate_max (the maximum value of glycerol conversion rate during 2 h on stream) and Gly_rate_30 (glycerol conversion rate at 30 min of reaction, before deactivation) about 15% and 22% higher than for **iPt/SiO2**, respectively. Since the amount of Pt sites loaded for both catalytic reactions are similar and the glycerol feed is kept constant, it is possible to attribute the increased conversion of glycerol on **iPt/CeO2_5** to the presence of CeO_2. Despite the possibility of C-O bond breaking due to the presence of ceria as discussed in section 2.2.2, no liquid byproducts were detected on the liquid fraction collected after reaction for **iPt/CeO2_5**. Table 4.8 summarizes the properties of the tested samples, as well as the representative values for their performance.

Table 4.8: Catalysts properties and performance obtained for GSR reaction runs.

Sample	**Catalyst weight (g)**	**WHSV (h^{-1})[a]**	**Amount CeO_2 ($x10^{-6}$ mol)**	**Exposed Pt sites ($x10^{17}$)[b]**	**Gly_Rate (min^{-1})**	
					Max	**At 30 min**
iPt/SiO2	0.025	22.8	-	8.2	75	70
iPt/CeO2_5	0.016	35.6	10.9	8.2	86	86
NP_Pt/SiO2	0.014	40.7	-	5.8	64	21
NP_Pt/CeO2_5	0.012	47.5	7.9	5.8	92	85
NP_Pt/i6CeO2	0.013	43.8	4.6	5.8	81	72
NP_Pt/i12CeO2	0.013	43.8	6.6	5.8	92	92
NP_Pt/i20CeO2	0.013	43.8	12.1	5.8	83	78
NP_Pt/i6CeO2b	0.026	21.9	9.1	11.7	55	35

[a]: WHSV: weight hourly space velocity, calculated as the ratio between glycerol weight feed rate (0.57 $g.h^{-1}$) and the mass of catalyst.
[b]: Calculated using Pt dispersion derived from EXAFS.

Regarding the deactivation with time on stream (after the maximum rate is reached), the similar profiles for both samples indicate that some site blocking may be taking place mainly on Pt sites. Since no liquid byproducts are detected in the condensate of these two samples, the deactivation by the deposition of heavier lateral byproducts is less plausible. According to literature, as described in section 2.2.1, coke formation on Pt/SiO_2 catalysts during GSR reaction is not usual, thus the deactivation is likely due to poisoning of Pt sites by the produced CO, especially given the neutral nature of SiO_2 [6,100,101]. The high fraction of CO on **iPt/SiO2** (about 60%, Figure 4.21a) could provoke the blocking of HC and UC Pt sites. For **iPt/CeO2_5** sample, H_2 fraction is more than twice the CO fraction, but it does not rule out the possibility of CO binding strongly to Pt sites. The strong adsorption of CO on HC Pt sites at 400 °C was observed in section 4.3.1 (Figure 4.5 and Figure 4.7). Nevertheless, in the case of **iPt/CeO2_5**, such Pt poisoning may also be taking place; however, it remains slightly more active than **iPt/SiO2**, which can be related to the ability of ceria to release Pt-bound CO as CO_2. Another indicative of the blocking of active sites instead of structural modifications of active sites under reaction is that the distribution of products shown in Figure 4.21a is quite stable for both catalysts.

The highest fraction of H_2 for **iPt/CeO2_5** sample can be a result of both higher production by the decomposition reaction (Equation 1.3) and/or increased WGS rates. The latter is further illustrated by the comparison of the molar fraction of gas products (Figure 4.21a), which shows the higher proportion of H_2 and CO_2 over the ceria sample. Regarding WGS reaction step, although its participation cannot be quantitatively determined, it is clear this step was taking place solely on ceria catalyst. The absence of expressive drops in CO_2 fractions over time on stream (Figure 4.21a) suggests that WGS step is stable during GSR reaction.

Therefore, the presence of CeO_2 on **iPt/CeO2_5** catalyst for GSR reaction was beneficial, increasing the glycerol conversion rates to gas products, H_2 formation and promoting the WGS reaction step. The characterization findings in section 4.3.1 showed that these two samples have high metal dispersion and similar fraction of WC, UC and HC Pt sites, with **iPt/CeO2_5** exhibiting more oxidized Pt sites. Since the glycerol conversion rates are only slightly higher for the ceria sample, the presence of the latter do not seem to have a direct effect on glycerol decomposition, as discussed in section 2.2.2, it is mostly involved in WGS reaction step. Despite the efforts, with this two catalysts it was not possible to determine which is the main factor driving the deactivation process and catalytic activity.

To better understand the role of CeO_2 for GSR reaction and whether distinct Pt sites have an impact on the reaction, a larger set of catalyst was evaluated. Figure 4.22 shows of glycerol conversion for **iPt/SiO2** and **NP_Pt/SiO2** catalysts (mass of catalysts determined to have similar amounts of exposed Pt sites for both catalysts, ~10^{17} Pt atoms, estimated by the Pt dispersion obtained for both samples by EXAFS on Pt-L_3 edge). The significant difference in activity as a function time observed in Figure 4.22 suggests that the nature of Pt sites, probably concerning the proportion of HC, UC and WC Pt sites determines the activity. Indeed, the uneven proportion of such Pt sites could be observed in Figure 4.7, clearly showing a higher relative proportion of HC and UC Pt sites for **iPt/SiO2** when compared to **NP_Pt/SiO2**.

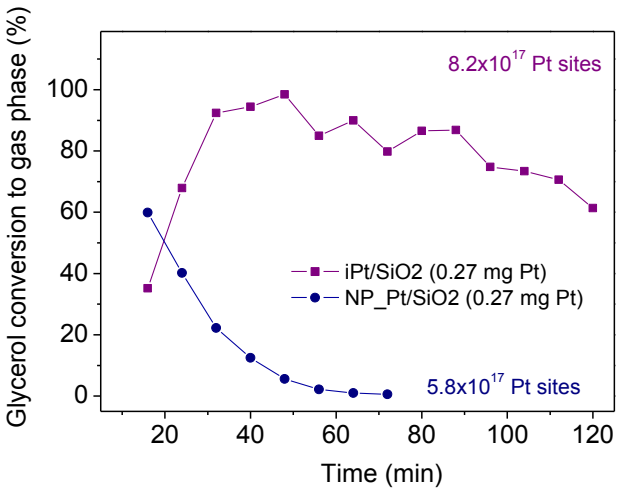

Figure 4.22: Glycerol conversion to gas products for **iPt/SiO2** and **NP_Pt/SiO2** with comparable amount of exposed Pt sites.

It was discussed in Chapter 2 that HC and UC Pt sites would be more reactive than WC ones regarding the C-C and/or C-H bond breaking, and since **iPt/SiO2** has a higher proportion of them, the conversion of glycerol would then be increased compared to **NP_Pt/SiO2**. Such low coordination Pt sites strongly attach CO, and thus would compete for glycerol and the product CO. The same is expected to occur on **NP_Pt/SiO2**, however with its lower proportion of HC and UC sites the effect of blocking some of them with CO would have a greater impact, consistent with the rapid decrease in conversion observed in Figure 4.22. Therefore, despite the diverse GSR reaction conditions on literature, our catalytic results from the samples supported on bare silica are in agreement with theoretical and experimental descriptions, in which low coordination Pt sites are deeply involved on the promotion of glycerol decomposition steps.

Figure 4.23 also exhibits the glycerol conversion to gas phase obtained for the sample **NP_Pt/i6CeO2** (using a catalyst weight to achieve comparable amounts of exposed

Pt sites as **iPt/SiO2**). Regardless the absolute values of glycerol conversion, **NP_Pt/i6CeO2** reaches the level of the **iPt/SiO2**, while remaining less active than **iPt/CeO2_5** (fixing the same number of Pt exposed sites). It is important to note that under these conditions, **NP_Pt/i6CeO2** and **iPt/CeO2_5** also possess similar amounts of CeO_2 (mol) on the catalyst beds. The beneficial effect of CeO_2 on glycerol conversion may prevail over the negative impact of the reduced proportion of the HC and UC Pt sites over **NP_Pt/i6CeO2** compared to iPt catalyst. Therefore, the low coordination Pt sites and CeO_2 were identified as determinant to favor the glycerol conversion to gas products, and the latter could also promote the WGS step during GSR reaction.

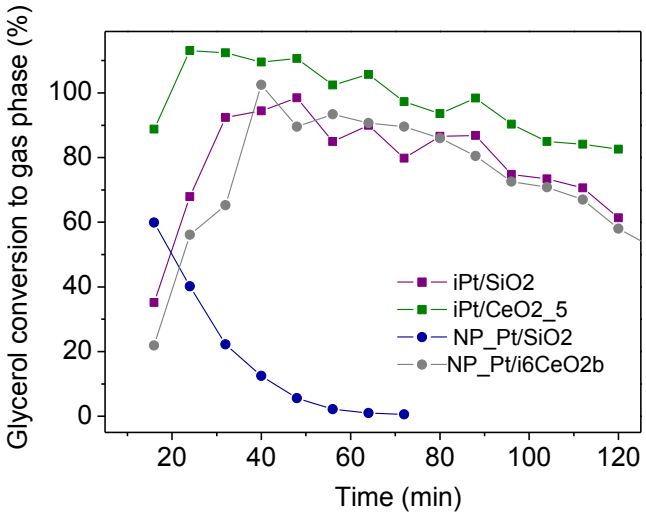

Figure 4.23: Glycerol conversion to gas products for iPt and NP_Pt catalysts with varying amount of exposed Pt sites. **NP_Pt/i6CeO2b** has a higher weight for this test (Table 4.8).

Additionally, the deactivation profile for **NP_Pt/i6CeO2** in Figure 4.23 is similar to iPt samples. Since this catalyst has a smaller fraction of HC Pt sites, a strong decrease in conversion would be expected to occur as seen for **NP_Pt/SiO2** in Figure 4.22. In this case, as CO poisoning being the most probable reason for deactivation, the higher stability shown by **NP_Pt/i6CeO2** may stem from the ability of CeO_2 to promote the CO removal as CO_2, reducing CO poisoning of low coordination Pt sites and resulting in conversion levels comparable to iPt samples. It could also reflect a change in reactivity of Pt sites due to the interface with ceria that we could not detect in the characterization step. Nevertheless, the presence of ceria in **NP_Pt/i6CeO2** seems to compensate the lower amount of HC Pt sites on the NP_Pt sample.

Having the role of Pt sites coordination already discussed, we focus now in the impact of the CeO_2 phase (particle size and dispersion) in GRS. The glycerol conversion profiles for all NP_Pt samples are presented in Figure 4.24.

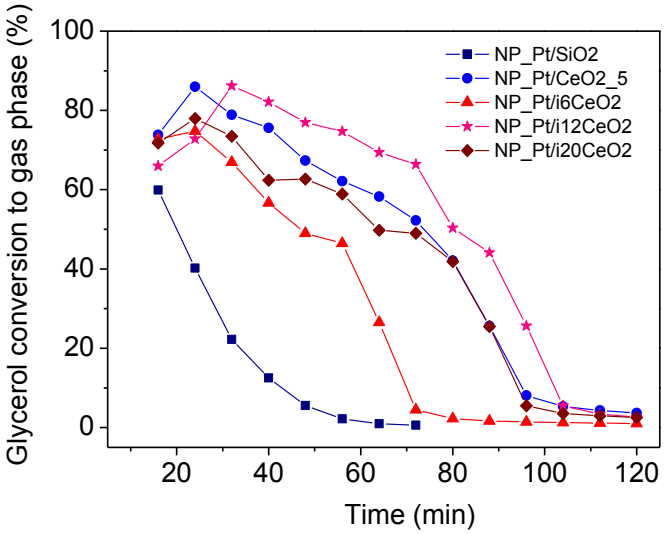

Figure 4.24: Glycerol conversion to gas phase for NP_Pt catalysts during GSR reaction.

All the samples in Figure 4.24 were tested having the same amount of exposed Pt sites and it is possible to observe a trend in glycerol conversion to gas products with CeO_2 loading among catalysts with Pt NPs. The sample with no CeO_2 has the smallest initial conversion, as well as the faster deactivation, remaining active for about 60 min on stream. With the addition of ceria, **NP_Pt/i6CeO2** (lowest CeO_2 loading), the conversion is significantly higher up to 60 min, but it fully deactivates 10 min later. As the CeO_2 loading increases, the full deactivation is delayed (occurring around 100 minutes) and the conversion levels rise, with the samples **NP_Pt/CeO2_5** and **NP_Pt/i20CeO2** exhibiting similar profiles. As shown in Table 4.9, these catalysts have 7.9 and 12.1 x 10^{-6} mol of CeO_2 respectively, and despite this small difference and the distinguished CeO_2 formation method (CeO_2 NPs or Ce^{3+} impregnation) almost no effect is noticed on conversion values. In turn, the sample **NP_Pt/i12CeO2** is slightly more active and resistant to deactivation. As observed in the characterization section (4.3.1), CeO_2 domains formed by Ce^{3+} impregnation may exhibit a broad size distribution, having smaller and larger NPs over silica surface. As discussed in section 2.2.2, it has been reported in literature that high amounts of CeO_2 and even bulk CeO_2 led to the deactivation of the catalyst due to the formation of byproducts; however, our data shows that there must be an optimal Pt:Ce ratio, within a given WHSV and glycerol concentration solution, which enables glycerol conversion for NP_Pt catalysts. It was not possible to evaluate whether liquid byproducts were present on the condensate collected during reaction for all NP_Pt samples, hence to determine if the deactivation is caused by the formation of lateral products is not possible.

It is important to add that the optimal Pt:Ce ratio (which is the best compromise between activity and deactivation) may change with reaction conditions (mass of catalyst,

temperature, glycerol concentration and feed flow). Therefore, the promoting role of CeO_2 depends strongly on the reaction conditions and catalyst nature.

To verify if the trend in activity can be related to the amount of exposed Ce atoms, the estimate for each catalyst was performed (as in section 4.3.2) and the values are shown in Table 4.9. While Figure 4.25a exhibits the glycerol conversion rates per exposed Pt site, Figure 4.25b shows the rates normalized by the exposed Ce atoms.

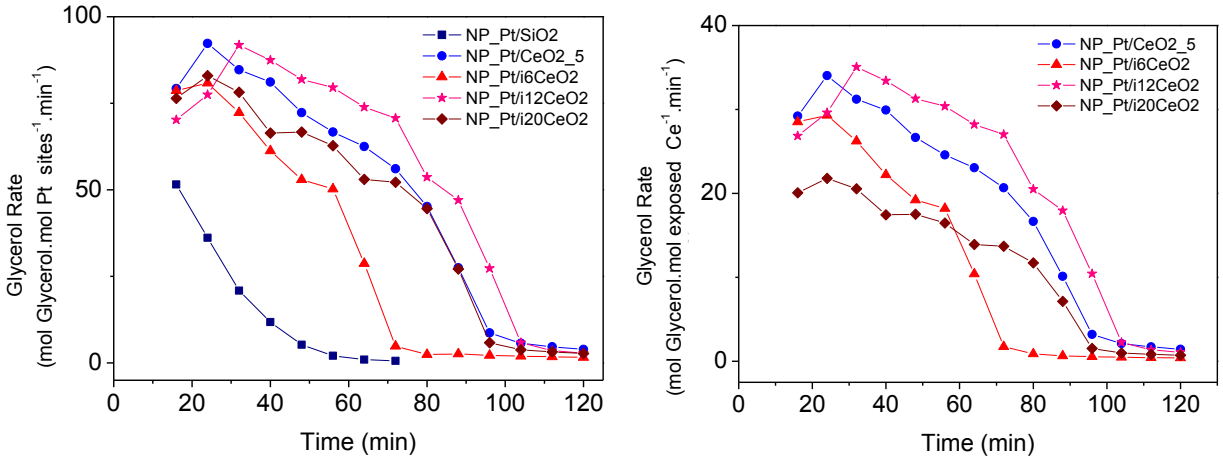

a) b)

Figure 4.25: Glycerol conversion rate for NP_Pt catalysts during GSR reaction normalized by a) exposed Pt sites and b) Ce exposed atoms.

Although the amount of exposed Ce sites are similar among **NP_Pt/CeO2_5**, **NP_Pt/i6CeO2** and **NP_Pt/i12CeO2** samples, the conversion rate normalized by Ce atoms is still higher for the ones with intermediate CeO_2 loading. It can be observed how the rate decreases for the sample with the highest amount of exposed Ce atoms. The better performance displayed by **NP_Pt/i12CeO2** may stem from the optimal Pt:Ce ratio or also from a broad size distribution of CeO_2 NPs. Regardless the amount of Ce exposed, the probability of creating interfacial Pt/CeO_2 sites for NP_Pt samples may be the factor dictating the activity.

Table 4.9: Properties of NP_Pt catalysts and their performance on GSR reaction.

Sample	**CeO_2 amount (x10^{-6} mol)**	**Number of Pt sites (x10^{17})**	**CeO_2 size domain (nm)[a]**	**Exposed Ce atoms (x10^{18})[b]**	**Max Glycerol rate by Ce (min^{-1})[c]**
NP_Pt/CeO2_5	7.9	5.8	4.9	1.6	34
NP_Pt/i6CeO2	4.6	5.8	2.8	1.6	29
NP_Pt/i12CeO2	6.6	5.8	4.2	1.5	35
NP_Pt/i20CeO2	12.1	5.8	5.3	2.2	22

[a:] CeO_2 size domain was estimated by XRD measurements using Scherrer's equation.

[b:] Estimated considering that one CeO_2 unit cell (fluorite structure, lattice parameter of 0.541 nm and volume of 0.158 nm^3) has 4 Ce atoms.

[c:] Maximum glycerol conversion rate during time on stream.

Looking in detail the distribution of products of NP_Pt catalysts with varying CeO_2 loading (Figure 4.26), up to the deactivation time (60 minutes for **NP_Pt/i6CeO2** and 100 minutes for the other CeO_2 samples) H_2 fractions are similar, indicating the role of WGS step during GSR reaction is insensitive to the CeO_2 loading.

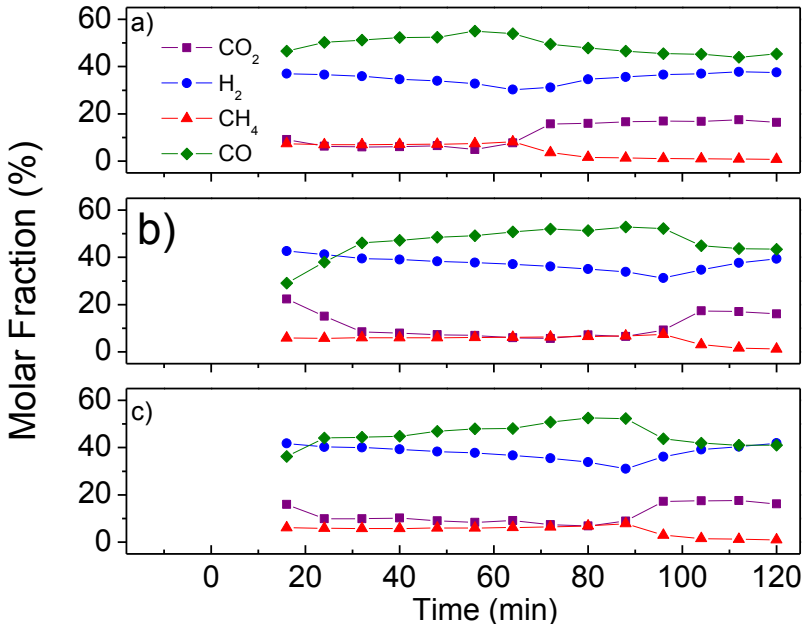

Figure 4.26: Distribution of gas products during GSR reaction for the samples with different CeO_2 loading. a) **NP_Pt/i6CeO2**, b) **NP_Pt/i12CeO2**, c) **NP_Pt/i20CeO2** catalysts.

Comparing the samples **NP_Pt/CeO2_5** and **NP_Pt/i12CeO2** in Figure 4.27, the equivalent CeO_2 loadings (12% wt) and distinct CeO_2 nature (formed by pre-formed CeO_2 NPs or by Ce^{3+} impregnation, having mean sizes of 4.2 and 4.9 nm, respectively), also resulted in comparable glycerol conversions and distribution of products. Thus, the results suggest the reaction is indifferent to the nature of CeO_2 domains within the explored conditions with the same Pt:Ce ratio.

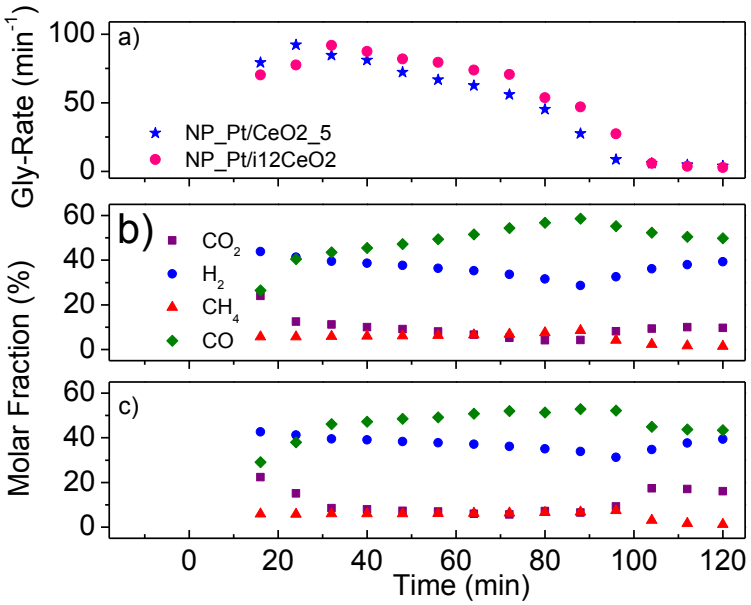

Figure 4.27: a) Glycerol conversion rates for **NP_Pt/CeO2_5** and **NP_Pt/i12CeO2**. Distribution of gaseous products during GSR reaction for b) **NP_Pt/CeO2_5** and c) **NP_Pt/i12CeO2**.

The evaluation of Pt catalysts composed of pre-synthetized Pt NPs in common for all different supports allowed the observation of the effect of CeO_2 loading, which is a compromise between the improvement in GSR and WGS reactions (even overcoming the lack of low coordination Pt sites) and the negative role of high amounts of CeO_2 (low Pt:Ce ratios) which can lead to byproducts formation.

The study of Pt catalysts for GSR reaction showed the importance of low coordination Pt atoms, possibly acting as the active sites for glycerol activation, and the promoting role of CeO_2, whether as enhancing the activation of glycerol, reducing CO poisoning and favoring WGS reaction. The presence of ceria was crucial to render **NP_Pt** catalysts active, mostly because low coordination Pt atoms are not the dominant sites. Additionally, the Pt:Ce ratio has a great impact on glycerol conversion to gas products, requiring an optimal valuet so the reaction outcome is a balance between glycerol and CO conversions and deactivation caused by formed byproducts. On the other hand, WGS reaction step occurring during GSR reaction demonstrated to be indifferent to CeO_2 loading, size and nature, showing equivalent reactivity in all evaluated conditions.

Rossetti *et al.*[24] observed that supports with many OH groups and without the predominance of Lewis acid sites (as SiO_2) showed higher amounts of coke deposited on the catalysts after GSR reaction, however the deactivation did not follow the same trend in coke deposition. The authors then proposed that the formation of coke on the support was not directly related to catalyst deactivation, as long as the exposed metallic sites (Ni) were

still active, not undergoing deactivation for some other reason. Analogously, the same could be true for the NP_Pt samples, in the case of formation of lateral products in ceria surface, it should not lead to deactivation of glycerol decomposition provided the Pt sites were still available. However, under reaction conditions the active Pt sites for glycerol decomposition seem to be blocked by CO, thus WGS step should take place to remove CO by forming CO_2, thus rendering Pt sites available again. In the case glycerol interaction over ceria caused the formation of coke or other byproducts on its surface, WGS step could not be promoted, leading to deactivation of the catalyst towards both WGS and glycerol decomposition reactions. This proposition is consistent with the case that **NP_Pt/CeO2** samples deactivate to the same extent as **NP_Pt/SiO2** (Figure 4.24**)**, which has only a small fraction of HC and UC Pt sites available and no cleaning promoted by WGS step.

The studies of both set of Pt catalysts regarding their performance for GSR reaction provided valuable insights about the thoughtful design of systems to favor higher glycerol conversion, H_2 selectivity and stability. More importantly, using diversified synthesis methods and characterizations, it was possible to distinguish key factors driving high-activity catalysts, not only the chemical composition of support, but potential active sites and their essential interaction with promoters.

4.4 GENERAL CONCLUSIONS

This chapter regarding Pt/CeO_2 and Pt/SiO_2 catalysts demonstrated the importance of several properties affecting the catalytic activity for WGS and GSR reaction. Varying the preparation of Pt catalysts evidenced the distinct reactivity of Pt sites having different atomic coordination for both explored catalytic reactions. Among WC, UC and HC Pt sites within a NP, the latter are more reactive towards glycerol decomposition; however, they are more susceptible towards poisoning for strongly binding CO. When WGS reaction is taking place, such CO poisoning is minimized at the interface with ceria through the reaction to form CO_2, and the success of this step relies on the degree of carbonate formation over ceria, which may block the interface and decrease reaction rates.

The expected promoting role of ceria in WGS reaction was evidenced and the increase in reaction rates mostly relies on the odds to create interfacial Pt/CeO_2 sites, whether by increasing CeO_2 loading or decreasing Pt and/or CeO_2 particle size. *In situ* measurements showed the exclusive participation of the interfacial Pt/CeO_2 (HC Pt) sites on the WGS reaction pathway and also pointed out that such sites are the ones related to the faster reaction pathway to produce CO_2. Additionally, it was possible to identify that the reaction mechanism occurs by the carboxylate intermediate through a faster route involving HC and UC Pt sites, while the slower path relates formate intermediates to WC Pt sites.

Concerning GSR reaction, the HC Pt sites were identified as the most active towards glycerol decomposition, which could also take place without ceria. However, the clean-up of such Pt sites is essential to assure that the catalyst remain active, thus WGS step is determinant not only to increase H_2 selectivity but also to prevent catalyst deactivation. Thus, the promoting effect of CeO_2 for GSR reaction mostly affects the release of CO from such HC Pt sites by WGS reaction. Also, the presence of ceria proved to be beneficial on C-C bond breaking and to promote increased CO_2 and H_2 fractions, however its promoting effect is limited to a strict loading range, up to that strong catalyst deactivation is observed. It is suggested that there is a compromise between enhancing WGS reaction step and favoring byproducts formation over CeO_2 that dictates the promoting ceria composition. Hence, increasing H_2 fraction on the reaction products turns out to be an intricate equation. Moreover, it was observed the strong dependence of reaction pathways and catalyst performance over different reaction conditions;

Hence, for both reactions investigated in this chapter, the importance of Pt/CeO_2 interfacial sites was highlighted, and catalyst development must take into account the optimization of their reactivity and amount.

In situ ME-DRIFTS experiments can be finely designed to probe a particular metal site and it can provide valuable information regarding reaction pathways occurring at the surface, being essential to better understand catalytic processes that will facilitate the design of more efficient systems. On the other hand, uniquely investigating true active sites is still a challenge, as well as to quantitatively determine the dominant reaction pathways taking place under a specific reaction condition.

This chapter evidenced the extreme importance of developing well-designed and size controlled catalysts to evaluate the effect of specific and isolated parameters on catalytic performance, such as distinct metal sites, metal and promoter loading, NP size. Hence, a strong effort is still needed to improve synthesis protocols in order to achieve such controlled systems. Moreover, it is relevant to stress the importance of combining the rich information provided by theoretical studies to assist in the assembly of conjectures, especially the aspects we are not able to get hold of experimentally.

Chapter 5

FINAL REMARKS AND PERSPECTIVES

The present work has demonstrated the importance of a thoughtful catalyst design to enable the independent evaluation of specific parameters that may be crucial to catalytic performance. Such investigation is essential to better understand the system behavior and thus tune catalytic properties, aiming the development of more efficient catalysts. Factors as the synthesis method (addition of Pt phase), nature of support and metal oxide promoters, size control of metal and oxide NPs and the creation of interfacial sites for bifunctional catalysts have a key role in enhancing the desired catalytic activity and H_2 selectivity and also allow a deeper comprehension of such systems. It was also demonstrated the importance of isolating overlapping parameters to evaluate the impact of one given factor (as the distinct reactivity of Pt sites and the size of CeO_2 NPs).

More specifically, the bifunctional systems explored herein were composed of Pt as the metallic phase, supported on a high surface area metal oxide (Al_2O_3 or SiO_2) and were also promoted with a reducible metal oxide (VO_x or CeO_2). The characterization of these systems provided the correlation of their catalytic activity for GSR and WGS reactions to intrinsic properties of metal, support, promoter and metal/metal oxide interface. Related to the metallic phase, it was shown that the nature and relative fraction of the exposed atoms within a nanoparticle, regarding their coordination environment and interaction with the promoter, were important factors determining the catalytic activity. Concerning the support, its nature, specifically the acid-base characteristic of the surface, also proved to be essential to favor H_2 production. In its turn, the promoter nature is also pivotal to the catalytic performance, as well as its proximity with the metallic phase, whereas factors as its size and loading are seemingly influencing on the probability of creating additional active interfacial sites. In both vanadium and ceria systems, the catalytic activity, selectivity towards H_2 and stability was utterly dependent on the increased creation of interface metal-reducible oxide interface and its efficiency in promoting the transfer of species between them. Moreover, it was evidenced that by tuning catalyst properties (as varying the loading of promoter or metallic dispersion) results in a complex interplay between increasing catalytic activity, H_2 selectivity and maintaining stability with time on stream.

Therefore, new highly active, selective and stable catalysts can be designed by effectively creating large quantities of active interfacial sites. This can be achieved through maximizing the amount of highly under-coordinated metal sites spread on the support surface, at the same time optimizing the interaction of such sites with the promoter (reducible

oxide), to facilitate the transfer of species (oxygen, hydrogen, hydroxyl groups) among them, thus avoiding the formation of strongly attached and site-blocking species.

It is also important to highlight the importance of studying model reaction as WGS and GSR, which were not conducted with realistic feed compositions (with H_2 and CO_2 presented in the industrial reformate gas or with crude glycerol from biodiesel production, respectively), but still provides rich insights that can be extrapolated to real conditions to improve catalytic performance.

Noteworthy, the *in situ* studies have proved to be an essential approach to probe structural and electronic evolution of the catalysts during reaction (by a bulk technique as XAFS), or to follow reaction intermediates and metal sites on the catalyst surface (by DRIFTS). Additionally, ME-DRIFTS experiments coupled to PSD methodology showed to be a valuable tool to distinguish active intermediates from spectators and to provide kinetic information about the simultaneous reaction pathways taking place during the catalytic reaction, as well as to demonstrate the exclusive participation of a given metal active site on the reaction. On the other hand, there is plenty of room for the development of more powerful, sensitive and surface site-specific approaches to probe true active sites and quantitatively determine the contribution of concomitant reaction pathways. This could be achieved, for example, by associating modulation-excitation methodology to several time-resolved techniques performed simultaneously under reaction conditions. Ideally it would be interesting that an element-specific spectroscopy (such as XAFS, to probe the element in the active site) would be applied with infrared spectroscopy (to probe molecular vibrations, as DRIFTS). It is also important that the techniques allow the measurements to be acquired with speeds in the same order of magnitude as the evolution of active sites and reaction intermediates, and that the data has good signal quality. If the modulation of reactants were performed using isotopes, for example, we could observe the participation of lattice oxygen during WGS reaction, thus the importance of the redox mechanism. Some techniques are already being associated for *in situ* experiments, such as XRD and XAFS, or XAFS and DRIFTS, however many results end up limited by time resolution issues or masked by the signal of non-active species or sites. Once the catalyst synthesis is advanced enough to promote the selective deposition of the element of interest, creating several single active sites over the surface, probing only these specific sites can be possible.

REFERENCES

1. Ramos, A.; Monteiro, E.; Silva, V.; Rouboa, A. Co-Gasification and Recent Developments on Waste-to-Energy Conversion: A Review. *Renew. Sustain. Energy Rev.* **2018**, *81*, 380–398.

2. Covert, T.; Greenstone, M.; Knittel, C. R. Will We Ever Stop Using Fossil Fuels? *J. Econ. Perspect.* **2016**, *30* (1), 117–138.

3. Li, H.; Riisager, A.; Saravanamurugan, S.; Pandey, A.; Sangwan, R. S.; Yang, S.; Luque, R. Carbon-Increasing Catalytic Strategies for Upgrading Biomass into Energy-Intensive Fuels and Chemicals. *ACS Catal.* **2018**, *8* (1), 148–187.

4. Laksmono, N.; Paraschiv, M.; Loubar, K.; Tazerout, M. Biodiesel Production from Biomass Gasification Tar via Thermal/catalytic Cracking. *Fuel Process. Technol.* **2013**, *106*, 776–783.

5. Dou, B.; Song, Y.; Wang, C.; Chen, H.; Xu, Y. Hydrogen Production from Catalytic Steam Reforming of Biodiesel Byproduct Glycerol: Issues and Challenges. *Renew. Sustain. Energy Rev.* **2014**, *30*, 950–960.

6. Tran, N. H.; Kannangara, G. S. K. Conversion of Glycerol to Hydrogen Rich Gas. *Chem. Soc. Rev.* **2013**, *42* (24), 9454–9479.

7. Almena, A.; Bueno, L.; Díez, M.; Martín, M. Integrated Biodiesel Facilities: Review of Glycerol-Based Production of Fuels and Chemicals. *Clean Technol. Environ. Policy* **2017**, 1–23.

8. Serrano-Ruiz, J. C.; Dumesic, J. A. Catalytic Routes for the Conversion of Biomass into Liquid Hydrocarbon Transportation Fuels. *Energy Environ. Sci.* **2011**, *4* (1), 83–99.

9. Huber, G. W.; Iborra, S.; Corma, A. Synthesis of Transportation Fuels from Biomass: Chemistry, Catalysts, and Engineering. *Chem. Rev.* **2006**, *106* (9), 4044–4098.

10. Vaidya, P. D.; Rodrigues, A. E. Glycerol Reforming for Hydrogen Production: A Review. *Chem. Eng. Technol.* **2009**, *32* (10), 1463–1469.

11. Cortright, R. D.; Davda, R. R.; Dumesic, J. A. Hydrogen from Catalytic Reforming of Biomass-Derived Hydrocarbons in Liquid Water. *Nature* **2002**, *418* (6901), 964–967.

12. Balat, M. Potential Importance of Hydrogen as a Future Solution to Environmental and Transportation Problems. *Int. J. Hydrogen Energy* **2008**, *33* (15), 4013–4029.

13. Mazloomi, K.; Gomes, C. Hydrogen as an Energy Carrier: Prospects and Challenges. *Renew. Sustain. Energy Rev.* **2012**, *16* (5), 3024–3033.

14. Holladay, J. D.; Hu, J.; King, D. L.; Wang, Y. An Overview of Hydrogen Production Technologies. *Catal. Today* **2009**, *139* (4), 244–260.

15. Li, D.; Li, X.; Gong, J. Catalytic Reforming of Oxygenates: State of the Art and Future Prospects. *Chem. Rev.* **2016**, *116* (19), 11529–11653.

16. Katryniok, B.; Paul, S.; Bellière-Baca, V.; Rey, P.; Dumeignil, F. Glycerol Dehydration to Acrolein in the Context of New Uses of Glycerol. *Green Chem.* **2010**, *12* (12), 2079.

17. Silva, J. M.; Soria, M. A.; Madeira, L. M. Challenges and Strategies for Optimization of Glycerol Steam Reforming Process. *Renew. Sustain. Energy Rev.* **2015**, *42*, 1187–1213.

18. Chheda, J. N.; Huber, G. W.; Dumesic, J. A. Liquid-Phase Catalytic Processing of Biomass-Derived Oxygenated Hydrocarbons to Fuels and Chemicals. *Angew. Chem. Int. Ed. Engl.* **2007**, *46* (38), 7164–7183.

19. Veiga, S.; Faccio, R.; Segobia, D.; Apesteguía, C.; Bussi, J. Hydrogen Production by Crude Glycerol Steam Reforming over Ni–La–Ti Mixed Oxide Catalysts. *Int. J. Hydrogen Energy* **2017**, *42* (52), 30525–30534.

20. Davidson, S. D.; Zhang, H.; Sun, J.; Wang, Y. Supported Metal Catalysts for Alcohol/sugar Alcohol Steam Reforming. *Dalton Trans.* **2014**, *43* (31), 11782–11802.

21. Douette, A. M. D.; Turn, S. Q.; Wang, W.; Keffer, V. I. Experimental Investigation of Hydrogen Production from Glycerin Reforming. *Energy & Fuels* **2007**, *21* (6), 3499–3504.

22. Montini, T.; Singh, R.; Das, P.; Lorenzut, B.; Bertero, N.; Riello, P.; Benedetti, A.; Giambastiani, G.; Bianchini, C.; Zinoviev, S.; Miertus, S.; Fornasiero, P. Renewable H_2 from Glycerol Steam Reforming: Effect of La_2O_3 and CeO_2 Addition to Pt/Al_2O_3 Catalysts. *ChemSusChem* **2010**, *3* (5), 619–628.

23. Pompeo, F.; Santori, G. F.; Nichio, N. N. Hydrogen Production by Glycerol Steam Reforming with Pt/SiO_2 and Ni/SiO_2 Catalysts. *Catal. Today* **2011**, *172* (1), 183–188.

24. Rossetti, I.; Gallo, A.; Dal Santo, V.; Bianchi, C. L.; Nichele, V.; Signoretto, M.; Finocchio, E.; Ramis, G.; Di Michele, A. Nickel Catalysts Supported Over TiO_2 , SiO_2 and ZrO_2 for the Steam Reforming of Glycerol. *ChemCatChem* **2013**, *5* (1), 294–306.

25. Iriondo, A.; Barrio, V. L.; Cambra, J. F.; Arias, P. L.; Guemez, M. B.; Sanchez-Sanchez, M. C.; Navarro, R. M.; Fierro, J. L. G. Glycerol Steam Reforming over Ni Catalysts Supported on Ceria and Ceria-Promoted Alumina. *Int. J. Hydrogen Energy* **2010**, *35* (20), 11622–11633.

26. Soares, R. R.; Simonetti, D. A.; Dumesic, J. A. Glycerol as a Source for Fuels and Chemicals by Low-Temperature Catalytic Processing. *Angew. Chem. Int. Ed. Engl.* **2006**, *45* (24), 3982–3985.

27. Zamzuri, N. H.; Mat, R.; Saidina Amin, N. A.; Talebian-Kiakalaieh, A. Hydrogen Production from Catalytic Steam Reforming of Glycerol over Various Supported Nickel Catalysts. *Int. J. Hydrogen Energy* **2017**, *42* (14), 9087–9098.

28. Kalamaras, C. M.; Dionysiou, D. D.; Efstathiou, A. M. Mechanistic Studies of the Water–Gas Shift Reaction over $Pt/Ce_XZr_{1-X}O_2$ Catalysts: The Effect of Pt Particle Size and Zr Dopant. *ACS Catal.* **2012**, *2* (12), 2729–2742.

29. Rodriguez, J. A. Gold-Based Catalysts for the Water–gas Shift Reaction: Active Sites and Reaction Mechanism. *Catal. Today* **2011**, *160* (1), 3–10.

30. Xu, W.; Si, R.; Senanayake, S. D.; Llorca, J.; Idriss, H.; Stacchiola, D.; Hanson, J. C.; Rodriguez, J. A. In Situ Studies of CeO_2-Supported Pt, Ru, and Pt–Ru Alloy Catalysts for the Water–gas Shift Reaction: Active Phases and Reaction Intermediates. *J. Catal.* **2012**, *291*, 117–126.

31. Panagiotopoulou, P.; Kondarides, D. I. Effect of the Nature of the Support on the Catalytic Performance of Noble Metal Catalysts for the Water–gas Shift Reaction. *Catal. Today* **2006**, *112* (1–4), 49–52.

32. Si, R.; Raitano, J.; Yi, N.; Zhang, L.; Chan, S.-W.; Flytzani-Stephanopoulos, M. Structure Sensitivity of the Low-Temperature Water-Gas Shift Reaction on $Cu–CeO_2$ Catalysts. *Catal. Today* **2012**, *180* (1), 68–80.

33. Gamarra, D.; Cámara, A. L.; Monte, M.; Rasmussen, S. B.; Chinchilla, L. E.; Hungría, A. B.; Munuera, G.; Gyorffy, N.; Schay, Z.; Corberán, V. C.; Conesa, J. C.; Martínez-Arias, A. Preferential Oxidation of CO in Excess H_2 over CuO/CeO_2 Catalysts: Characterization and Performance as a Function of the Exposed Face Present in the CeO_2 Support. *Appl. Catal. B Environ.* **2013**, *130–131*, 224–238.

34. Wang, X.; Rodriguez, J. A.; Hanson, J. C.; Gamarra, D.; Martínez-Arias, A.; Fernández-García, M. Ceria-Based Catalysts for the Production of H_2 Through the Water-Gas-Shift Reaction: Time-Resolved XRD and XAFS Studies. *Top. Catal.* **2008**, *49* (1–2), 81–88.

35. Shekhar, M.; Wang, J.; Lee, W.; Williams, W. D.; Kim, S. M.; Stach, E. A.; Miller, J. T.; Delgass, W. N.; Ribeiro, F. H. Size and Support Effects for the Water-Gas Shift Catalysis over Gold Nanoparticles Supported on Model Al_2O_3 and TiO_2. *J. Am. Chem. Soc.* **2012**, *134* (10), 4700–4708.

36. Vignatti, C. I.; Avila, M. S.; Apesteguía, C. R.; Garetto, T. F. Study of the Water-Gas Shift Reaction over Pt Supported on $CeO_2–ZrO_2$ Mixed Oxides. *Catal. Today* **2011**, *171* (1), 297–303.

37. Moretti, E.; Lenarda, M.; Riello, P.; Storaro, L.; Talon, A.; Frattini, R.; Reyes-Carmona, A.; Jiménez-López, A.; Rodríguez-Castellón, E. Influence of Synthesis Parameters on the Performance of $CeO_2–CuO$ and $CeO_2–ZrO_2–CuO$ Systems in the Catalytic Oxidation of CO in Excess of Hydrogen. *Appl. Catal. B Environ.* **2013**, *129*, 556–565.

38. Fonseca, J. D. S. L.; Ferreira, H. S.; Bion, N.; Pirault-Roy, L.; Rangel, M. D. C.; Duprez, D.; Epron, F. Cooperative Effect between Copper and Gold on Ceria for CO-

PROX Reaction. *Catal. Today* **2012**, *180* (1), 34–41.

39. Rodriguez, J. A.; Hanson, J. C.; Stacchiola, D.; Senanayake, S. D. In Situ/operando Studies for the Production of Hydrogen through the Water-Gas Shift on Metal Oxide Catalysts. *Phys. Chem. Chem. Phys.* **2013**, *15* (29), 12004–12025.

40. Ratnasamy, C.; Wagner, J. P. Water Gas Shift Catalysis. *Catal. Rev.* **2009**, *51* (3), 325–440.

41. Meira, D. M.; Ribeiro, R. U.; Mathon, O.; Pascarelli, S.; Bueno, J. M. C.; Zanchet, D. Complex Interplay of Structural and Surface Properties of Ceria on Platinum Supported Catalyst under Water Gas Shift Reaction. *Appl. Catal. B Environ.* **2016**, *197*, 73–85.

42. LeValley, T. L.; Richard, A. R.; Fan, M. The Progress in Water Gas Shift and Steam Reforming Hydrogen Production Technologies – A Review. *Int. J. Hydrogen Energy* **2014**, *39* (30), 16983–17000.

43. Meunier, F. C.; Goguet, A.; Hardacre, C.; Burch, R.; Thompsett, D. Quantitative DRIFTS Investigation of Possible Reaction Mechanisms for the Water-Gas Shift Reaction on High-Activity Pt- and Au-Based Catalysts. *J. Catal.* **2007**, *252* (1), 18–22.

44. Burch, R.; Goguet, A.; Meunier, F. C. A Critical Analysis of the Experimental Evidence for and against a Formate Mechanism for High Activity Water-Gas Shift Catalysts. *Appl. Catal. A Gen.* **2011**, *409–410*, 3–12.

45. Kalamaras, C. M.; Gonzalez, I. D.; Navarro, R. M.; Fierro, J. L. G.; Efstathiou, A. M. Effects of Reaction Temperature and Support Composition on the Mechanism of Water–Gas Shift Reaction over Supported-Pt Catalysts. *J. Phys. Chem. C* **2011**, *115* (23), 11595–11610.

46. Cybulskis, V. J.; Wang, J.; Pazmiño, J. H.; Ribeiro, F. H.; Delgass, W. N. Isotopic Transient Studies of Sodium Promotion of Pt/Al2O3 for the Water–gas Shift Reaction. *J. Catal.* **2016**, *339*, 163–172.

47. Phatak, A. A.; Koryabkina, N.; Rai, S.; Ratts, J. L.; Ruettinger, W.; Farrauto, R. J.; Blau, G. E.; Delgass, W. N.; Ribeiro, F. H. Kinetics of the Water-Gas Shift Reaction on Pt Catalysts Supported on Alumina and Ceria. *Catal. Today* **2007**, *123* (1–4), 224–234.

48. Petallidou, K. C.; Polychronopoulou, K.; Fierro, J. L. G.; Efstathiou, A. M. Low-Temperature Water-Gas Shift on $Pt/Ce_{0.8}La_{0.2}O_{2-\delta}$–CNT: The Effect of $Ce_{0.8}La_{0.2}O_{2-\delta}$/CNT Ratio. *Appl. Catal. A Gen.* **2015**, *504*, 585–598.

49. Kalamaras, C. M.; Americanou, S.; Efstathiou, A. M. "Redox" vs "associative Formate with –OH Group Regeneration" WGS Reaction Mechanism on Pt/CeO_2: Effect of Platinum Particle Size. *J. Catal.* **2011**, *279* (2), 287–300.

50. Aranifard, S.; Ammal, S. C.; Heyden, A. On the Importance of Metal-Oxide Interface

Sites for the Water-Gas Shift Reaction over Pt/CeO_2 Catalysts. *J. Catal.* **2014**, *309*, 314–324.

51. Ding, K.; Gulec, A.; Johnson, A. M.; Schweitzer, N. M.; Stucky, G. D.; Marks, L. D.; Stair, P. C. Identification of Active Sites in CO Oxidation and Water-Gas Shift over Supported Pt Catalysts. *Science* **2015**, *350* (6257), 189–192.

52. Guo, N.; Fingland, B. R.; Williams, W. D.; Kispersky, V. F.; Jelic, J.; Delgass, W. N.; Ribeiro, F. H.; Meyer, R. J.; Miller, J. T. Determination of CO, H_2O and H_2 Coverage by XANES and EXAFS on Pt and Au during Water Gas Shift Reaction. *Phys. Chem. Chem. Phys.* **2010**, *12* (21), 5678.

53. Grabow, L. C.; Gokhale, A. A.; Evans, S. T.; Dumesic, J. A.; Mavrikakis, M. Mechanism of the Water Gas Shift Reaction on Pt: First Principles, Experiments, and Microkinetic Modeling. *J. Phys. Chem. C* **2008**, *112* (12), 4608–4617.

54. Bruix, A.; Rodriguez, J. A; Ramírez, P. J.; Senanayake, S. D.; Evans, J.; Park, J. B.; Stacchiola, D.; Liu, P.; Hrbek, J.; Illas, F. A New Type of Strong Metal-Support Interaction and the Production of H_2 through the Transformation of Water on Pt/CeO_2(111) and Pt/$CeO_{(x)}$/TiO_2(110) Catalysts. *J. Am. Chem. Soc.* **2012**, *134* (21), 8968–8974.

55. Yang, M.; Flytzani-Stephanopoulos, M. Design of Single-Atom Metal Catalysts on Various Supports for the Low-Temperature Water-Gas Shift Reaction. *Catal. Today* **2017**, *298* (April), 216–225.

56. Aranifard, S.; Ammal, S. C.; Heyden, A. On the Importance of the Associative Carboxyl Mechanism for the Water-Gas Shift Reaction at Pt/CeO_2 Interface Sites. *J. Phys. Chem. C* **2014**, *118* (12), 6314–6323.

57. Ammal, S. C.; Heyden, A. Origin of the Unique Activity of Pt/TiO_2 Catalysts for the Water-Gas Shift Reaction. *J. Catal.* **2013**, *306*, 78–90.

58. Chen, Y.; Lin, J.; Li, L.; Qiao, B.; Liu, J.; Su, Y.; Wang, X. Identifying Size Effects of Pt as Single Atoms and Nanoparticles Supported on FeO_X for the Water-Gas Shift Reaction. *ACS Catal.* **2018**, *8* (2), 859–868.

59. Senanayake, S. D.; Rodriguez, J. A.; Stacchiola, D. Electronic Metal–Support Interactions and the Production of Hydrogen Through the Water-Gas Shift Reaction and Ethanol Steam Reforming: Fundamental Studies with Well-Defined Model Catalysts. *Top. Catal.* **2013**, *56* (15–17), 1488–1498.

60. Ahmadi, M.; Mistry, H.; Roldan Cuenya, B. Tailoring the Catalytic Properties of Metal Nanoparticles via Support Interactions. *J. Phys. Chem. Lett.* **2016**, 3519–3533.

61. Azzam, K.; Babich, I.; Seshan, K.; Lefferts, L. Bifunctional Catalysts for Single-Stage Water–gas Shift Reaction in Fuel Cell applications.Part 1. Effect of the Support on the Reaction Sequence. *J. Catal.* **2007**, *251* (1), 153–162.

62. Huang, X.; Beck, M. J. Metal-Free Low-Temperature Water-Gas Shift Catalysis over Small, Hydroxylated Ceria Nanoparticles. *ACS Catal.* **2015**, *5* (11), 6362–6369.

63. Sener, C.; Wesley, T. S.; Alba-Rubio, A. C.; Kumbhalkar, M. D.; Hakim, S. H.; Ribeiro, F. H.; Miller, J. T.; Dumesic, J. A. PtMo Bimetallic Catalysts Synthesized by Controlled Surface Reactions for Water Gas Shift. *ACS Catal.* **2016**, *6* (2), 1334–1344.

64. Roh, H.-S.; Jeong, D.-W.; Kim, K.-S.; Eum, I.-H.; Koo, K. Y.; Yoon, W. L. Single Stage Water–Gas Shift Reaction Over Supported Pt Catalysts. *Catal. Letters* **2010**, *141* (1), 95–99.

65. Azzam, K.; Babich, I.; Seshan, K.; Lefferts, L. A Bifunctional Catalyst for the Single-Stage Water–gas Shift Reaction in Fuel Cell Applications. Part 2. Roles of the Support and Promoter on Catalyst Activity and Stability. *J. Catal.* **2007**, *251* (1), 163–171.

66. Duke, A. S.; Xie, K.; Brandt, A. J.; Maddumapatabandi, T. D.; Ammal, S. C.; Heyden, A.; Monnier, J. R.; Chen, D. A. Understanding Active Sites in the Water–Gas Shift Reaction for Pt–Re Catalysts on Titania. *ACS Catal.* **2017**, *7* (4), 2597–2606.

67. Rozanska, X.; Fortrie, R.; Sauer, J. Size-Dependent Catalytic Activity of Supported Vanadium Oxide Species: Oxidative Dehydrogenation of Propane. *J. Am. Chem. Soc.* **2014**, *136* (21), 7751–7761.

68. Feng, H.; Elam, J. W.; Libera, J. A.; Pellin, M. J.; Stair, P. C. Oxidative Dehydrogenation of Cyclohexane over Alumina-Supported Vanadium Oxide Nanoliths. *J. Catal.* **2010**, *269* (2), 421–431.

69. Ndifor, E. N.; Garcia, T.; Taylor, S. H. Naphthalene Oxidation over Vanadium-Modified Pt Catalysts Supported on γ-Al_2O_3. *Catal. Letters* **2006**, *110* (1–2), 125–128.

70. García, T.; López, J. M.; López Nieto, J. M.; Sanchis, R.; Dejoz, A.; Vázquez, M. I.; Solsona, B. Insights into the Catalytic Production of Hydrogen from Propane in the Presence of Oxygen: Cooperative Presence of Vanadium and Gold Catalysts. *Fuel Process. Technol.* **2015**, *134*, 290–296.

71. Silva, A. M.; Farias, A. M. D. De; Costa, L. O. O.; Barandas, A. P. M. G.; Mattos, L. V.; Fraga, M. a.; Noronha, F. B. Partial Oxidation and Water–gas Shift Reaction in an Integrated System for Hydrogen Production from Ethanol. *Appl. Catal. A Gen.* **2008**, *334* (1–2), 179–186.

72. Vining, W. C.; Strunk, J.; Bell, A. T. Investigation of the Structure and Activity of VOx/CeO_2/SiO_2 Catalysts for Methanol Oxidation to Formaldehyde. *J. Catal.* **2011**, *281* (2), 222–230.

73. Kilos, B.; Bell, A. T.; Iglesia, E. Mechanism and Site Requirements for Ethanol Oxidation on Vanadium Oxide Domains. *J. Phys. Chem. C* **2009**, *113* (7), 2830–2836.

74. Huang, H.; Gu, Y.; Zhao, J.; Wang, X. Catalytic Combustion of Chlorobenzene over VO_x/CeO_2 Catalysts. *J. Catal.* **2015**, *326* (3), 54–68.

75. Nguyen-Thanh, D.; Duarte de Farias, A. M.; Fraga, M. A. Characterization and Activity of Vanadia-Promoted Pt/ZrO_2 Catalysts for the Water–gas Shift Reaction. *Catal. Today* **2008**, *138* (3–4), 235–238.

76. Duarte de Farias, A. M.; Bargiela, P.; Rocha, M. da G. C.; Fraga, M. A. Vanadium-Promoted Pt/CeO_2 Catalyst for Water–gas Shift Reaction. *J. Catal.* **2008**, *260* (1), 93–102.

77. Trovarelli, A. *Catalysis by Ceria and Related Materials*; Trovarelli, A., Ed.; Catalytic Science Series; Imperial College Press, 2002; Vol. 2.

78. Montini, T.; Melchionna, M.; Monai, M.; Fornasiero, P. Fundamentals and Catalytic Applications of CeO_2 -Based Materials. *Chem. Rev.* **2016**, *116* (10), 5987–6041.

79. Cargnello, M.; Doan-Nguyen, V. V. T.; Gordon, T. R.; Diaz, R. E.; Stach, E. A.; Gorte, R. J.; Fornasiero, P.; Murray, C. B. Control of Metal Nanocrystal Size Reveals Metal-Support Interface Role for Ceria Catalysts. *Science* **2013**, *341* (6147), 771–773.

80. Trovarelli, A. Catalytic Properties of Ceria and CeO_2 -Containing Materials. *Catal. Rev.* **1996**, *38* (4), 439–520.

81. Soykal, I. I.; Sohn, H.; Singh, D.; Miller, J. T.; Ozkan, U. S. Reduction Characteristics of Ceria under Ethanol Steam Reforming Conditions: Effect of the Particle Size. *ACS Catal.* **2014**, *4* (2), 585–592.

82. Buitrago, R.; Ruiz-Martínez, J.; Silvestre-Albero, J.; Sepúlveda-Escribano, A.; Rodríguez-Reinoso, F. Water Gas Shift Reaction on Carbon-Supported Pt Catalysts Promoted by CeO_2. *Catal. Today* **2012**, *180* (1), 19–24.

83. Barrio, L.; Zhou, G.; González, I. D.; Estrella, M.; Hanson, J.; Rodriguez, J. A.; Navarro, R. M.; Fierro, J. L. G. In Situ Characterization of Pt catalysts Supported on Ceria Modified TiO_2 for the WGS Reaction: Influence of Ceria Loading. *Phys. Chem. Chem. Phys.* **2012**, *14* (7), 2192–2202.

84. Wu, Z.; Li, M.; Overbury, S. H. On the Structure Dependence of CO Oxidation over CeO_2 Nanocrystals with Well-Defined Surface Planes. *J. Catal.* **2012**, *285* (1), 61–73.

85. Molinari, M.; Parker, S. Water Adsorption and Its Effect on the Stability of Low Index Stoichiometric and Reduced Surfaces of Ceria. *ACS Publ.* **2012**, No. 111.

86. van Santen, R. A.; Tranca, I.; Hensen, E. J. M. Theory of Surface Chemistry and Reactivity of Reducible Oxides. *Catal. Today* **2015**, *244*, 63–84.

87. Vayssilov, G. N.; Migani, A.; Neyman, K. Density Functional Modeling of the Interactions of Platinum Clusters with CeO_2 Nanoparticles of Different Size. *J. Phys. Chem. C* **2011**, *115* (32), 16081–16086.

88. Nagata, T.; Miyajima, K.; Hardy, R. A.; Metha, G. F.; Mafuné, F. Reactivity of Oxygen Deficient Cerium Oxide Clusters with Small Gaseous Molecules. *J. Phys. Chem. A* **2015**, *119* (22), 5545–5552.

89. Jain, R.; Poyraz, A. S.; Gamliel, D. P.; Valla, J.; Suib, S. L.; Maric, R. Comparative Study for Low Temperature Water-Gas Shift Reaction on Pt/ceria Catalysts: Role of Different Ceria Supports. *Appl. Catal. A Gen.* **2015**, *507*, 1–13.

90. Petallidou, K. C.; Boghosian, S.; Efstathiou, A. M. Low-Temperature Water–gas Shift on $Pt/Ce_{0.5}La_{0.5}O_{2-\delta}$: Effect of Support Synthesis Method. *Catal. Today* **2015**, *242*, 153–167.

91. Kale, M. J.; Christopher, P. Utilizing Quantitative in Situ FTIR Spectroscopy to Identify Well-Coordinated Pt Atoms as the Active Site for CO Oxidation on Al_2O_3-Supported Pt Catalysts. *ACS Catal.* **2016**, *6* (8), 5599–5609.

92. Lentz, C.; Jand, S. P.; Melke, J.; Roth, C.; Kaghazchi, P. DRIFTS Study of CO Adsorption on Pt Nanoparticles Supported by DFT Calculations. *J. Mol. Catal. A Chem.* **2017**, *426*, 1–9.

93. Stamatakis, M.; Chen, Y.; Vlachos, D. G. First-Principles-Based Kinetic Monte Carlo Simulation of the Structure Sensitivity of the Water–Gas Shift Reaction on Platinum Surfaces. *J. Phys. Chem. C* **2011**, *115* (50), 24750–24762.

94. Liu, X.; Ruettinger, W.; Xu, X.; Farrauto, R. Deactivation of Pt/CeO_2 Water-Gas Shift Catalysts due to Shutdown/startup Modes for Fuel Cell Applications. *Appl. Catal. B Environ.* **2005**, *56* (1–2), 69–75.

95. Shinde, V. M.; Madras, G. A Single-Stage Water-Gas Shift Reaction over Highly Active and Stable Si- and Al-Substituted Pt/CeO_2 Catalysts. *ChemCatChem* **2012**, *4* (12), 1968–1978.

96. Urakawa, A.; Bürgi, T.; Baiker, A. Sensitivity Enhancement and Dynamic Behavior Analysis by Modulation Excitation Spectroscopy: Principle and Application in Heterogeneous Catalysis. *Chem. Eng. Sci.* **2008**, *63* (20), 4902–4909.

97. Müller, P.; Hermans, I. Applications of Modulation Excitation Spectroscopy in Heterogeneous Catalysis. *Ind. Eng. Chem. Res.* **2017**, *45*, 1123-1136.

98. Aguirre, A.; Collins, S. E. Selective Detection of Reaction Intermediates Using Concentration- Modulation Excitation DRIFT Spectroscopy. *Catal. Today* **2013**, *205*, 34–40.

99. Rossi, C.; Alonso, C.; Antunes, O.; Guirardello, R.; Cardozofilho, L. Thermodynamic Analysis of Steam Reforming of Ethanol and Glycerine for Hydrogen Production. *Int. J. Hydrogen Energy* **2009**, *34* (1), 323–332.

100. Pompeo, F.; Santori, G.; Nichio, N. N. Hydrogen And/or Syngas from Steam Reforming of Glycerol. Study of Platinum Catalysts. *Int. J. Hydrogen Energy* **2010**, *35* (17), 8912–8920.

101. Sad, M. E.; Duarte, H. a.; Vignatti, C.; Padró, C. L.; Apesteguía, C. R. Steam Reforming of Glycerol: Hydrogen Production Optimization. *Int. J. Hydrogen Energy*

2015, *40* (18), 6097–6106.

102. Kim, S. M.; Woo, S. I. Sustainable Production of Syngas from Biomass-Derived Glycerol by Steam Reforming over Highly Stable Ni/SiC. *ChemSusChem* **2012**, *5* (8), 1513–1522.

103. Bobadilla, L. F.; Penkova, A.; Romero-Sarria, F.; Centeno, M. A.; Odriozola, J. A. Influence of the Acid–base Properties over $NiSn/MgO–Al_2O_3$ Catalysts in the Hydrogen Production from Glycerol Steam Reforming. *Int. J. Hydrogen Energy* **2014**, *39* (11), 5704–5712.

104. Kunkes, E. L.; Soares, R. R.; Simonetti, D. A.; Dumesic, J. a. An Integrated Catalytic Approach for the Production of Hydrogen by Glycerol Reforming Coupled with Water-Gas Shift. *Appl. Catal. B Environ.* **2009**, *90* (3–4), 693–698.

105. Wei, Z.; Karim, A. M.; Li, Y.; King, D. L.; Wang, Y. Elucidation of the Roles of Re in Steam Reforming of Glycerol over Pt–Re/C Catalysts. *J. Catal.* **2015**, *322*, 49–59.

106. Sanchez, E. A.; Comelli, R. a. Hydrogen Production by Glycerol Steam-Reforming over Nickel and Nickel-Cobalt Impregnated on Alumina. *Int. J. Hydrogen Energy* **2014**, *39* (16), 8650–8655.

107. Kim, J.; Lee, D. Glycerol Steam Reforming on Supported Ru-Based Catalysts for Hydrogen Production for Fuel Cells. *Int. J. Hydrogen Energy* **2013**, *38* (27), 11853–11862.

108. Adhikari, S.; Fernando, S.; Haryanto, A. Production of Hydrogen by Steam Reforming of Glycerin over Alumina-Supported Metal Catalysts. *Catal. Today* **2007**, *129* (3–4), 355–364.

109. Huang, X.; Dang, C.; Yu, H.; Wang, H.; Peng, F. Morphology Effect of $Ir/La_2O_2CO_3$ Nanorods with Selectively Exposed {110} Facets in Catalytic Steam Reforming of Glycerol. *ACS Catal.* **2015**, *5* (2), 1155–1163.

110. Zhang, B.; Tang, X.; Li, Y.; Xu, Y.; Shen, W. Hydrogen Production from Steam Reforming of Ethanol and Glycerol over Ceria-Supported Metal Catalysts. *Int. J. Hydrogen Energy* **2007**, *32* (13), 2367–2373.

111. Li, S.; Gong, J. Strategies for Improving the Performance and Stability of Ni-Based Catalysts for Reforming Reactions. *Chem. Soc. Rev.* **2014**, *43* (21), 7245–7256.

112. Liu, B.; Zhou, M.; Chan, M. K. Y.; Greeley, J. P. Understanding Polyol Decomposition on Bimetallic Pt-Mo Catalysts - A DFT Study of Glycerol. *ACS Catal.* **2015**, *5* (8), 4942–4950.

113. Copeland, J. R.; Santillan, I. A.; Schimming, S. M.; Ewbank, J. L.; Sievers, C. Surface Interactions of Glycerol with Acidic and Basic Metal Oxides. *J. Phys. Chem. C* **2013**, *117* (41), 21413–21425.

114. Foo, G. S.; Wei, D.; Sholl, D. S.; Sievers, C. Role of Lewis and Brønsted Acid Sites in

the Dehydration of Glycerol over Niobia. *ACS Catal.* **2014**, *4* (9), 3180–3192.

115. Cheng, C. K.; Foo, S. Y.; Adesina, A. A. Steam Reforming of Glycerol over Ni/Al_2O_3 Catalyst. *Catal. Today* **2011**, *178* (1), 25–33.

116. de Rezende, S. M.; Franchini, C. A.; Dieuzeide, M. L.; Duarte de Farias, A. M.; Amadeo, N.; Fraga, M. A. Glycerol Steam Reforming over Layered Double Hydroxide-Supported Pt Catalysts. *Chem. Eng. J.* **2015**, *272*, 108–118.

117. Ciftci, A.; Ligthart, D. a. J. M.; Hensen, E. J. M. Influence of Pt Particle Size and Re Addition by Catalytic Reduction on Aqueous Phase Reforming of Glycerol for Carbon-Supported Pt(Re) Catalysts. *Appl. Catal. B Environ.* **2015**, *174–175*, 126–135.

118. Van Santen, R. A. Complementary Structure Sensitive and Insensitive Catalytic Relationships. *Acc. Chem. Res.* **2009**, *42* (1), 57–66.

119. Buffoni, I. N.; Gatti, M. N.; Santori, G. F.; Pompeo, F.; Nichio, N. N. Hydrogen from Glycerol Steam Reforming with a Platinum Catalyst Supported on a SiO_2-C Composite. *Int. J. Hydrogen Energy* **2017**, *42* (18), 12967–12977.

120. Tereshchuk, P.; Amaral, R. C.; Seminovski, Y.; Da Silva, J. L. F. Glycerol Adsorption on a Defected Pt_6 /Pt(100) Substrate: A Density Functional Theory Investigation within the D3 van Der Waals Correction. *RSC Adv.* **2017**, *7* (28), 17122–17127.

121. Gu, X.-K.; Liu, B.; Greeley, J. First-Principles Study of Structure Sensitivity of Ethylene Glycol Conversion on Platinum. *ACS Catal.* **2015**, *5* (4), 2623–2631.

122. Mahmoodinia, M.; Trinh, T. T.; Åstrand, P.-O.; Tran, K. Geometrical Flexibility of Platinum Nanoclusters: Impacts on Catalytic Decomposition of Ethylene Glycol. *Phys. Chem. Chem. Phys.* **2017**, *19* (42), 28596–28603.

123. Liu, B.; Greeley, J. Density Functional Theory Study of Selectivity Considerations for C–C Versus C–O Bond Scission in Glycerol Decomposition on Pt(111). *Top. Catal.* **2012**, *55* (5–6), 280–289.

124. Chen, T.-L.; Mullins, D. R. Ethylene Glycol Adsorption and Reaction over CeO_X (111) Thin Films. *J. Phys. Chem. C* **2011**, *115* (28), 13725–13733.

125. El Doukkali, M.; Iriondo, A.; Arias, P. L.; Cambra, J. F.; Gandarias, I.; Barrio, V. L. Bioethanol/glycerol Mixture Steam Reforming over Pt and PtNi Supported on Lanthana or Ceria Doped Alumina Catalysts. *Int. J. Hydrogen Energy* **2012**, *37* (10), 8298–8309.

126. Ferreira, A. P.; Zanchet, D.; Rinaldi, R.; Schuchardt, U.; Damyanova, S.; Bueno, J. M. C. Effect of the CeO_2 Content on the Surface and Structural Properties of CeO_2–Al_2O_3 Mixed Oxides Prepared by Sol–gel Method. *Appl. Catal. A Gen.* **2010**, *388* (1–2), 45–56.

127. Wong, J.; Messmer, R. P.; Maylotte, D. H. K-Edge Absorption Spectra of Selected Vanadium Compounds. *Phys. Rev. B* **1984**, *30* (10), 5596–5610.

128. Ravel, B.; Newville, M. ATHENA, ARTEMIS, HEPHAESTUS: Data Analysis for X-Ray Absorption Spectroscopy Using IFEFFIT. *J. Synchrotron Radiat.* **2005**, *12* (Pt 4), 537–541.

129. Calvin, S.; Riedel, C. J.; Carpenter, E. E.; Morrison, S. A.; Stroud, R. M.; Harris, V. G. Estimating Crystallite Size in Polydispersed Samples Using EXAFS. *Phys. Scr.* **2005**, *2005* (T115), 744.

130. Wu, Z.; Stair, P. C.; Rugmini, S.; Jackson, S. D. Raman Spectroscopic Study of V/θ-Al_2O_3 Catalysts: Quantification of Surface Vanadia Species and Their Structure Reduced by Hydrogen. *J. Phys. Chem. C* **2007**, *111* (44), 16460–16469.

131. Wu, Z.; Kim, H.-S.; Stair, P. C.; Rugmini, S.; Jackson, S. D. On the Structure of Vanadium Oxide Supported on Aluminas: UV and Visible Raman Spectroscopy, UV-Visible Diffuse Reflectance Spectroscopy, and Temperature-Programmed Reduction Studies. *J. Phys. Chem. B* **2005**, *109* (7), 2793–2800.

132. Artiglia, L.; Agnoli, S.; Granozzi, G. Vanadium Oxide Nanostructures on Another Oxide: The Viewpoint from Model Catalysts Studies. *Coord. Chem. Rev.* **2015**, *301–302*, 106–122.

133. Ballarini, N.; Battisti, A.; Cavani, F.; Cericola, A.; Lucarelli, C.; Racioppi, S.; Arpentinier, P. The Oxygen-Assisted Transformation of Propane to CO_x/H_2 through Combined Oxidation and WGS Reactions Catalyzed by Vanadium Oxide-Based Catalysts. *Catal. Today* **2006**, *116* (3), 313–323.

134. Carrero, C. A.; Keturakis, C. J.; Orrego, A.; Schomäcker, R.; Wachs, I. E. Anomalous Reactivity of Supported V_2O_5 Nanoparticles for Propane Oxidative Dehydrogenation: Influence of the Vanadium Oxide Precursor. *Dalt. Trans.* **2013**, *42* (35), 12644.

135. Tanaka, T.; Yamashita, H.; Tsuchitani, R.; Funabiki, T.; Yoshida, S. X-Ray Absorption (EXAFS/XANES) Study of Supported Vanadium Oxide Catalysts. Structure of Surface Vanadium Oxide Species on Silica and γ-Alumina at a Low Level of Vanadium Loading. *J. Chem. Soc. Faraday Trans. 1 Phys. Chem. Condens. Phases* **1988**, *84* (9), 2987.

136. Ruitenbeek, M.; van Dillen, A. J.; de Groot, F.; Wachs, I.; Geus, J.; Koningsberger, D. The Structure of Vanadium Oxide Species on γ-Alumina; an in Situ X-Ray Absorption Study during Catalytic Oxidation. *Top. Catal.* **2000**, *10* (3/4), 241–254.

137. Garcia, T.; Agouram, S.; Taylor, S. H.; Morgan, D.; Dejoz, A.; Vázquez, I.; Solsona, B. Total Oxidation of Propane in Vanadia-Promoted Platinum-Alumina Catalysts: Influence of the Order of Impregnation. *Catal. Today* **2015**, *254*, 12–20.

138. Arena, F.; Frusteri, F.; Martra, G.; Coluccia, S.; Parmaliana, A. Surface Structures, Reduction Pattern and Oxygen Chemisorption of V_2O_5/SiO_2 Catalysts. *J. Chem. Soc. Faraday Trans.* **1997**, *93* (21), 3849–3854.

139. Tian, H.; Ross, E. I.; Wachs, I. E. Quantitative Determination of the Speciation of Surface Vanadium Oxides and Their Catalytic Activity. *J. Phys. Chem. B* **2006**, *110* (19), 9593–9600.

140. Martínez-Huerta, M. V.; Gao, X.; Tian, H.; Wachs, I. E.; Fierro, J. L. G.; Bañares, M. A. Oxidative Dehydrogenation of Ethane to Ethylene over Alumina-Supported Vanadium Oxide Catalysts: Relationship between Molecular Structures and Chemical Reactivity. *Catal. Today* **2006**, *118* (3–4), 279–287.

141. Ricote, S.; Jacobs, G.; Milling, M.; Ji, Y.; Patterson, P. M.; Davis, B. H. Low Temperature Water–gas Shift: Characterization and Testing of Binary Mixed Oxides of Ceria and Zirconia Promoted with Pt. *Appl. Catal. A Gen.* **2006**, *303* (1), 35–47.

142. Zheng, Y.; Zhang, L.; Wang, S.; Ding, D.; Zhang, H.; Chen, M.; Wan, H. Synergistic Effects of VO_x –Pt Probed by the Oxidation of Propane on VO_x /Pt(111). *Langmuir* **2013**, *29* (29), 9090–9097.

143. Panagiotopoulou, P.; Kondarides, D. I. A Comparative Study of the Water-Gas Shift Activity of Pt Catalysts Supported on Single (MOx) and Composite (MO_x/Al_2O_3, MO_x/TiO_2) Metal Oxide Carriers. *Catal. Today* **2007**, *127* (1–4), 319–329.

144. Wachs, I. E. Catalysis Science of Supported Vanadium Oxide Catalysts. *Dalton Trans.* **2013**, *42* (33), 11762–11769.

145. Zhou, C. H.; Zhao, H.; Tong, D. S.; Wu, L. M.; Yu, W. H. Recent Advances in Catalytic Conversion of Glycerol. *Catal. Rev.* **2013**, *55* (4), 369–453.

146. Lee, S. S.; Zhu, H.; Contreras, E. Q.; Prakash, A.; Puppala, H. L.; Colvin, V. L. High Temperature Decomposition of Cerium Precursors To Form Ceria Nanocrystal Libraries for Biological Applications. *Chem. Mater.* **2012**, *24* (3), 424–432.

147. Zhang, S.; Cargnello, M.; Cai, W.; Murray, C. B.; Graham, G. W.; Pan, X. Revealing Particle Growth Mechanisms by Combining High-Surface-Area Catalysts Made with Monodisperse Particles and Electron Microscopy Conducted at Atmospheric Pressure. *J. Catal.* **2016**, *337*, 240–247.

148. Bürgi, T.; Baiker, A. In Situ Infrared Spectroscopy of Catalytic Solid-Liquid Interfaces Using Phase-Sensitive Detection: Enantioselective Hydrogenation of a Pyrone over Pd/TiO_2. *J. Phys. Chem. B* **2002**, *106* (41), 10649–10658.

149. Zaera, F. New Advances in the Use of Infrared Absorption Spectroscopy for the Characterization of Heterogeneous Catalytic Reactions. *Chem. Soc. Rev.* **2014**, *43* (22), 7624–7663.

150. Kydd, R.; Ferri, D.; Hug, P.; Scott, J.; Teoh, W. Y.; Amal, R. Temperature-Induced Evolution of Reaction Sites and Mechanisms during Preferential Oxidation of CO. *J. Catal.* **2011**, *277* (1), 64–71.

151. George, C.; Genovese, A.; Casu, A.; Prato, M.; Povia, M.; Manna, L.; Montanari, T.

CO Oxidation on Colloidal $Au_{0.80}Pd_{0.20}$–Fe_XO_Y Dumbbell Nanocrystals. *Nano Lett.* **2013**, *13* (2), 752–757.

152. Si, R.; Flytzani-Stephanopoulos, M. Shape and Crystal-Plane Effects of Nanoscale Ceria on the Activity of Au-CeO_2 Catalysts for the Water-Gas Shift Reaction. *Angew. Chem. Int. Ed. Engl.* **2008**, *47* (15), 2884–2887.

153. Caldas, P. C. P.; Gallo, J. M. R.; Lopez-Castillo, A.; Zanchet, D.; C. Bueno, J. M. The Structure of the Cu–CuO Sites Determines the Catalytic Activity of Cu Nanoparticles. *ACS Catal.* **2017**, *7* (4), 2419–2424.

154. Raskó, J. CO-Induced Surface Structural Changes of Pt on Oxide-Supported Pt Catalysts Studied by DRIFTS. *J. Catal.* **2003**, *217* (2), 478–486.

155. Aleksandrov, H. A.; Neyman, K. M.; Hadjiivanov, K.; Vayssilov, G. N. Can the State of Platinum Species Be Unambiguously Determined by the Stretching Frequency of Adsorbed CO Probe Molecule? *Phys. Chem. Chem. Phys.* **2016**, *18*, 22108–22121.

156. Dvořák, F.; Farnesi Camellone, M.; Tovt, A.; Tran, N.; Negreiros, F. R.; Vorokhta, M.; Skála, T.; Matolínová, I.; Mysliveček, J.; Matolín, V.; Fabris, S. Creating Single-Atom Pt-Ceria Catalysts by Surface Step Decoration. *Nat. Commun.* **2016**, *7* (10801), 10801.

157. Bruix, A.; Lykhach, Y.; Matolínová, I.; Neitzel, A.; Skála, T.; Tsud, N.; Vorokhta, M.; Stetsovych, V.; Ševčíková, K.; Mysliveček, J.; et al. Maximum Noble-Metal Efficiency in Catalytic Materials: Atomically Dispersed Surface Platinum. *Angew. Chemie Int. Ed.* **2014**, *53* (39), 10525–10530.

158. Zarfl, J.; Ferri, D.; Schildhauer, T. J.; Wambach, J.; Wokaun, A. DRIFTS Study of a Commercial Ni/γ-Al_2O_3 CO Methanation Catalyst. *Appl. Catal. A Gen.* **2015**, *495*, 104–114.

159. Vecchietti, J.; Bonivardi, A.; Xu, W.; Stacchiola, D.; Delgado, J. J.; Calatayud, M.; Collins, S. E. Understanding the Role of Oxygen Vacancies in the Water Gas Shift Reaction on Ceria-Supported Platinum Catalysts. *ACS Catal.* **2014**, *4* (6), 2088–2096.

160. Bazin, P.; Saur, O.; Lavalley, J. C.; Daturi, M.; Blanchard, G. FT-IR Study of CO Adsorption on Pt/CeO_2: Characterisation and Structural Rearrangement of Small Pt Particles. *Phys. Chem. Chem. Phys.* **2005**, *7*, 187–194.

APPENDIX

ADDITIONAL WORK

5.1 The crucial role of the support in the transformations of bimetallic nanoparticles and catalytic performance

This chapter contains a brief description of the work entitled *"The crucial role of the support in the transformations of bimetallic nanoparticles and catalytic performance"*, published by Priscila Destro, Tathiana M. Kokumai, Alice Scarpellini, Lea Pasquale, Liberato Manna, Massimo Colombo, Daniela Zanchet, reprinted with permission from ACS Catalysis, Copyright 2017. The copyright clearance can be found in PUBLICATION LICENSES (pg.131).

Reference: ACS Catal. 2018, 8, 1031−1037.

My contribution to this work was mainly in the measurement, analysis and interpretation of synchrotron-based experiments, with a special focus on XAS data comprehension. I also contributed to the manuscript writing and discussion of results.

5.1.1 Abstract

The combination of two or more metals, forming alloys, core-shells or other complex hetero metallic nanostructures has substantially spanned the available options to finely tune electronic and structural properties, opening a myriad of opportunities that has yet to be fully explored in different fields. In Catalysis, the rational exploitation and design of bimetallic and trimetallic catalysts has just started. Several major aspects such as stability, phase-segregation and alloy-dealloy mechanisms have yet to be deeply understood and correlated with intrinsic factors such as nanoparticle size, composition, structure and with extrinsic factors, or external agents, such as temperature, reaction gases and support. Here, by combining model catalysts based on AuCu nanoparticles supported on silica or alumina with in situ characterization techniques under redox pretreatments and CO oxidation reaction, we demonstrate the crucial role of the support with regards to determining the stable active phase of bimetallic supported catalysts. This strategy, associated to theoretical studies, could lead to the rational design of unique active sites.

5.1.2 Graphical Abstract

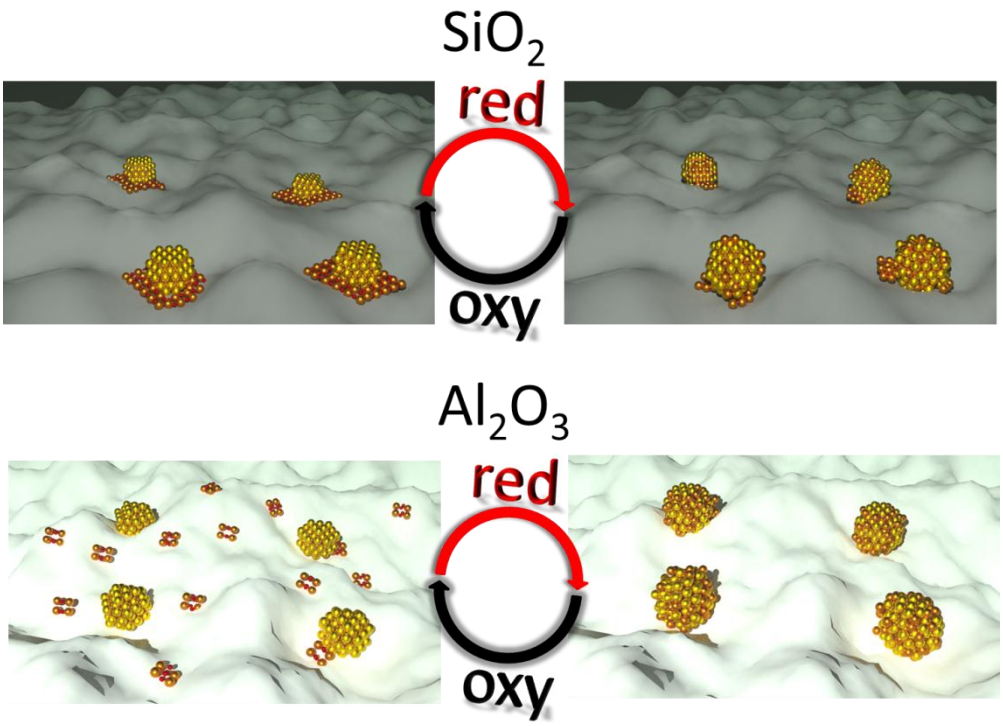

5.2 Dumbbell-like $Au_{0.5}Cu_{0.5}@Fe_3O_4$ Nanocrystals: Synthesis, Characterization, and Catalytic Activity in CO Oxidation

This chapter contains a brief description of the work entitled *"Dumbbell-like $Au_{0.5}Cu_{0.5}@Fe_3O_4$ Nanocrystals: Synthesis, Characterization, and Catalytic Activity in CO Oxidation"* published by Sharif Najafishirtari, Tathiana Midori Kokumai, Sergio Marras, Priscila Destro, Mirko Prato, Alice Scarpellini, Rosaria Brescia, Aidin Lak, Teresa Pellegrino, Daniela Zanchet, Liberato Manna and Massimo Colombo, reprinted with permission from ACS Applied Materials and Interfaces, Copyright 2016. The copyright clearance can be found in PUBLICATION LICENSES (pg. 132).

Reference: ACS Appl. Mater. Interfaces 2016, 8, 28624−28632.

My contribution to this work was in the measurement, analysis and interpretation of XAS data. I also contributed to the manuscript writing and discussion of results.

5.2.1 Abstract

We report the colloidal synthesis of dumbbell-like $Au_{0.5}Cu_{0.5}@Fe_3O_4$ nanocrystals (AuCu@FeOx NCs) and the study of their properties in the CO oxidation reaction. To this aim, the as-prepared NCs were deposited on γ-alumina and pre-treated in an oxidizing environment to remove the organic ligands. A comparison of these NCs with bulk Fe_3O_4-supported AuCu NCs showed that the nanosized support was far more effective in preventing the sintering of the metal domains, leading thus to a superior catalytic activity.

Nanosizing of the support could be thus an effective, general strategy to improve the thermal stability of metallic NCs. On the other hand, the support size did not affect the chemical transformations experienced by the AuCu NCs during the activation step. Independently from support size, we observed indeed the segregation of Cu from the alloy phase under oxidative conditions, as well as the possible incorporation of the Cu atoms into the iron oxide domain.

5.2.2 Graphical Abstract

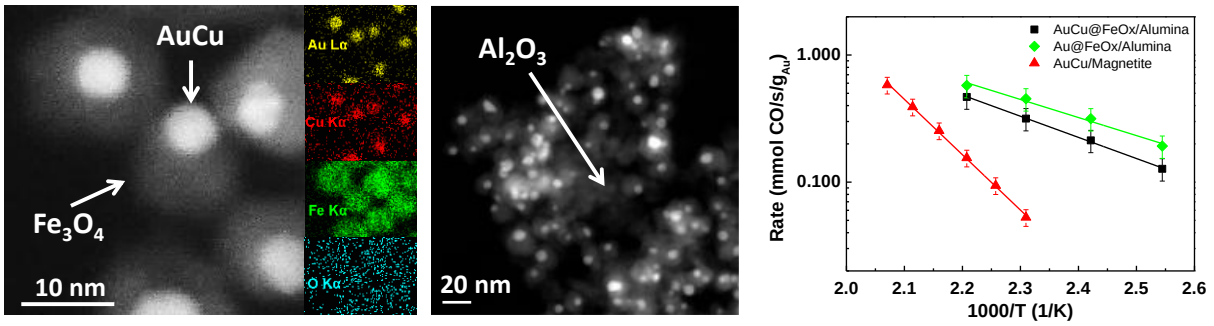

5.3 Alloying Tungsten Carbide Nanoparticles with Tantalum: Impact on Electrochemical Oxidation Resistance and Hydrogen Evolution Activity

This chapter contains a brief description of the work entitled *"Alloying Tungsten Carbide Nanoparticles with Tantalum: Impact on Electrochemical Oxidation Resistance and Hydrogen Evolution Activity"* published by Sean T. Hunt, Tathiana Midori Kokumai, Daniela Zanchet, and Yuriy Román-Leshkov, reprinted with permission from ACS Journal of Physical Chemistry C, Copyright 2015. The copyright clearance can be found in PUBLICATION LICENSES (pg. 133).

Reference: J. Phys. Chem. C 2015, 119, 13691−13699

My contribution to this work was in the measurement, analysis and interpretation of XAS data. I also contributed to the manuscript writing and discussion of results.

5.3.1 Abstract

Metal-terminated bimetallic carbide nanoparticles (NPs) of tungsten and tantalum are synthesized in a monodisperse particle size distribution of 2−3 nm. The bimetallic particles feature enhanced electrocatalytic behavior with respect to the monometallic composition. X-ray absorption near-edge structure (XANES) and extended X-ray absorption fine structure (EXAFS) measurements indicate that the $Ta_{0.3}W_{0.7}C$ NPs consist of a well-mixed random alloy featuring a compressed lattice that favorably impacts stability and catalytic activity. Electrochemical testing shows that the incorporation of 30% tantalum into the tungsten carbide lattice increases the electrochemical oxidation resistance of the NPs. The onset of surface passivation in 0.5 M H_2SO_4 shifted from +0.2 V vs RHE to +0.45 V vs RHE, and the maximum surface oxidation current shifted from +0.4 to +0.75 V vs RHE. The

activity toward hydrogen evolution (HER) of the carbon-supported $Ta_{0.3}W_{0.7}C$ NPs is preserved relative to the activity of unmodified carbon-supported WC NPs. The increase in electrochemical oxidation resistance is attributed to the presence of surface Ta moieties as determined by X-ray photoelectron spectroscopy (XPS) while the preservation of the HER activity is attributed to the observed lattice compression.

5.3.2 Graphical Abstract

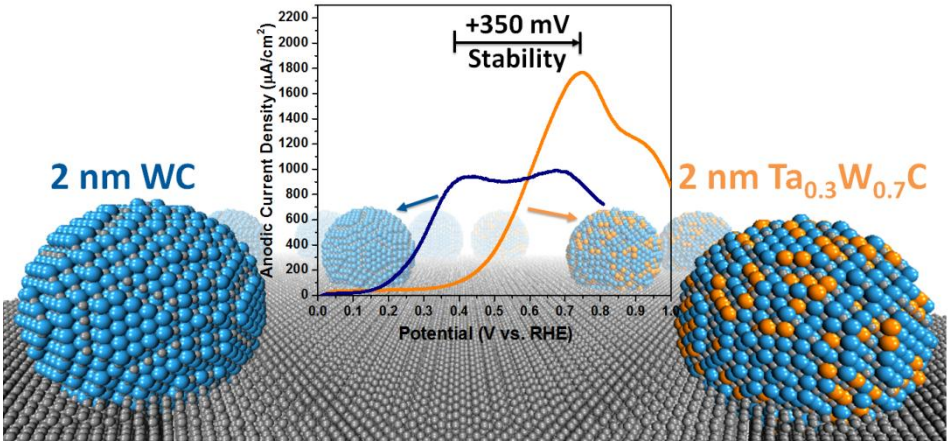

PUBLICATION LICENSES

VO_x-Pt/Al_2O_3 catalysts for hydrogen production

The crucial role of the support in the transformations of bimetallic nanoparticles and catalytic performance

Dumbbell-like $Au_{0.5}Cu_{0.5}@Fe_3O_4$ Nanocrystals: Synthesis, Characterization, and Catalytic Activity in CO Oxidation

Alloying Tungsten Carbide Nanoparticles with Tantalum: Impact on Electrochemical Oxidation Resistance and Hydrogen Evolution Activity

On the importance of metal-oxide interface sites for the water-gas shift reation over Pt/CeO_2 catalysts

ELSEVIER LICENSE
TERMS AND CONDITIONS

Mar 02, 2018

This Agreement between Institute of Chemistry -- Tathiana Kokumai ("You") and Elsevier ("Elsevier") consists of your license details and the terms and conditions provided by Elsevier and Copyright Clearance Center.

License Number	4300780527954
License date	Mar 02, 2018
Licensed Content Publisher	Elsevier
Licensed Content Publication	Journal of Catalysis
Licensed Content Title	On the importance of metal–oxide interface sites for the water–gas shift reaction over Pt/CeO2 catalysts
Licensed Content Author	Sara Aranifard,Salai Cheettu Ammal,Andreas Heyden
Licensed Content Date	Jan 1, 2014
Licensed Content Volume	309
Licensed Content Issue	n/a
Licensed Content Pages	11
Start Page	314
End Page	324
Type of Use	reuse in a thesis/dissertation
Portion	figures/tables/illustrations
Number of figures/tables/illustrations	1
Format	both print and electronic
Are you the author of this Elsevier article?	No
Will you be translating?	No
Original figure numbers	Figure 1
Title of your thesis/dissertation	PLATINUM CATALYSTS FOR HYDROGEN PRODUCTION REACTIONS
Expected completion date	Apr 2018
Estimated size (number of pages)	130
Requestor Location	Institute of Chemistry - UNICAMP Monteiro Lobato S/N Cidade Universitária Zeferino Vaz Campinas, SP 13083755 Brazil Attn: Institute of Chemistry - UNICAMP
Publisher Tax ID	GB 494 6272 12
Total	0.00 USD
Terms and Conditions	

Utilizing Quantitative in Situ FTIR Spectroscopy To Identify Well- Coordinated Pt Atoms as the Active Site for CO Oxidation on Al_2O_3-Supported Pt Catalysts

DRIFTS study of CO adsorption on Pt nanoparticles supported by DFT calculations

Order Completed

Thank you for your order.

This Agreement between Institute of Chemistry - UNICAMP -- Tathiana Kokumai ("You") and Elsevier ("Elsevier") consists of your license details and the terms and conditions provided by Elsevier and Copyright Clearance Center.

Your confirmation email will contain your order number for future reference.

printable details

License Number	4322250146751
License date	Apr 04, 2018
Licensed Content Publisher	Elsevier
Licensed Content Publication	Journal of Molecular Catalysis A: Chemical
Licensed Content Title	DRIFTS study of CO adsorption on Pt nanoparticles supported by DFT calculations
Licensed Content Author	Claudia Lentz,Sara Panahian Jand,Julia Melke,Christina Roth,Payam Kaghazchi
Licensed Content Date	Jan 1, 2017
Licensed Content Volume	426
Licensed Content Issue	n/a
Licensed Content Pages	9
Type of Use	reuse in a thesis/dissertation
Portion	figures/tables/illustrations
Number of figures/tables/illustrations	1
Format	both print and electronic
Are you the author of this Elsevier article?	No
Will you be translating?	No
Original figure numbers	Figure 4
Title of your thesis/dissertation	PLATINUM CATALYSTS FOR HYDROGEN PRODUCTION REACTIONS
Expected completion date	Apr 2018
Estimated size (number of pages)	130
Attachment	
Requestor Location	Institute of Chemistry - UNICAMP Monteiro Lobato S/N Cidade Universitária Zeferino Vaz Campinas, SP 13083755 Brazil Attn: Institute of Chemistry - UNICAMP
Publisher Tax ID	GB 494 6272 12
Total	0.00 USD

Role of Lewis and Brønsted Acid Sites in the Dehydration of Glycerol over Niobia

Steam reforming of glycerol: Hydrogen production optimization

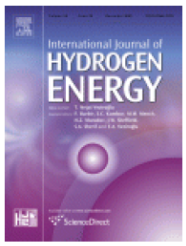

Title: Steam reforming of glycerol: Hydrogen production optimization
Author: M.E. Sad,H.A. Duarte,Ch. Vignatti,C.L. Padró,C.R. Apesteguía
Publication: International Journal of Hydrogen Energy
Publisher: Elsevier
Date: 18 May 2015

Order Completed

Thank you for your order.

This Agreement between Institute of Chemistry - UNICAMP -- Tathiana Kokumai ("You") and Elsevier ("Elsevier") consists of your license details and the terms and conditions provided by Elsevier and Copyright Clearance Center.

Your confirmation email will contain your order number for future reference.

printable details

License Number	4323231089817
License date	Apr 06, 2018
Licensed Content Publisher	Elsevier
Licensed Content Publication	International Journal of Hydrogen Energy
Licensed Content Title	Steam reforming of glycerol: Hydrogen production optimization
Licensed Content Author	M.E. Sad,H.A. Duarte,Ch. Vignatti,C.L. Padró,C.R. Apesteguía
Licensed Content Date	May 18, 2015
Licensed Content Volume	40
Licensed Content Issue	18
Licensed Content Pages	10
Type of Use	reuse in a thesis/dissertation
Portion	figures/tables/illustrations
Number of figures/tables/illustrations	1
Format	both print and electronic
Are you the author of this Elsevier article?	No
Will you be translating?	No
Original figure numbers	Figure 2
Title of your thesis/dissertation	PLATINUM CATALYSTS FOR HYDROGEN PRODUCTION REACTIONS
Expected completion date	Apr 2018
Estimated size (number of pages)	130
Attachment	
Requestor Location	Institute of Chemistry - UNICAMP Monteiro Lobato S/N Cidade Universitária Zeferino Vaz Campinas, SP 13083755 Brazil Attn: Institute of Chemistry - UNICAMP
Publisher Tax ID	GB 494 6272 12
Total	0.00 USD